

**INTEGRATED LANDSAT-ETM⁺ AND AEROMAGNETIC STUDY FOR ENHANCED
STRUCTURAL AND GEOTHERMAL INTERPRETATION: CASE STUDY OF PART
OF CALABAR FLANK, NIGERIA**

BY

CHUKWUKA, CHIDIEBERE IZUNDU (B.Sc., ESUT)

REG NO.: 20134871248

**A THESIS SUBMITTED TO THE POSTGRADUATE SCHOOL
FEDERAL UNIVERSITY OF TECHNOLOGY, OWERRI**

**IN PARTIAL FULFILMENT OF THE REQUIREMENTS FOR THE AWARD OF THE
DEGREE (MASTER OF SCIENCE), M.SC. IN GEOPHYSICS**

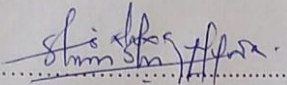
NOVEMBER, 2016



Integrated landsat-etm⁺ and aeromagnetic study for enhanced structural and geothermal interpretation: case study of part of Calabar flank, Nigeria.. By Chukwuka, C. I. is licensed under a [Creative Commons Attribution-NonCommercial-NoDerivatives 4.0 International License](https://creativecommons.org/licenses/by-nc-nd/4.0/).

CERTIFICATION

This is to certify that this work entitled "INTEGRATING LANDSAT-ETM AND HRAM DATA FOR ENHANCED STRUCTURAL AND GEOTHERMAL INTERPRETATION: CASE STUDY OF PART OF CALABAR FLANK" was carried out by "CHUKWUKA, CHIDIEBERE IZUNDU (20134871248)", in partial fulfilment for the award of the degree of M.Sc. in Geophysics in the department of Geosciences, of the Federal University of Technology, Owerri.

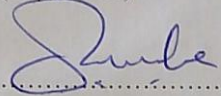


10/01/2017

Dr. Opara, Alex I.

Date

(Supervisor)

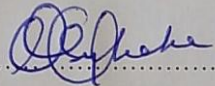


13-01-2017

Dr. Okereke, C. N.

Date

(Co-Supervisor)

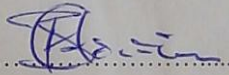


23/01/2017

Dr Okeke, O. C.

Date

(Head of Department, Geology)

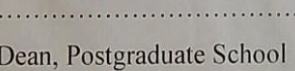


23/01/2017

Dean, School of Physical Sciences

Date

Prof. Anusonwu, B. C.

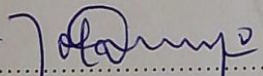


Date

Dean, Postgraduate School

Date

Prof. Oti, Nnenna N.



Date

Prof. A.S. Oniku

Date

External Examiner

DEDICATION

This work is dedicated to God Almighty, my Parents, and to all men of good will.

ACKNOWLEDGEMENTS

I acknowledge the amiable lecturers and staff of the great department of Geology, and the School of Physical Sciences (SOPS), FUTO. Special Acknowledgement goes my mentor Dr. Opara, Alex I., and to my Thesis Supervisors, in the persons of Dr. Opara, Alex I., and Dr. Okereke, C.N. I acknowledge the indelible efforts of the former HOD of Geology department, in the person of Dr. Akaolisa, C.Z., the Current HOD in the person of Dr. Okeke, O.C., and the Departmental PG Coordinator, in the person of Dr. Onyekuru, S.

My profound gratitude goes to God Almighty, whose banner over my life is love. I also cannot continue without acknowledging my Parents, Sir & Lady Chineke, A.C., my lovely Siblings, and my Uncle, Prof. Chineke Chidiezie (IMSU), all of whom God has used to beautiful my life, and for all the morals and support they have always bestowed on me. I pray God to endow you with all his blessings, and also grant that I will always reach and achieve above your expectations.

I appreciate with thanks the efforts of the amiable lecturers of Geology department, in the persons of Prof. Ibe, K.K., Dr. Akaolisa, C.Z., Dr. Okeke, O.C., Dr. Onyekuru, S.O., Dr. Opara, Alex I., Mr. Essien, A.G., Prof. Iwuagwu, C.J., Dr. Selemono, Alex, Prof. Ahirakwem, just to mention but a few.

I acknowledge also my friends and classmates, and the entire Geoscience students. I also pray God to endow everyone here with his blessings, even as you continue to do good, and obey his commands.

TABLE OF CONTENTS

TITLE PAGE	
CERTIFICATION	i
DEDICATION	ii
ACKNOWLEDGEMENT	iii
ABSTRACT	iv
TABLE OF CONTENTS	v
LIST OF TABLES	ix
LIST OF FIGURES / CHARTS	x
CHAPTER ONE: INTRODUCTION	1
1.1 Background Information	1
1.2 Statement of Problem	2
1.3 Aim and Objectives of Study	2
1.4 Justification of Study	4
1.5 Scope of Study	4
1.6 Location of Study and Geological Setting	5
1.7 Climate and Vegetation	10
1.8 Physiography and Mineralization of Study Area	11
1.9 Drainage	12
1.10 Geology of Study Area	12
1.10.1 Structural Pattern Geology	12
1.10.1 Stratigraphic Pattern Geology	16
CHAPTER TWO: LITERATURE REVIEW	18

2.1	Review of Previous Works on Aeromagnetics and Landsat-ETM studies	18
2.2	Theoretical Framework	19
2.2.1	Principles of Aeromagnetic (Airborne Magnetic) Survey	19
2.2.1.1	Geologic Applications of Aeromagnetic Data	20
2.2.1.2	Rock Magnetic Properties	21
2.2.1.3	Aeromagnetic Data Processing	24
2.2.1.4	Filtering of Aeromagnetic Map	25
2.2.1.5	Reduction to the Pole (RTP)	25
2.2.1.7	Regional- Residual Separation	26
2.2.1.8	Depth Estimation	27
2.2.1.9	Aeromagnetic Data Interpretation	28
2.2.1.9.1	Qualitative Interpretation	28
2.2.1.9.2	Quantitative Interpretation	30
2.2.2	Concept of Remote Sensing	30
2.2.3	Principles of Electromagnetic Radiation	31
2.2.4	Application of Landsat Satellite	32
2.2.5	Remote Sensing Data Analysis and Interpretation	34
2.2.5.3	Image Interpretation and Photogrammetry	34
2.2.5.4	Digital Image Preprocessing	36
2.2.5.5	Image Enhancement and Feature Extraction	36

2.2.5.6	Image Classification	37
CHAPTER THREE: METHODOLOGY		42
3.1	Research Methodology	39
3.2	Aeromagnetic Data Acquisition	41
3.3	Landsat-ETM Data Acquisition	41
3.4	Landsat-ETM Data Analysis	41
3.5	High Resolution Aeromagnetic Data Analysis	42
3.5.1	Filtering Of HRAM Map	42
3.5.2	Magnetic Depth Estimation	43
3.5.2.1	Spectral Analysis	43
3.5.2.2	3-D Euler Deconvolution	47
3.5.3	Geothermal Gradient, Curie Point Depth, and Heat Flow	51
CHAPTER FOUR: RESULTS AND DISCUSSION		53
4.1	Aeromagnetic Data: Total Magnetic Field Intensity	53
4.1.1	Total Magnetic Field Intensity	53
4.1.2	Relief of the Study Area	56
4.1.3	Upward Continuation	58
4.1.4	Applied Filters	60
4.1.4.1	Non-Linear Filter	61
4.1.4.2	B-Spline Filter and High-Pass Filter	61

4.1.5	Reduction to Pole	62
4.1.6	Horizontal Gradient Filter	64
4.1.7	Regional to Residual Anomaly Separation	65
4.1.8	Derivatives	71
4.1.8.1	Horizontal Derivatives	71
4.1.8.2	Vertical Derivatives	73
4.1.9	Depth Estimation by Spectral Analysis	75
4.1.10	Depth Estimation and Source Location by 3-D Euler Deconvolution	87
4.1.11	Curie Point Depth, Heat Flow, and Geothermal Gradient Field from Spectral Analysis.	91
4.2	Data Presentation, Results and Interpretation: Landsat-ETM Data.	95
4.2.1	Digital Elevation Model (DEM)	95
4.2.2	Lineament Density, Lineament on Drainage, and Lineament on Edge Enhanced Band5.	97
4.2.2.1	Lineament Density	97
4.2.2.2	Lineament on Drainage	98
4.2.3	Normalized Difference Vegetation Index (NDVI) Map	100
4.2.4	Color Composites	103
4.2.5	Rose Diagram	106
CHAPTER FIVE: CONCLUSION AND RECOMMENDATION		107
REFERENCES		109

LIST OF TABLES

1.1:	STRATIGRAPHIC SEQUENCE IN THE CALABAR FLANK	8
2.1:	TYPICAL MAGNETIC SUSCEPTIBILITIES OF EARTH MATERIALS.	24
3.1:	STRUCTURAL INDICES FOR SIMPLE MAGNETIC MODELS USED FOR DEPTH ESTIMATIONS BY 3D EULER DECONVOLUTION.	49
4.1:	CALCULATED DEPTH TO THE MAGNETIC SOURCE AEROMAGNETIC MAP OF IKOTEKPENE	77
4.2:	CALCULATED DEPTH TO THE MAGNETIC SOURCE AEROMAGNETIC MAP OF UWET	79
4.3:	CALCULATED DEPTH TO THE MAGNETIC SOURCE AEROMAGNETIC MAP OF UGEP	81
4.4:	CALCULATED DEPTH TO THE MAGNETIC SOURCE AEROMAGNETIC MAP OF AFIKPO	83
4.5:	BASEMENT DEPTH ESTIMATES OF THE STUDY AREA CALCULATED FROM SPECTRAL INVERSION	85
4.6:	ESTIMATED CURIE DEPTH POINT, TEMPERATURE AND HEAT FLOW	92
4.7:	CALCULATED AVERAGE CURIE POINT DEPTH (KM) AND THEIR CORRESPONDING HEAT FLOW (MWM^{-2}) FROM SPECTRAL ANALYSIS	93
4.8:	APPEARANCE OF FEATURES ON COMPOSITE IMAGES	105

LIST OF FIGURES / CHARTS

1.1:	COORDINATES OF THE STUDY DATA SHEETS	6
1.2:	GEOLOGY MAP OF STUDY AREA	6
1.3:	IDEALISED GEOLOGICAL CROSS-SECTION OF THE CALABAR FLANK SHOWING THE MAIN STRUCTURAL FEATURES AND SEQUENCES.	9
1.4:	THE MAP OF NIGER DELTA SHOWING STRUCTURAL ELEMENTS AND THE CALABAR FLANK IN RELATION TO OTHER SEDIMENTARY BASINS IN NIGERIA. (NYONG AND RAMANATHAN, 1985).	9
4.1:	TOTAL MAGNETIC FIELD INTENSITY MAP OF THE STUDY AREA	53
4.2:	3D TOTAL MAGNETIC FIELD INTENSITY MAP OF THE STUDY AREA	53
4.3:	TOTAL MAGNETIC FIELD INTENSITY MAP OF THE STUDY AREA	54
4.4:	COLOUR SHADED PIXEL MAP OF THE TOTAL MAGNETIC FIELD INTENSITY OF THE STUDY AREA CONTOURED IN GAMMAS.	55
4.5:	TOTAL MAGNETIC FIELD INTENSITY OF THE STUDY AREA CONTOURED IN GAMMAS.	55
4.6:	SHADED RELIEF MAP OF THE TOTAL MAGNETIC FIELD INTENSITY OF THE STUDY AREA CONTOURED IN GAMMAS	57
4.7:	3-D SURFACE MAP OF THE STUDY AREA	57
4.8:	UPWARD CONTINUATION MAP OF THE STUDY AREA.	59
4.9:	NON-LINEAR FILTER MAP OF THE STUDY AREA.	60
4.10:	B-SPLINE FILTER MAP OF THE STUDY AREA	60
4.11:	HIGH PASS FILTER MAP OF THE STUDY AREA	60
4.12:	REDUCTION TO POLE FILTER MAP OF THE STUDY AREA.	63

4.13:	HORIZONTAL GRADIENT FIELD MAP OF THE STUDY AREA.	64
4.14:	FIRST DEGREE REGIONAL FIELD	67
4.15:	SECOND DEGREE REGIONAL FIELD	67
4.16:	THIRD DEGREE REGIONAL FIELD	67
4.17:	FOURTH DEGREE REGIONAL FIELD	67
4.18:	FIRST DEGREE RESIDUAL FIELD	68
4.19:	SECOND DEGREE RESIDUAL FIELD	68
4.20:	THIRD DEGREE RESIDUAL FIELD	68
4.21:	FOURTH DEGREE RESIDUAL FIELD	68
4.22:	FIRST DEGREE RESIDUAL FILTER MAP OF THE STUDY AREA	69
4.23:	SECOND DEGREE RESIDUAL FILTER MAP OF THE STUDY AREA	69
4.24:	THIRD DEGREE RESIDUAL FILTER MAP OF THE STUDY AREA	69
4.25:	FOURTH DEGREE RESIDUAL FILTER MAP OF THE STUDY AREA	69
4.26:	FIRST HORIZONTAL DERIVATIVE MAP OF THE STUDY AREA.	72
4.27:	SECOND HORIZONTAL DERIVATIVE MAP OF THE STUDY AREA.	72
4.28:	FIRST VERTICAL DERIVATIVE MAP OF THE STUDY AREA.	74
4.29:	SECOND VERTICAL DERIVATIVE MAP OF THE STUDY AREA.	74
4.30:	PLOT OF LOG POWER AGAINST FREQUENCY (IKOT-EKPENE)	
4.31:	TOTAL MAGNETIC INTENSITY FIELD MAP OF THE AEROMAGNETIC DATA OF THE IKOT-EKPENE	75
4.32:	INTERPRETATION OF SOME LINEAR MAGNETIC ANOMALIES FROM IKOT-EKPENE	76
4.33:	PLOT OF LOG POWER AGAINST FREQUENCY (UWET)	77

4.34:	TOTAL MAGNETIC INTENSITY FIELD MAP OF THE AEROMAGNETIC DATA OF THE UWET	78
4.35:	INTERPRETATION OF SOME LINEAR MAGNETIC ANOMALIES FROM UWET	79
4.36:	PLOT OF LOG POWER AGAINST FREQUENCY (UGEP)	80
4.37:	TOTAL MAGNETIC INTENSITY FIELD MAP OF THE AEROMAGNETIC DATA OF THE UGEP	80
4.38:	INTERPRETATION OF SOME LINEAR MAGNETIC ANOMALIES FROM UGEP	81
4.39:	PLOT OF LOG POWER AGAINST FREQUENCY (AFIKPO)	82
4.40:	TOTAL MAGNETIC INTENSITY FIELD MAP OF THE AEROMAGNETIC DATA OF THE AFIKPO	82
4.41:	INTERPRETATION OF SOME LINEAR MAGNETIC ANOMALIES FROM AFIKPO SHEET	83
4.42:	DEPTH MAP, D1	86
4.43:	3D WIREFRAME DEPTH MAP, D1	86
4.44:	DEPTH MAP, D2	86
4.45:	3D WIREFRAME DEPTH MAP, D2	86
4.46:	STANDARD EULER MAP (SI=0)	88
4.47:	STANDARD EULER MAP (SI=1)	88
4.48:	STANDARD EULER MAP (SI=2)	88
4.49:	STANDARD EULER MAP (SI=3)	88

4.50:	STANDARD EULER MAP (SI=0)	89
4.51:	STANDARD EULER MAP (SI=1)	89
4.52:	TANDARD EULER MAP (SI=2)	89
4.53:	STANDARD EULER MAP (SI=3)	89
4.54:	PLOT OF CURIE POINT DEPTH VERSUS HEAT FLOW	93
4.55:	PLOT OF CURIE POINT DEPTH VERSUS GEOTHERMAL GRADIENT	93
4.56:	DIGITAL ELEVATION MODEL OF THE STUDY AREA	95
4.57:	LINEAMENT DENSITY MAP OF THE STUDY AREA	97
4.58:	LINEAMENT ON DRAINAGE MAP OF THE STUDY AREA	99
4.59:	NDVI MAP OF THE STUDY AREA	101
4.60:	RGB 432 COLOR COMPOSITE MAP	104
4.61:	RGB 517 COLOR COMPOSITE MAP	104
4.62:	RGB 721 COLOR COMPOSITE MAP	104
4.63:	ROSE DIAGRAM	106

ABSTRACT

An integrated structural interpretation of part of the Calabar Flank and environs was carried out using high resolution aeromagnetic (HRAM) and Landsat-ETM⁺ data to study magnetic basement depth, structure and tectonics of the study area. It is believed that result of this study will help in making far reaching inferences of the hydrocarbon and geothermal potentials of the study area. Several image processing and analytical techniques were applied to both the aeromagnetic and Landsat-ETM⁺ data to improve the data quality and resolution. Regional – residual separation was carried out on the aeromagnetic data using polynomial regression analysis. The acquired residual data were then used for more detailed interpretation of the HRAM data. The study revealed several linear features with structural trends in the NE-SW, ENE-WSW and N-S directions, with the NE-SW been dominant. These paleo-structures are believed to have played essential roles in the geodynamic and tectonic evolution of the study area. Similarly, several circular clusters of magnetic anomaly closures observed in the NE-SW section of the study area were interpreted as lithological variations of mafic-ultramafic inclusions. The positive and negative second derivative anomalies correlated with the presence and distribution of mafic and felsic rock forming minerals within the study area. Spectral inversion was carried out using the residual data to estimate the Curie point depth, heat flow and geothermal gradient in the study area. Results of the 2-D spectral analysis revealed a two layer depth model with the depth to shallower magnetic source bodies (d_1) varying from 0.0345 km to 2.7798 km, with an average depth of 1.365425 km, while the depth to the deeper magnetic source bodies (d_2), varies from 0.7012 km – 6.7893 km, with an average depth of 3.403056 km. Structural analysis of these shallow anomalies using 3-D Euler deconvolution with structural index values ranging from 0-3, revealed three main structural models which include spheres, pipes/cylinders, and sills/dikes. These shallower sources are probably due to intra-basement features within the basement and magnetized bodies which intruded into the sedimentary cover. Heat flow estimated from spectral inversion revealed three main geo-thermally active areas which include Afikpo, Ugep and Uwet, with heat flow values of 64.71 mW/m², 66.23 mW/m² and 64.87 mW/m² respectively. These areas are therefore recommended for further geothermal exploration. Finally, the average

sedimentary thickness of 2.660 km derived from this study is interpreted as unfavorable for hydrocarbon generation, as it suggests possible over cooking kerogen in the study area.

Keywords: Magnetic anomaly, Curie point, Thermal gradient, Heat flow, Lineament, Calabar Flank.

CHAPTER ONE

INTRODUCTION

1.1 Background Information

The Calabar Flank, southeastern Nigeria, holds a Cretaceous-Tertiary succession and this represents a post rift basin fill containing about 4 km of fluvial-continental, marine and paralic sediments (Odumudu, 2012). The presence of associations of shales, sandstones and limestones in the area suggests possible source rocks, reservoir rocks, traps and seals which present a potential for hydrocarbon accumulation in the area. This has generated interest in the study of the regional petroleum potential of the area. The area is also characterized by the existence of minerals. These minerals and hydrocarbons are associated with inherent magnetic intensity.

The interpretation of structures existing in the Calabar Flank using a combination of Aeromagnetic (geophysical) and Landsat ETM (remote sensing) data and examining the temperature and geothermal gradient field of the area is the chosen approach to this work.

This use of aeromagnetic and Landsat data imagery have therefore found much significance in the study of geological structures. Thus the past few decades have therefore seen a revolution in the integration of aeromagnetic and Landsat images for interpretation of structure and lithologic variations in the sedimentary section. Several studies carried out worldwide (Opara, 2012; Al-Moush et al., 2013; Kowalik and Glenn., 1987; Rangani and Ebinger., 2008; Ramasamy, 2010, among others) revealed that the combined interpretation of aeromagnetic and landsat data added significant structural elements that were previously unrecognized from the separate interpretation of the respective datasets.

The study area lies between latitudes $5^{\circ}00''$ N – $6^{\circ}00''$ N and longitudes $7^{\circ}30''$ E – $8^{\circ}30''$ E. The NW-SE aligned Calabar Flank forms the boundary between the Oban Massif to the north and the eastern part of the Cenozoic – Recent Niger Delta complex to the south. To the southeast, the Calabar Flank is contiguous with the Doula Basin in Cameroun (Reyment, 1965). The Calabar Flank is a sedimentary basin extending from the southern margins of the igneous Oban Massif to the hinge line of the Niger Delta (Reijers and Petters, 1987). The Flank extends to the Cameroun

volcanic ridge in the east. Northwest–southeast trending basement structures underlie the Flank and define the Ituk high and the Ikang trough; thus relating the Calabar Flank to the south Atlantic Cretaceous marginal basins with similar horst and graben structures.

This study therefore seeks to use aeromagnetic and Landsat imageries in interpreting both geologic and structural features within the study area.

“Geothermal gradient in the area range between 30°C/km and 45°C/km, with a corrected average of 38.8°C/km. The adjoining parts of the Niger Delta have values that are lower than 30°C/km. In the Calabar Flank, elevated temperatures were observed at depths of 1000 m, 2000 m, and 3000 m. This contrasts with the adjoining parts of the Niger Delta having lower temperatures characteristic of a more normal thermal regime. The elevated temperatures in the Calabar Flank are attributable to such factors as volcanic intrusion into the sediments, the shallow depth to basement, increase in Shaliness (reduction in Sand percentage), upward transmission of hotter fluids through the faults, and closeness to the Cameroun volcanic line. The elevated temperatures suggest possible thermal cracking of generated hydrocarbons to gas” (Odumodu, 2012).

Basically, aeromagnetic maps display variations in the magnetic field of crustal rocks and are usually expressed in gammas. This data can be used to delineate structural trends by following lineaments in magnetic contours (Okereke and Ananaba, 2006). Moreover, they can be used successfully in mapping new structures and extending known areas. The anomalies in the magnetic field of the earth may be considered as arising from two principal causes – lateral changes in the magnetic polarization of the basement rocks and the structure of the basement surface.

1.2 Statement of Problem

Previous studies on the Cretaceous sedimentary rocks that outcrops in the Calabar Flank are mostly limited to geological descriptions (Adeleye and Fayose, 1978; Petters, 1982; Reyment, 1965; Peters et al., 1995).

This Calabar flank from literature holds Cretaceous to Tertiary sediments and shares in the geological and structural evolution of the Benue trough, and extends from the southern margins of the Igneous Oban Massif to the hinge line of the Niger Delta (Reijers and Petters, 1987). This connection and more lead to studies on the hydrocarbon generation potential of the Calabar Flank, and the recent discovery of oil seeps in the Calabar Flank generated renewed interest in appraising the petroleum potential of the area. But for a better understanding of the hydrocarbon generation potential of the Flank, a previous study conducted (Odumodu, 2012), detailed geochemical and organic petrographic studies with the aim of reconstructing paleo-environmental control on the deposition of organic-rich shales in the Calabar Flank. The area also has abundance of certain minerals of economic viability. But the Geophysical methods used in prospecting for these minerals and hydrocarbon are not totally putting all the square pegs in square holes.

There's also the glaring fact of lacking crustal temperature information within the study area, and the importance of geothermal investigation cannot be over emphasized, as temperatures inside the earth directly controls most of the geodynamic processes that are visible on the surface (Nwankwo, et al 2011). Also the assessment of variations of the Curie isotherm of an area can provide valuable information about the regional temperature distribution at depth and the concentration of subsurface geothermal energy. But these information and clear/conclusive findings are in short fall within the Calabar Flank.

1.3 Aim and Objectives of Study

The chosen approach to this work is to carry out an enhanced interpretation of parts of the Calabar Flank, by using an integrated Landsat-ETM and High Resolution Aeromagnetic Data, to provide geological results, and determine the temperature and geothermal gradient field of the area.

The objectives are;

- To identify and determine varieties of geologic structures, stratigraphic units, and mineralization precursors.

- To determine the subsurface temperature (Curie point depth/temperature), and geothermal gradient field of the area
- To employ spectral analysis and 3D Euler Deconvolution for depth-to-magnetic sources determination and structural interpretation.
- To determine the regional petroleum potential of the area.

1.4 Justification of Study

The study, is to compliment the geophysical information on the study area in a better way, by integrating Landsat-ETM and High Resolution Aeromagnetic Survey data.

To bridge the gap of lacking crustal temperature information within the study area, the option of geothermal investigation has also been chosen for the study since temperature inside the earth directly controls most of the geodynamic processes that are visible on the surface (Nwankwo, et al 2011). In this regard, Heat flow measurements in several parts of African continent have revealed that the mechanical structure of the African lithosphere is variable (Nur, et al 1999).

Therefore, regional temperature distribution at depth in the area, and the concentration of subsurface geothermal energy were obtained from this study. Geothermally active areas were observed as having shallow Curie point depth and high heat flow values (Nur, et al 2005). This assessment of variations of the Curie isotherm of the area of study provided valuable information about the regional temperature distribution at depth and the concentration of subsurface geothermal energy.

1.5 Scope of Study

For this study, four (4) High Resolution Digital Aeromagnetic data were used. It is high resolution because, it provides more detailed information on the area and more flexibility in analysis of the data. They were then integrated with Landsat Enhanced-Thematic-Mapper-Data.

The study was limited to achieving the prelisted objectives, between latitudes 5°00'N and 6°00'N and longitudes 7°30'E and 8°30'E.

The areas within the coordinates of the study area are Afikpo, Ugep, Ikot-Ekene and Uwet. Ground truthing was not undertaken.

1.6 Location of Study and Geological Setting

The study area (Fig. 1.1 and 1.2) lies between latitudes 5°00'N and 6°00'N and longitudes 7°30'E and 8°30'E. It covers four localities, namely Afikpo, Ugep, Ikot Ekpenne and Uwet, all lying within the Calabar Flank.

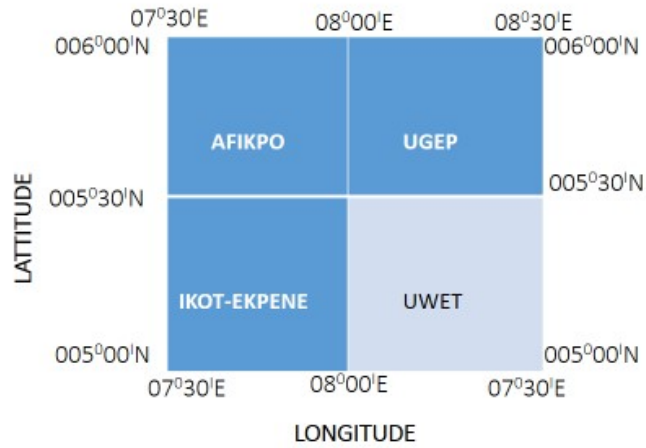


FIG 1.1: COORDINATES OF THE STUDY DATA SHEETS

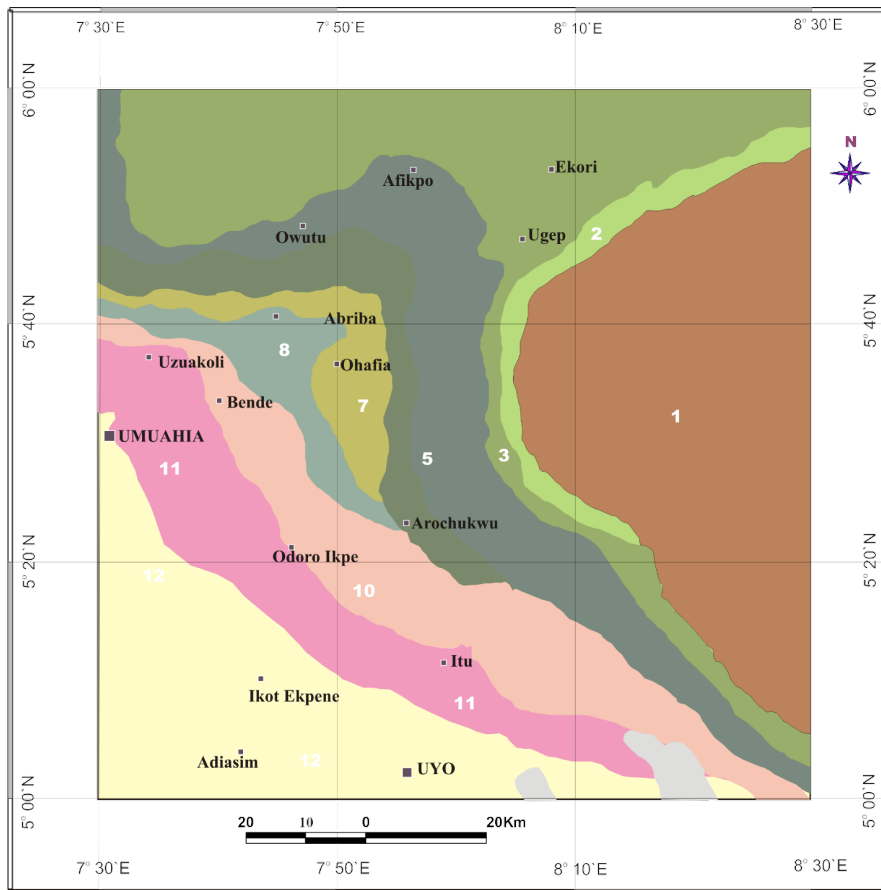


FIG 1.2: GEOLOGY MAP OF STUDY AREA

The term Calabar Flank was first proposed by Murat (1972) for that part of the southern sedimentary basin in the Niger Delta of Nigeria characterized by crustal block faulting. It was formed by incipient rifting during the breakaway of South America from Africa and the opening of the South Atlantic in Albian times (Whiteman, 1982) with the basement structures that align parallel to those underlying the coastal basins of Gabon, Congo and Angola.

The structures in these basins formed during the opening of the South Atlantic Ocean are similar, except for the absence of evaporates in the Calabar Flank which were prevented from deposition by the Guinea Ridge. There is considerable lithologic similarity including carbonate development between the West African South Atlantic Coastal basins and the Calabar Flank. They are therefore classified as components of a typical divergent, rafted continental margin, and in general can be linked to a single evolutionary geologic history. The Cretaceous sedimentary rocks of the Calabar Flank are unique in that the whole Upper Cretaceous sequence is exposed in outcrops within a narrow strip of about 8 km. The Calabar flank is a sedimentary basin that borders southeastern Nigeria's continental margin. According to Reijers and Petters, 1987, the Calabar Flank is at right angles to the major rift faults of the Benue Trough and structurally consists of NW-SE trending basement horsts (the Oban massif and the Ituk-high) separated by a graben, the Ikang trough.

The evolution of the Calabar Flank is a result of the separation of the African and South American plates. Olade, 1975, Whiteman, 1982, Ofoegbu and Onuoha, 1991, has discussed the origins of the Benue Trough and the Calabar Flank. The various views are however very similar but described the Benue Trough as a failed arm (or aulacogen) of a Cretaceous triple junction, located at the site of the present day Niger Delta, with the other two arms subsequently developing into the South Atlantic Ocean and Gulf of Guinea. According to Olade, 1975, the early stage in the evolution of the trough involved the rise of mantle plume or hot spots in the region of the Niger Delta. This caused doming and rifting of the Benue region developing an R-R-R triple junction. Rifting within the trough was accompanied by rapid subsidence and sedimentation. Sub-crustal contraction and compression of the sediments began when mantle upwelling temporarily ceased.

The Calabar flank consists of Cretaceous to Tertiary sediments classified into eight formations by different authors. The Awi Formation, which is Aptian, in age is the basal stratigraphic unit and consists of calcareous arkosic sandstones resting on the basement surface. The Albian Mfamosing Limestone overlies the Awi Formation. The Mfamosing Limestone is overlain by the Turonian Nkalagu Formation, which consists of a succession of alternating dark grey shales with intercalations of thin calcareous limestone bands. This formation was referred to as Eze-Aku Shale and Awgu Shale, as well as the alternating shales and limestones of the Odukpani Formation. The Nkalagu Formation was later described as Ekenkpon Shale. The Ekenkpon Shale is overlain by Coniacian to Early Santonian New Netim Marl. Some fragments of volcanic bodies have been found in the Nkalagu Formation at Anua-1 and Ikono-1 wells. Unconformably overlying the New Netim marls is the Campanian-Maastrichtian Nkporo Shale, which consists of dark grey to bluish-black, friable to flaggy carbonaceous shales with bands of marly and silty to sandy shales and mudstones. The Imo Shale, Ameke Formation and Benin Sandstone are Tertiary to Recent sediments overlying the Nkporo Shale. The general stratigraphy of the Calabar Flank is summarized in the table 1.1 below.

Table 1.1: Stratigraphic Sequence in the Calabar Flank

	AGE	FORMATION	LITHOSTRATIGRAPHIC DESCRIPTION	DEPOSITIONAL ENVIRONMENT
T E R T I A R Y	OLIGOCENE TO RECENT	Benin Formation	Pebbly sands and gravels	Continental
	EOCENE	Ameke Formation	Medium grained pebbly sandstones, clayey sandstones, calcareous silts, clay and thin limestones	Paralic
	PALEOCENE	Imo Shale	Clayey shale, clay ironstone bands, thin sandstone and sandy limestone bands	Paralic
C R E T A C E O U S	MAASTRICHTIAN	Nkporo Shale	Gypsiferous dark grey shales with ironstone intercalation	Shallow marine
	CAMPANIAN		Unconformity	
	SANTONIAN	New Netim Marl	Marlstones with shale intercalations	Marine
	CONIACIAN			
	TURONIAN	Ekenkpon Shales / Nkalagu Formation	Thick black pyritic shales with intercalations of mudstones, sandstones, ironstones and oyster beds	Marine
	CENOMANIAN			
	ALBAIN	Mfamosing Limestone	Stromatolitic fossiliferous limestones.	Marine
	APTIAN	Awi Formation	Arkosic sandstones interbedded with shales	Fluvio - deltaic
	PRECAMBRIAN	Oban Basement Complex	Crystalline basement rocks	

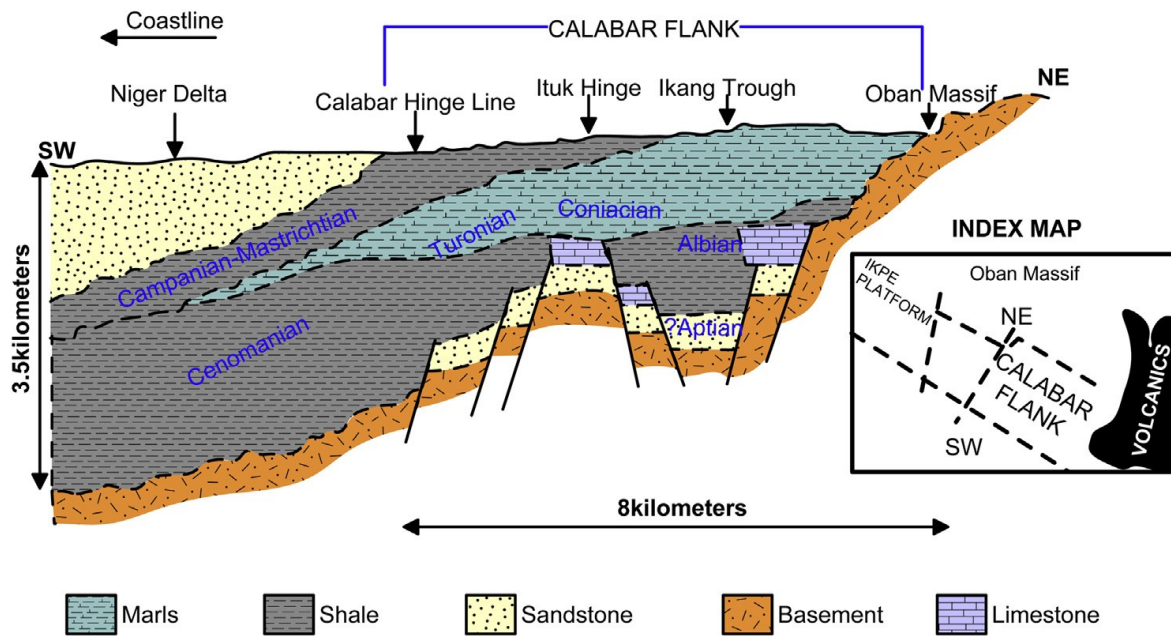


Figure 1.3: Idealized Geological Cross-Section of the Calabar Flank Showing The Main Structural Features and Sequences (Nyong And Ramanathan, 1985).

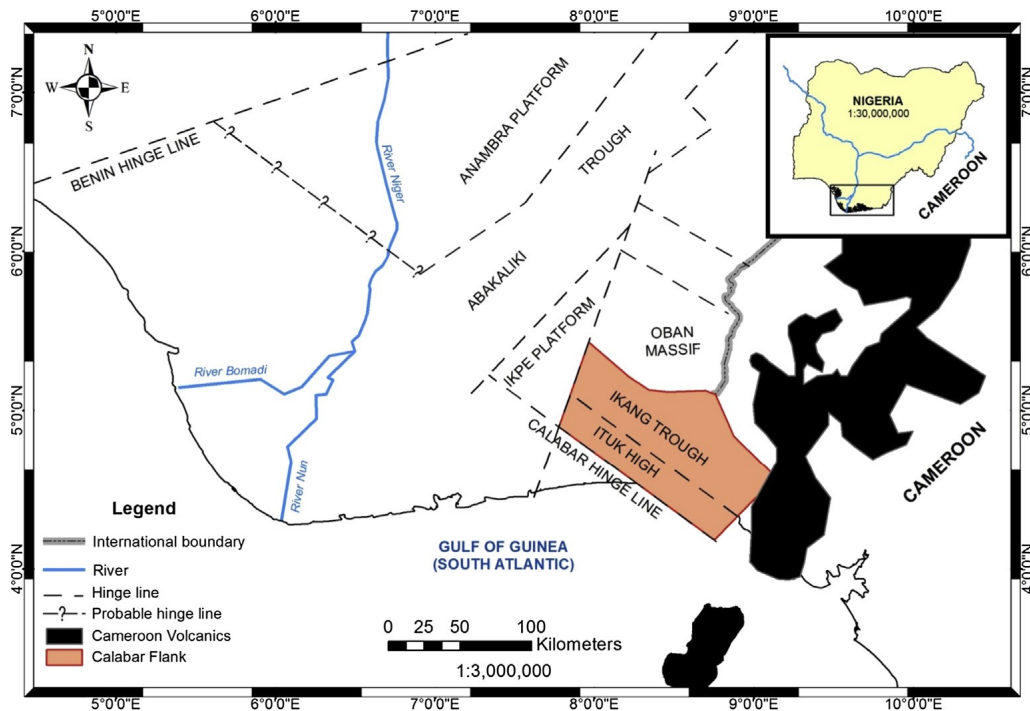


Figure 1.4. The Map of Niger Delta Showing Structural Elements and the Calabar Flank in Relation to Other Sedimentary Basins in Nigeria. (Nyong and Ramanathan, 1985).

1.7 Climate and Vegetation

The climate of the study area is a humid tropical climate (3000mm rain fall) and prevails over Cross River State, except on the Obudu Plateau.

Also, the vegetation ranges from mangrove swamps, through rainforest, to derived savannah, and montane parkland. Just as its rocks are diverse, so also are the mineral resource potentials of the State.

CLMATE: The climate condition of the study area is characterized by uniformly high temperature and a seasonal distribution of precipitation. A tropical wet and dry season prevails in the area. The dry season runs through the months of November to March and the rainy season which begins in April and ends in October with a short period of reduced rains in August commonly referred to as “August break”. The southwards moving Sahara air mass causes the dry season which is associated with extreme aridity, a dusty atmosphere, lowering of water levels and intense leaf fall. The rainy season follows the northward advance of maritime air from the Atlantic Ocean. July and August are usually the wettest periods of the rainy season. The conventional nature of the heavy rainfall results in alternating periods of sunny and rainy conditions.

The highest temperature occurs in February and March at the end of the dry season. The lowest temperatures occur in July, August and September. These months have the highest degree of cloudiness, which reduces insulation and causes lowering of day-time temperatures. The mean temperatures of the study area therefore, are 22.5°C at the minimum and maximum of 31.9°C.

VEGETATION: The study area has displays typical characteristics of the tropical rainforest with multitude of evergreen trees, climbing plants, parasitic plants that live on the other plants and creepers. Some of the areas enjoy luxuriant vegetation with high forest zone (rain forest) in the south and sub-savannah forest in the northern fringe. Similarly, the vegetation of Ugep ranges from mangrove swamps, through rain forest, to derived savannah and montane parkland. Just as its rocks are diverse, so also are the mineral resource potentials of the area.

1.8 Physiography and Mineralization of Study Area

In the Basement Complex, mineralization includes tin and gold (mined in colonial days from Akwa Ibami and Akamkpa), ilmenite, columbite-tantalite, kaolin, graphite, manganese and marble; while in the sedimentary basins are high quality limestones, salts, barytes, leadzinc, and uranium prospects.

Also Unconformably on the Cretaceous Calabar Odukpani Flank, is the thick Tertiary sequence of the Cross River Delta which has built out onto the continental shelf where deep submarine canyons (e.g. the Calabar Canyon) have been incised, with deep sea fans building out onto the ocean floor and providing excellent petroleum traps.

In terms of physiography, the Calabar Flank is a sedimentary basin and extends from the southern margin of the Oban Basement complex to the boundary with the Niger Delta. Here, sudden sediment thickening demarcates the Niger Delta Basin that formed as the latest of a series of basins in the Benue Trough, diagonally crossing Nigeria from the southwest to the northwest.

Northwest-southern trending basement structures underlie the Calabar Flank and define the Itu High and the Ilang Trough, thus relating the Calabar Flank to the South Atlantic Cretaceous marginal basins with similar horst-and-graben structures in Angola and Gabon. The sedimentary succession on the Calabar Flank is mostly of Cretaceous age, comprising an ancient river-borne sandstone, the Awi Formation; and the overlying marine Odukpani Group of Albian to Late Cretaceous age.

The Odukpani Group comprises the Mfamosing Limestone, the Ekenkpon Shale and the New Netim Marl, which are all exposed near the Odukpani local government area headquarters. This is unconformably covered by the Nkporo Shale. Tertiary marine shales and regressive sandstones overlie the Cretaceous succession. The total sediment thickness in the surfaces of the Calabar Flank is over 3500m.

Basically, the sedimentary basins, of Cretaceous Tertiary age, are found in the Ikorn Depression (Mamfe Rift), the Cross River Plain, and the Calabar Flank. Structurally, the Cross River Plain is

underlain by the Ogoja syncline and the Abakaliki uplift wherein lie thick Cretaceous sandstones, marine shales and limestones of the Asu River Group and the Cross River Group.

The Ikorn depression is filled with over 3 km of Cretaceous sandstones and mudstones and Tertiary basalts. Along the Calabar Flank is a thick sequence of shales and the karstic carbonates of the Mfamosing Limestone, with caves. Located on Nigeria's southeastern frontier, the Cross River landscape descends precipitously from the Oban-Obudu rugged foothills (1000 - 2000m) of the Cameroun Mountains on the east, into the Cross River Plains (30m) to the west, and down to the Bight of Bonny coastal plains to the south, Coastal mangrove wetlands interlaced with creeks, virgin rainforest on the Oban-Obudu hills, montane parkland on the Obudu Plateau, and derived Savannah on the Cross River Plain, are all parts of the Cross River State vegetation and scenery.

1.9 Drainage

The study area is drained mainly by the Cross River with many tributaries such as Aboine, Enyong, Udene and Iyiokwu Rivers which in turn empties into the Atlantic Ocean. The Rivers are perennial and usually overflow their banks at the peak of the rainy season. The high rate of runoff and the dense mature drainage pattern makes the soils generally perfect to imperfectly drain.

1.10 Geology of Study Area

1.10.1 Structural Pattern Geology

The Calabar Flank is that part of the southern Nigerian sedimentary basin characterized by crustal block faulting and is bounded by the Oban Massif to the north and the Calabar hinge line delineating the Niger Delta basin in the south. It is also separated from the Ikpe platform to the west by a NE-SW trending fault. In the east, it extends up to the Cameroon volcanic ridge. The Cretaceous shales exposed in the Calabar Flank are unique in that the whole Upper Cretaceous sequence is exposed in outcrops within a narrow strip of about 8 km. The total sediment thickness

is over 3500 m, with a feathered edge of outcrops north of Calabar along the margin of the Oban basement.

The ages of the sedimentary rocks in the Calabar Flank range from Aptian to Campanian Maastrichtian. Sedimentation started with deposition of the Awi Formation (Adeleye and Fayose, 1978) consisting of fluvio-deltaic shales, mudstone, and arkosic sandstone, dated to be of Aptian age. This stratigraphic unit unconformably overlies the base ment complex.

The Awi Formation is directly overlain by platform carbonates of the Mfamosing Limestone Formation (Petters, 1982), deposited in various environmental settings during the first significant marine transgression in the Gulf of Guinea in Mid-Albian times. A hard ground separates the carbonate build up from a thick sequence of black, highly fissile shales with minor intercalations of marls, calcareous mudstones and shell beds belonging to the Ekenkpong and New Netim Formations and this thick sequence spans late Albian-Cenomanian-Turonian age. Santonian and early Campanian sedimentary rocks have not been reported in the Calabar Flank, probably representing a period of non-deposition and/or erosion.

Cretaceous rocks in the Flank are capped by dark grey carbonaceous, friable shales with intercalation of mudstone and gypsiferous beds of the Nkporo Shale (Reyment, 1965). The Nkporo Shale Formation is late Campanian-Maastrichtian in age and was deposited in various environmental settings including shallow open marine, paralic and continental regimes. The lithostratigraphy of the Calabar Flank outcrops is as shown in table 1.1.

In the Calabar Flank, evidence from ammonites and planktonic foraminifera (Nyong and Ramanathan, 1985) support the presence of three major transgressive episodes with oxygen-deficient conditions that resulted in the deposition of dark-colored organic rich shales during the Barremian-Aptian-Albian, Cenomanian-Turonian and, to a lesser extent, Coniacian-Santonian stages. The basement structures of the Calabar Flank are aligned parallel to those of the coastal basins of Gabon, Congo and Angola. These structures were produced during the opening of the South Atlantic Ocean. Except for the absence of evaporites which were closed off from the Calabar Flank by the Guinea Ridge, there are considerable lithologic similarities including carbonate development between the SW-African coastal basins and the Calabar Flank.

They are classified as components of a typical divergent, rafted continental margin and in general can be linked to a single evolutionary geologic history.

The term Calabar Flank was first proposed by Murat (1972) for that part of the southern sedimentary basin in the Niger Delta of Nigeria characterised by crustal block faulting. It was formed by incipient rifting during the breakaway of South America from Africa and the opening of the South Atlantic in Albian times (Whiteman, 1982) with the basement structures that align parallel to those underlying the coastal basins of Gabon, Congo and Angola.

The structures in these basins formed during the opening of the South Atlantic Ocean are similar, except for the absence of evaporates in the Calabar Flank which were prevented from deposition by the Guinea Ridge (De Ruiter, 1978). There is considerable lithologic similarity including carbonate development between the West African South Atlantic Coastal basins and the Calabar Flank. They are therefore classified as components of a typical divergent, rafted continental margin, and in general can be linked to a single evolutionary geologic history. The Cretaceous sedimentary rocks of the Calabar Flank are unique in that the whole Upper Cretaceous sequence is exposed in outcrops within a narrow strip of about 8 km.

Therefore, the recent discovery of oil seeps in the Calabar Flank has generated renewed interest in appraising the petroleum potential of the area.

For a better understanding of the hydrocarbon generation potential of the Calabar Flank, a previous study conducted (Odumodo, 2012) detailed geochemical and organic petrographic studies with the aim of reconstructing paleoenvironmental control on the deposition of organic-rich shales in the Calabar Flank. Previous studies (Adeleye and Fayose, 1978; Petters, 1982; Reyment, 1965) on the Cretaceous sedimentary rocks that outcrops in the Calabar Flank are mostly limited to geological descriptions. Preliminary geochemical studies include organic geochemical appraisal (Essien et al., 2005), geochemical studies of subsurface limestone (Ekwere, 1993) and geochemistry and organic petrography (Ekpo et al., 2012).

The study demonstrates the use of Rock-Eval pyrolysis and biomarker data in elucidating the source (marine or terrigenous), quality, maturation status and depositional environment of the Calabar Flank Cretaceous sedimentary rocks with a view to comparing on a regional basis our data with that of the marginal basins of Brazil and West Africa: Gabon, Cabinda and Angola.

Detailed studies of this kind have not been conducted for this region and the results will provide a better understanding of the petroleum potential of this sedimentary basin and may serve as one

of exploration inland frontier basins that would lead to a major petroleum exploration direction in Nigeria.

The tectonism in Southern Nigeria probably started in Early Cretaceous, with the separation of Africa from South American and opening of the Atlantic. This resulted in the development of the Benue Trough which stretched in a NE-SW direction and resting unconformably upon the Pre-Cambrian basement complex. It extends from the Gulf of Guinea to the Chad Basin and is thought to have been formed by the Y-shaped (RRR) triple junction ridge system that initiated the breaking and dispersion of the Afro-Brazilian plates in the Early Cretaceous (Kogbe, 1989). After the evolution of the Benue Trough, sediments started depositing into the trough with Asu River Group being the oldest sediment followed by Ezeaku Group, and Awgu Group respectively (Nwajide, 1990).

Santonian age marked the stage when the basin experienced another phase of tectonic event that involved deformation, folding, faulting and uplift to the Pre-Santonian sediments leading to the formation of Anambra Basin which evolved as a depression to the west of the uplift (Benkhelil, 1987). Anambra Basin is a Cretaceous depo-centre that received Campanian to Tertiary sediments (Nwajide, 1990 and Obi, 2000).

In Anambra Basin, the strongly folded Albian-Coniacian succession (Pre-Santonian sediments) is overlain by nearly flat-lying Campanian-Eocene succession. The oldest sediment in the Anambra Basin is Nkporo Group (Nwajide, 1990). It was deposited into the basin in Late Campanian, comprising Nkporo Shale, Owelli Sandstone and Enugu Shale (Reyment, 1965 and Obi, 2001).

Nkporo Group is overlain by Mamu Formation. It was deposited in Early Maastrichtian (Kogbe, 1989 and Obi, 2000). It comprises succession of siltstone, shale, coal seam and sandstone (Kogbe, 1989). Ajali sandstone (Maastrichtian) overlies Mamu Formation (Reyment, 1965 and Nwajide, 1990) which is mainly unconsolidated coarse-fine grained, poorly cemented; mudstone and siltstone (Kogbe, 1989). Ajali Sandstone is overlain by diachronous Nsukka Formation (Maastrichtian-Danian) which is also known as the Upper Coal Measure (Reyment, 1965). Imo

Shale (Paleocene) overlies Nsukka Formation (Nwajide, 1990). It comprises clayey shale with occasional ironstone and thin sandstone in which carbonized plants remains may occur (Kogbe, 1989). The Eocene stage was characterized by regressive phase that led to deposition of Ameki Group.

1.10.2 Stratigraphic Pattern Geology

The Calabar flank is a sedimentary basin that borders southeastern Nigeria's continental margin. According to Reijers and Petters (1987), the Calabar Flank is at right angles to the major rift faults of the Benue Trough and structurally consists of NW-SE trending basement horsts (the Oban massif and the Ituk-high) separated by a graben, the Iking trough.

The evolution of the Calabar Flank is a result of the separation of the African and South American plates. Burke *et al* (1972), Olade (1975), Whiteman (1982), Ofoegbu and Onuoha (1991), has discussed the origins of the Benue Trough and the Calabar Flank. The various views are however very similar. Burke *et al* (1972) described the Benue Trough as a failed arm (or aulacogen) of a Cretaceous triple junction, located at the site of the present day Niger Delta, with the other two arms subsequently developing into the South Atlantic Ocean and Gulf of Guinea. According to Olade (1975), the early stage in the evolution of the trough involved the rise of mantle plume or hot spots in the region of the Niger Delta. This caused doming and rifting of the Benue region developing an R-R-R triple junction. Rifting within the trough was accompanied by rapid subsidence and sedimentation. Sub-crustal contraction and compression of the sediments began when mantle upwelling temporarily ceased.

The Calabar flank consists of Cretaceous to Tertiary sediments classified into eight formations by different authors. The Awi Formation, which is Aptian, in age is the basal stratigraphic unit and consists of calcareous arkosic sandstones resting on the basement surface. The Albian Mfamosing Limestone overlies the Awi Formation. The Mfamosing Limestone is overlain by the Turonian Nkalagu Formation, which consists of a succession of alternating dark grey shales with intercalations of thin calcareous limestone bands. This formation was referred to as Eze-Aku Shale and Awgu Shale, as well as the alternating shales and limestones of the Odukpani

Formation. The Nkalagu Formation was later described by Nyong (1995) and Petters (1982) as Ekenkpon Shale. The Ekenkpon Shale is overlain by Coniacian to Early Santonian New Netim Marl. Some fragments of volcanic bodies have been found in the Nkalagu Formation at Anua-1 and Ikono-1 wells. Unconformably overlying the New Netim marls is the Campanian-Maastrichtian Nkporo Shale, which consists of dark grey to bluish-black, friable to flaggy carbonaceous shales with bands of marly and silty to sandy shales and mudstones. The Imo Shale, Ameki Formation and Benin Sandstone are Tertiary to Recent sediments overlying the Nkporo Shale.

CHAPTER TWO

LITERATURE REVIEW

2.1 Review of Previous Works on Aeromagnetism and Landsat-ETM Studies

For HRAM and Landsat-ETM studies:

Ofoegbu and Onuoha (1991) based on spectral analysis of aeromagnetic data over Afikpo area, obtained depth to basement range of 1.2 km to 2.5 km in the Abakaliki anticlinorium. Another study estimated a depth to basement of 3.574 km in the neighboring Nkalagu area. Kogbe (1989) speculated that the total thickness of Cretaceous sediments in Nigeria is about 3.3 km.

Opara (2014), using the spectral plot of aeromagnetic data of this area, revealed the average depth to the basement represented by the D2 values as 2.289 km and proposed that this layer may be attributed to magnetic rocks that have intruded onto the basement surface. They also found the study area to have a mean sedimentary thickness of 2.289 km and noted the abundance of intrusives and the shallow basement depth as not conducive for hydrocarbon generation and accumulation. The Rose diagram of the lineaments of the study area shows dominant structural trends of NW-SE and NE-SW directions

This depth to source interpretation of aeromagnetic field data provides important information on basin architecture for petroleum exploration and for mapping areas where there is shallow basement that may be related to mineral exploration.

Geothermal / Curie Depth Point studies:

Odumodu (2012), obtained the geothermal gradient in the area as between 30°C/km and 45°C/km, with a corrected average of 38.8°C/km. They also observed elevated temperatures at depths of 1000 m, 2000 m, and 3000 m, attributable to such factors as volcanic intrusion into the sediments, the shallow depth to basement, increase in Shaliness (reduction in sand percentage), upward transmission of hotter fluids through the faults, and closeness to the Cameroun volcanic line. He derived a cross section which shows the presence of high temperature plumes at some depths within the Ikpe Platform, Ituk High and the Iking Trough. However towards the surface, these high temperatures are lowered by the thick pile of Benin Sands. The high temperature plumes at the Calabar Flank are as a result of intrusive rocks in the sediments, nearness to the basement, and fluid transmission associated with fault and fracture systems in the area.

According to Odumodu (2012), the description above gives a general picture of the temperature field in the Calabar Flank and parts of the Niger Delta. The high temperature anomalies are coincident with the Ituk High (the horst block) where Anua-1 and Uruan-1 wells with sediments containing intrusives are located, the Ikang Trough (the graben block) and the Ikpe Platform. These sediments range from Cretaceous to Tertiary in age. However, west of the Ituk High, lower temperature anomalies were observed in the Tertiary sediments of the Niger Delta. The high temperature anomalies in the Calabar Flank may be attributed to faulting and associated volcanism in the basement rocks. The fractures and faults within the basement underlying the Ituk High, the Ikang Trough and the Ikpe Platform are possible conduits for upward migration of warmer fluids into the sediments. The shape and size of the high temperature trends vary with depth. At shallow depths (< 1000 m), the anomalies are widely distributed over the Calabar Flank. At deeper levels (2000 – 3000 m), they become more restricted and more closely associated with active fault zones, regional structural highs, and anticlines.

2.2 Theoretical Framework

2.2.1 Principles of Aeromagnetic (Airborne Magnetic) Survey

An aeromagnetic survey is a common type of geophysical survey carried out using a magnetometer aboard or towed behind an aircraft. It is the oldest potential field method used for hydrocarbon exploration. The aeromagnetic geophysical method plays a distinguished role when compared with other geophysical methods in its rapid rate of coverage and low cost per unit area explored. The principle is similar to a magnetic survey carried out with a hand-held magnetometer, but allows much larger areas of the earth's surface to be covered quickly for regional reconnaissance. The aircraft typically flies in a grid-like pattern with height and line spacing determining the resolution of the data (and cost of the survey per unit area).

As the aircraft flies, the magnetometer records tiny variations in the intensity of the ambient magnetic field due to the temporal effects of the constantly varying solar wind and spatial variations in the earth's magnetic field, the latter being due both to the regional magnetic field, and the local effect of magnetic minerals in the earth's crust. By subtracting the solar and

regional effects, the resulting aeromagnetic map shows the spatial distribution and relative abundance of magnetic minerals in the upper levels of the crust. Different rock types differ in their content of magnetic minerals; hence, the magnetic map allows a visualization of the geological structure of the upper crust in the subsurface, particularly the spatial geometry of bodies of rock and the presence of faults and folds.

Aeromagnetic data was once presented as contour plots, but now is more commonly exposed as colored and shaded computer generated pseudo-topography images. The apparent hills, ridges and valleys are referred to as aeromagnetic anomalies, while the differences between actual measurements and theoretical values indicate anomalies in the magnetic field. These anomalies in turn represent changes in rock type or in thickness of rock units.

2.2.2 Geologic Applications of Aeromagnetic Data

Aeromagnetic surveys are an extremely useful tool in geophysical and geologic exploration.

- i. The main purpose of the aeromagnetic surveys is to detect minerals or rocks that have unusual magnetic properties which reveal them by causing anomalies in the intensity of the earth's magnetic field.
- ii. They provide generalized geologic information over a generalized area for ground investigation follow up.
- iii. They can be used to outline different geologic units between widely spaced ground transverses which thus speeds the compilation of provisional geologic map. In areas of deep weathering where geologic relationship are obscured, aeromagnetic data may be used for more accurately indicate the presence and configuration of other units.
- iv. In oil exploration, aeromagnetic data are particularly useful in the estimation of the depth to basement rocks, which cast light on the existence and geometry (thickness) of the sedimentary basin in previously unexplored area.

- v. In geotechnical and archaeological investigations, magnetic surveys may be used to delineate zones of faulting in bedrock and to locate buried metallic man made features such as pipeline, old mines, etc.
- vi. In the absence of rocks with magnetic properties, aeromagnetic data can provide information on the nature, type and form of the crystalline basement.
- vii. Magnetic surveys are effective in determining geometry of sedimentary basins and in defining major masses of extrusive and intrusive igneous rocks. For example, using the geometry of an intrusive mass inferred from magnetic data, it is possible to infer the spatial stress patterns produced by the forceful intrusion of the mass. The relationship between intrusive masses is often apparent from regional magnetic surveys.
- viii. Earthquake Hazards and Site Evaluation - Regional magnetic studies are not normally useful in engineering geology studies of specific sites but can be of considerable value in investigations of earthquake hazards. Magnetic data have proven very useful in determining location and attitudes of faults in several areas including faults of the San Andreas system in California.
- ix. Ground-water Studies - With the increased emphasis on appraisal and development of total ground-water resources of large regions, regional geophysical studies have become increasingly important to ground-water investigations. Ground water is now being developed from great depths in several basins in the world and magnetic data are useful in determining depth and structure of these basins.

2.2.1.2

ROCK MAGNETIC PROPERTIES

Aeromagnetic maps represent magnetic-field variations caused by differences in the total magnetization of underlying sources. Total magnetization is the vector sum of induced and remnant components. The induced component of a rock is the product between the Earth's present-day magnetic field vector and the magnetic susceptibility. Magnetic susceptibility is a scalar measure of the quantity and type of magnetic minerals (commonly Titanomagnetites) in the rock. The remnant component (also a vector) is based on the permanent alignment of magnetic domains within magnetic minerals and is measured using Paleo-magnetic methods.

Igneous and crystalline metamorphic rocks commonly have high total magnetizations compared to other rock types, whereas sedimentary rocks and poorly consolidated sediments have much lower magnetizations. Total magnetizations of volcanic rocks are normally dominated by the remnant component, whereas those for all other rock types are dominated by the induced component, with the exception of some mafic metamorphic rocks. Aeromagnetic anomalies over volcanic rocks commonly produce high-amplitude positive or negative anomalies. Where a correspondence between volcanic edifices and anomaly shape can be demonstrated, positive and negative anomalies indicate normal and reversed-polarity remnant polarities of the rocks respectively.

Theoretically, the magnetic methods are based on the measurement of the small variation in the distribution of the magnetized or polarized rocks.

A sedimentary basin is any depression that has accumulated sediment from the basement rocks. If it contains numerous magnetic rocks such as igneous intrusions or extrusive, magnetic sediments or magnetic metamorphic units, these can provide information on the morphology of the sedimentary basin and its structure. However, if the magnetic units in the basement occur at the basement surface, then the depth determinations for these will map the basin floor morphology. This approach has been used for several decades to locate sedimentary basins with significant thicknesses of sediment (Gunn, 1997).

Depth to basement, faults in the basement surface and relief of the basement have direct relevance to the depositional and structural history of a basin. Many examples exist of positive

basement block being directly related to depositional isopachs and / or structure which reflect the underlying basement structure. In general, igneous rocks have higher content of magnetic minerals especially magnetite than sedimentary rocks and can be identified and mapped in the sedimentary basin from the magnetic data. Igneous features such as intrusive plugs, dykes, sills, lava flows and volcanic centres can occur at any stage of a basin's evolution and therefore be preserved at any level in the sedimentary section. Such features are significant in understanding the history of a basin and assessing its petroleum or mineral prospectivity. Igneous intrusions can produce structural closure and here, magnetic anomalies can be indicators of hydrocarbon traps.

In sedimentary sections, magnetic anomalies caused by non – igneous sources with sediments, are typically weaker than those due to the basement and metamorphic rocks which generally contain much greater concentrations of the magnetic minerals. Sedimentary layer may be magnetic if they contain enough magnetic minerals. However, they must have structural relief for them to give rise to a magnetic anomaly. Magnetic sheets only have anomalies at the edges. Small concentrations of magnetite in sediment can produce an observable magnetic response. However, in sedimentary environments, detrital is rapidly oxidized to hematite which is marked less magnetic, although hematite can in sufficient concentration produce an observable magnetic effect. Magnetic anomalies may be caused by disseminated pyrrhorte in shale and siltstone. Ilmenite may give also a weak magnetic response and ancient beaches are known to contain enough of this mineral to give a weak observable response

Nevertheless pure salt comprising halite, gypsum and anhydrite is diamagnetic as such it has a negative magnetic susceptibility and as a result normally has a negative magnetic contrast relative to enclosing sediments. In such situation, high sensitivity magnetic survey map salt dome and salt ridge as magnetic lows.

Table 2.1: Typical Magnetic Susceptibilities of Earth Materials.

Rock (Mineral)	Type Susceptibility (c.g.s.)
Magnetite	0.3 -0.8
Pyrrhotite	0.028
Ilmenite	0.044
Specularite	0.004
Iron Formation	0.056
Basalt	0.00295
Diabase	0.00259
Rhyolite	0.00112
Gabbro	0.00099
Granite	0.00047
Other Acid Intrusive	0.00035
Ely Greenstone	0.00009
Slates	0.00005
Sedimentary Rocks	0.00001 to 0.001

2.2.1.3 Aeromagnetic Data Processing

The primary objective of data processing of the aeromagnetic data is to systematically separate the local anomalies from regional magnetic anomalies and for enhancement of these anomalies.

There are several analytical processes and methods used for analysis of aeromagnetic data. They include the following methods: filtering and convolution of aeromagnetic data, reduction to pole, regional- residual separation and depth estimation analysis. These methods are discussed in details for a better clarification.

2.2.1.4 Filtering of Aeromagnetic Map

Filtering is a way of separating signals of different wavelength to isolate and hence enhances any anomalous feature with a certain wavelength. A rule of thumb is that the wavelength of an anomaly divided by three or four is approximately equal to the depth at which the body producing the anomaly is buried. Thus filtering can be used to enhance anomalies produced by features in a given depth range. Traditional filtering can be either low pass (Regional) or high pass (Residual). Thus the technique is sometimes referred to as Regional-Residual Separation.

Bandpass filtering isolates wavelengths between user-defined upper and lower cut-off limits. In geophysical exploration, not every signal may of interest thus; there is always a need for filtration processes. Near surface or shallow anomalous sources usually produce relatively short wavelength disturbance. Practically, in the manual digitization of aeromagnetic map, certain short-wavelengths are eliminated to allow a pass of longer wavelength disturbances of lower wave numbers. This is known as a low-pass filter. The irregularities in aeromagnetic maps are removed by low pass filtering, which thus produces a smoother map than the original. Alternatively, the filter in the Fourier domain is designed to eliminate longer wavelengths and pass shorter ones. This is called a high pass filter. Wavelength filtering is a major consideration in selection of anomalies. In studying a large-scale crustal structure, a low pass filter is employed as small local bodies are of less interest. Similarly, in the investigation of anomalies due to shallow crustal sources, a high pass filtering is employed.

2.2.1.5 Reduction to the Pole (RTP)

Reduction to the Pole (RTP) transformation corrects for the offset between the locations of anomalies (closed highs or lows on a contour map) and their sources that is a consequence of the

vector nature of the Earth's magnetic field. To apply the reduced-to-pole transformation correctly, one must assume that the total magnetizations of most rocks in the study area align parallel or anti-parallel to the Earth's main field. This approach makes it possible to determine from the observed total field the position and depth of the pole that has the magnetic effect equivalent to that of an external source with the inclined magnetization. This technique transforms induced magnetic responses to those that would arise where the sources are placed at the magnetic pole (vertical field). This simplifies the interpretation because for sub-vertical prisms or sub-vertical contacts (including faults), it transforms their asymmetric responses to simpler symmetric and anti-symmetric forms. The symmetric 'highs' are directly centred on the body, while the maximum gradient of the anti-symmetric dipolar anomalies coincides exactly with the body edge. Pole reduction is difficult at low magnetic latitudes, since N-S bodies have no detectable induced magnetic anomaly at zero geomagnetic inclination. Pole reduction is not a valid technique where there are appreciable remanence effects.

The reduction to the pole of magnetic data allows us to have a pseudo magnetic map where the magnetization vector of the rocks and the measured total field both are in vertical direction. The contribution of remnant magnetization is supposed to be insignificant.

2.2.1.7 Regional- Residual Separation

The methods employed in the isolation of the background field from survey data have been discussed extensively in various geophysical literatures. These methods involve either visual and or graphical procedures or analytical methods such as least squares fit. Regional magnetic features are believed to be caused by the properties of materials deep within the earth or put simply are due to the dipole field of the earth. A precise definition of this dipole field of the earth is therefore critical to the definition and interpretation of the anomalies due to near surface mass distribution.

The mapped potential field data are the sum of the effect of all sources causing a magnetic anomaly. In applied geophysics, the problem is to eliminate or reduce to a minimum, the effects

of deep-seated, non-commercial sources with as little distortion of the resultant anomaly as possible. A geophysical anomaly is typically composed of a broad spectrum of frequencies, each frequency being characterized by specific amplitude. The anomalies of interest may be corrupted by multi-frequently “noise” consisting of regional trends, instrument drift, uninteresting geologic variation, etc. If the frequently content of both anomaly and noise is known, and there is no spectral overlap between them, then a filter of interest would be designed to eliminate the noise effects.

The Regional-Residual separation involves a careful analysis of the potential field profile in the area within and beyond the area of immediate concern the map. In most cases such analysis is subjective because limited knowledge is known about the geology of the area under investigation.

2.2.1.8 Depth Estimation

The quantitative interpretation of aeromagnetic survey data can be so complex. However, rigorous analysis is carried out on a routine basis only when simple geometrically models are utilized to represent the subsurface sources. In this study, dyke is considered as the predominant structural source of magnetic anomaly. In exploring sedimentary basins, the assumption is generally made that intrusive rocks within the basement are truncated by erosion at their surfaces. If this is the case, the depth to the top of the dyke is equal to the thickness of the sedimentary section. The intrusives may not be extended upward as the basement surface, therefore, any computed sedimentary thickness is generally considered to be a minimum.

The depth to the top of the source is a useful tool for finding thickness of sedimentary succession, and sometimes for locating major structures in basement rocks. Some anomalies arise from basement rocks may be due to lithologic changes rather than to structural features. In certain geologic situations, the depth to the bottom of magnetic sources is sought where it can correspond to the Curie-temperature.

The depth to the top surface can be estimated from the form of a magnetic profile, at right angles to the strike, and traversing an anomaly centre or its immediate neighborhood. The strike length

can be fairly accurately estimated from the shape of the magnetic anomaly. The depth obtained from a magnetic anomaly is dependent on the selection of appropriate source geometry. Accordingly, the selection of horizontal characteristic parameters can be directly related to the depth of burial.

The traditional depth estimation techniques involve the use of contours, stretched histogram pseudo-colour compositions and first vertical derivative data. But recently there are exciting suite of new-generation depth estimation tools and products. These tools include:

- i. Spectral analysis
- ii. Improved Naudy Automatic Model,
- iii. Matched filter depth separation and slicing,
- iv. Traditional and Extended Euler Deconvolution,
- v. Phillips method,
- vi. Complex amplitude and instantaneous phase,
- vii. Analytic signal,
- viii. Magnetic coherence map,
- ix. Vertical derivative, pass, continuation and directional filters,
- x. Powerful visualization and hard copy composition language and tools.

All the methods are based on the transform of the potential field anomalies into special functions that form gradient peaks and ridges over the sources. These maxima peak values are located directly above the magnetic contacts, depending on an assumed geometric model. All the methods can use the same function to locate the contacts and estimate the source depths

2.2.1.9 Aeromagnetic Data Interpretation

2.2.1.9.1 Qualitative Interpretation

The qualitative interpretation of a magnetic anomaly map begins with a visual inspection of the shapes and trends of the major anomalies.

Qualitative interpretation involves the description of the survey results and the explanation of the major features revealed by a survey in terms of the types of likely geological formations and

structures that give rise to the evident anomalies. Typically, some geological information is available from outcrop evidence within the survey area (or nearby) and very often the role of the geophysical data is to extend this geological knowledge into areas where there is no outcrop information (i.e. extrapolation from the known to the unknown) or to extend mapped units into the depth dimension (i.e. to help add the third dimension to the mapped geology).

After delineation of the structural trends, a closer examination of the characteristic features of each individual anomaly is carried out. These features are:

- i. The relative locations and amplitudes of the positive and negative contour parts of the anomaly,
- ii. the elongation and aerial extent of the contours and
- iii. the sharpness of the anomaly as seen by the spacing of contours (Sharma, 1976):

Accordingly, the following items are taken in considerations during qualitative interpretation of the aeromagnetic map:

- i. In sedimentary regions, particularly where the basement depth exceeds 1.5 km, the magnetic contours are normally smooth and variations are small, reflecting the basement rocks rather than the near surface features (Telford *et al.*, 1998). The magnetic relief observed over sedimentary basin areas is almost always controlled more by the lithology of the basement than by its topography. Meanwhile, in regions where igneous and metamorphic rocks predominate, usually exhibit complex magnetic variations. Deep features are frequently camouflaged by higher frequency magnetic effects originating nearer to the surface.
- ii. Changes in the magnetization of basement rocks a mile or more deep may result in magnetic anomalies up to several thousand gammas (nT) in magnetic readings at the surface. At the same depth, structural relief on the basement surface as great as 900 ft (~ 274.30 m) would seldom produce anomalies larger than 50 gamma. The density of contour lines often provides a useful criterion for indicating structures. The closer the contours, i.e., the greater the gradients, the shallower, in general, is the source. Any sudden change in the spacing over an appreciable distance suggests a discontinuity in depth, possibly a fault.

- iii. The magnetic anomalies of large areal extent reflect a deeper source than small-size anomalies.
- iv. Often, a well-defined boundary between zones with appreciably different degrees of magnetic relief can indicate the presence of a major basement fault.

2.2.1.9.2 Quantitative Interpretation

Quantitative interpretation involves making numerical estimates of the depth and dimensions of the sources of anomalies and this often takes the form of modelling of sources which could, in theory, replicate the anomalies recorded in the survey. In other words, conceptual models of the subsurface are created and their anomalies calculated in order to see whether the earth-model is consistent with what has been observed, i.e. given a model that is a suitable physical approximation to the unknown geology, the theoretical anomaly of the model is calculated (forward modelling) and compared with the observed anomaly. The model parameters are then adjusted in order to obtain a better agreement between observed and calculated anomalies.

2.2.2 Concept of Remote Sensing

Remote sensing refers to the activities of recording, observing, and perceiving (sensing) objects or events in far-away (remote) places. In remote sensing, the sensors are not in direct contact with the objects or events being observed. Electromagnetic radiation normally is used as the information carrier in remote sensing. The output of a remote sensing system is usually an image representing the scene being observed. A further step of image analysis and interpretation is required to extract useful information from the image. In a more restricted sense, remote sensing refers to the science and technology of acquiring information about the earth's surface (i.e., land and ocean) and atmosphere using sensors onboard airborne (e.g., aircraft or balloons) or space-borne (e.g., satellites and space shuttles) platforms.

Depending on the scope, remote sensing may be broken down into:

- i. Satellite remote sensing (when satellite platforms are used),
- ii. photography and photogrammetry (when photographs are used to capture visible light),
- iii. thermal remote sensing (when the thermal infrared portion of the spectrum is used),

- iv. radar remote sensing (when microwave wavelengths are used), and
- v. LiDAR remote sensing (when laser pulses are transmitted toward the ground and the distance between the sensor and the ground is measured based on the return time of each pulse).

The range of remote sensing applications includes archaeology, agriculture, cartography, civil engineering, meteorology and climatology, coastal studies, emergency response, forestry, geology, geographic information systems, hazards, land use and land cover, natural disasters, oceanography, water resources, and so on.

2.2.3 Principles of Electromagnetic Radiation

Remote sensing takes one of the two forms depending on how the energy is used and detected. Passive remote sensing systems record the reflected energy of electromagnetic radiation or the emitted energy from the earth, such as cameras and thermal infrared detectors.

Active remote sensing systems send out their own energy and record the reflected portion of that energy from the earth's surface, such as radar imaging systems.

Electromagnetic radiation is a form of energy with the properties of a wave, and its major source is the sun. Solar energy traveling in the form of waves at the speed of light (denoted as c and equals to 3.108 ms^{-1}) is known as the *electromagnetic spectrum*. The waves propagate through time and space in a manner rather like water waves, but they also oscillate in all directions perpendicular to their direction of travel. Electromagnetic waves may be characterized by two principal measures: wavelength and frequency. The wavelength λ is the distance between successive crests of the waves. The frequency μ is the number of oscillations completed per second. Wavelength and frequency are related by the following equation:

$$C = \lambda \cdot \mu \quad (1)$$

The electromagnetic spectrum, despite being seen as a continuum of wavelengths and frequencies, is divided into different portions by scientific convention. Major divisions of the electromagnetic spectrum, ranging from short-wavelength, high-frequency waves to long-

wavelength, low-frequency waves, include gamma rays, x-rays, ultraviolet (UV) radiation, visible light, infrared (IR) radiation, microwave radiation, and radiowaves.

The visible spectrum, commonly known as the *rainbow of colors* we see as visible light (sunlight), is the portion of the electromagnetic spectrum with wavelengths between 400 and 700 billionths of a meter (0.4–0.7 μm). Although it is a narrow spectrum, the visible spectrum has a great utility in satellite remote sensing and for the identification of different objects by their visible colors in photography.

The IR spectrum is the region of electromagnetic radiation that extends from the visible region to about 1 mm (in wavelength). Infrared waves can be further partitioned into the near-IR, mid-IR, and far-IR spectrum, which include thermal radiation. IR radiation can be measured by using electronic detectors. IR images obtained by sensors can yield important information on the health of crops and can help in visualizing forest fires even when they are enveloped in an opaque curtain of smoke.

Microwave radiation has a wavelength ranging from approximately 1 mm to 30 cm. Microwaves are emitted from the earth, from objects such as cars and planes, and from the atmosphere. These microwaves can be detected to provide information, such as the temperature of the object that emitted the microwave. Because their wavelengths are so long, the energy available is quite small compared with visible and IR wavelengths. Therefore, the fields of view must be large enough to detect sufficient energy to record a signal. Most passive microwave sensors thus are characterized by low spatial resolution. Active microwave sensing systems (e.g., radar) provide their own source of microwave radiation to illuminate the targets on the ground.

2.2.4 Application of Landsat Satellite

The wide range of application of the Landsat data has proved undoubtedly to be a true benefactor of humanity. These applications are listed below:

- i. Agriculture, Forestry And Range Resource:**

In discrimination of vegetative types; crop types, timber types, range vegetation. Measurement of crop acreage by species (estimating yields), measurement of timber acreage and volume by species (Monitoring forest harvest), determination of range readiness and biomass, determination of vegetation vigour, determination of vegetation stress, determination of soil conditions.

- Determination of soil association.
- Assessment of grass and forest fire damage.

ii. Land Use And Mapping:

- Classification of land uses.
- Cartographic mapping and map updating.
- Categorization of land capability.
- Separation of urban and rural categories (Monitoring urban growth).
- Regional planning.
- Mapping of transportation networks.
- Mapping of land – water boundaries.
- Mapping of fractures.

iii. Geology:

- Recognition of rock types.
- Mapping of major geology units.
- Revising geology maps.
- Delineation of unconsolidated rock and soils.
- Mapping igneous intrusions.
- Mapping recent volcanic surface deposits.
- Mapping land forms.
- Search for surface guides to mineralization.
- Determination of regional structures.

iv. Water Resources:

- Determination of water boundaries and surface water area and volume.
- Mapping of floods and flood plains.

- Determination of a real extent of snow and snow boundaries (estimating snow melt runoff).
 - Measurement of glacial features.
 - Measurement of sediment and turbidity patterns.
 - Determination of water depth.
 - Determination of irrigated fields.
 - Inventory of lakes.
- v. **Environment:**
- Monitoring surface mining and reclamation.
 - Mapping and monitoring of water pollution (e.g. tracing oil spills and pollutants).
 - Detection of air pollution and its effects.
 - Determination of effects of natural disasters.

2.2.5 Remote Sensing Data Analysis and Interpretation

Remotely sensed data can be used to extract thematic and metric information, making it ready for input into GIS. Thematic information provides descriptive data about earth surface features. Themes can be as diversified as their areas of interest, such as soil, vegetation, water depth, and land cover. Metric information includes location, height, and their derivatives, such as area, volume, slope angle, and so on. Thematic information can be obtained through visual interpretation of remote sensing images (including photographs) or computer based digital image analysis. Metric information is extracted by using the principles of photogrammetry.

2.2.5.1 Image Interpretation and Photogrammetry

Photographic interpretation is defined as the act of examining aerial photographs/images for the purpose of identifying objects and judging their significance (Colwell, 1997). The activities of aerial photo/image interpreters may include (1) detection/identification, (2) measurement, and (3) problem solving. In the process of detection and identification, the interpreter identifies objects, features, phenomena, and processes in the photograph and conveys his or her response by

labeling. These labels are often expressed in qualitative terms, for example, *likely*, *possible*, *probable*, or *certain*. The interpreter also may need to make quantitative measurements. Techniques used by the interpreter typically are not as precise as those employed by photogrammetrists. At the stage of problem solving, the interpreter identifies objects from a study of associated objects or complexes of objects from an analysis of their component objects, and this also may involve examining the effect of some process and suggesting a possible cause.

Seven elements are used commonly in photographic/image interpretation: tone/color, size, shape, texture, pattern, shadow, and association. Tone/color is the most important element in photographic/image interpretation.

Tone refers to each distinguishable variation from white to black and is a record of light reflection from the land surface onto the film. The more light received, the lighter is the image on the photograph.

Color refers to each distinguishable variation on an image produced by a multitude of combinations of hue, value, and chroma.

Size provides another important clue in discrimination of objects and features. Both the relative and absolute sizes of objects are important. An interpreter also should judge the significance of objects and features by relating to their background.

The *shapes* of objects/features can provide diagnostic clues in identification. It is worthy to note that human-made features often have straight edges, whereas natural features tend not to.

Texture refers to the frequency of change and arrangement in tones. The visual impression of smoothness or roughness of an area often can be a valuable clue in image interpretation. For example, water bodies typically are finely textured, whereas grass is medium and brush is rough, although there are always exceptions.

Pattern is defined as the spatial arrangement of objects. It is the regular arrangement of objects that can be diagnostic of features on the landscape. Human-made and natural patterns are often very different. Pattern also can be very important in geologic or geomorphologic analysis

because it may reveal a great deal of information about the lithology and structural patterns in an area.

Shadow relates to the size and shape of an object. Geologists like low-sun-angle photography because shadow patterns can help to identify objects. Steeples and smoke stacks can cast shadows that can facilitate interpretation.

2.2.5.2 Digital Image Preprocessing

In the context of digital analysis of remotely sensed data, the basic elements of image interpretation, although developed initially based on aerial photographs, also should be applicable to digital images. However, most digital image analysis methods are based on tone or color, which is represented as a digital number (i.e., brightness value) in each pixel of the digital image. As multisensor and high spatial-resolution data have become available, texture has been used in image classification, as well as contextual information, which describes the association of neighboring pixel values. Before main image analyses take place, preprocessing of digital images often is required. Image preprocessing may include detection and restoration of bad lines, geometric rectification or image registration, radiometric calibration and atmospheric correction, and topographic correction.

Geometric correction and atmospheric calibration are the most important steps in image preprocessing. *Geometric correction* corrects systemic and nonsystematic errors in the remote sensing system and during image acquisition. It commonly involves (1) *digital rectification*, a process by which the geometry of an image is made planimetric, and (2) *resampling*, a process of extrapolating data values to a new grid by using such algorithms as nearest neighbor, bilinear, and cubic convolution. Accurate geometric rectification or image registration of remotely sensed data is a prerequisite, and many textbooks and articles have described them with details.

2.2.5.3 Image Enhancement and Feature Extraction

Various image-enhancement methods may be applied to enhance visual interpretability of remotely sensed data as well as to facilitate subsequent thematic information extraction. Image-

enhancement methods can be roughly grouped into three categories: contrast enhancement, spatial enhancement, and spectral transformation.

Contrast enhancement involves changing the original values so that more of the available range of digital values is used, and the contrast between targets and their backgrounds is increased.

Spatial enhancement applies various algorithms, such as spatial filtering, edge enhancement, and Fourier analysis, to enhance low- or high-frequency components, edges, and textures.

Spectral transformation refers to the manipulation of multiple bands of data to generate more useful information and involves such methods as band rationing and differencing, principal components analysis, vegetation indices, and so on.

Feature extraction is often an essential step for subsequent thematic information extraction. Many potential variables may be used in image classification, including spectral signatures, vegetation indices, transformed images, textural or contextual information, multitemporal images, multisensor images, and ancillary data. Because of different capabilities in class separability, use of too many variables in a classification procedure may decrease classification accuracy. It is important to select only the variables that are most effective for separating thematic classes. Selection of a suitable feature extraction approach is especially necessary when hyperspectral data are used. This is so because the huge amount of data and the high correlations that exist among the bands of hyperspectral imagery and because a large number of training samples is required in image classification. Many feature-extraction approaches have been developed, including principal components analysis, minimum-noise fraction transform, discriminant analysis, decision-boundary feature extraction, nonparametric weighted-feature extraction, wavelet transform, and spectral mixture analysis.

2.2.5.4 Image Classification

Image classification uses spectral information represented by digital numbers in one or more spectral bands and attempts to classify each individual pixel based on the spectral information. The objective is to assign all pixels in the image to particular classes or themes (e.g., water,

forest, residential, commercial, etc.) and to generate a thematic “map.” It is important to differentiate between information classes and spectral classes. The former refers to the categories of interest that the analyst is actually trying to identify from the imagery, and the latter refers to the groups of pixels that are uniform (or near alike) with respect to their brightness values in the different spectral channels of the data. Generally, there are two approaches to image classification: supervised and unsupervised classification.

In a *supervised* classification, the analyst identifies in the imagery homogeneous representative samples of different cover types (i.e., information classes) of interest to be used as training areas. Each pixel in the imagery then would be compared spectrally with the training samples to determine to which information class they should belong. Supervised classification employs such algorithms as minimum-distance-to-means, parallelepiped, and maximum likelihood classifiers

In an *unsupervised* classification, spectral classes are first grouped based solely on digital numbers in the imagery, which then are matched by the analyst to information classes. Here the objective is to group multiband spectral response patterns into clusters that are statistically separable. Thus, a small range of digital numbers (DNs) for, say 3 bands, can establish one cluster that is set apart from a specified range combination for another cluster (and so forth).

CHAPTER THREE

3.1 RESEARCH METHODOLOGY

The analysis was accomplished based on certain mathematical developments.

HRAM data:

Four High Resolution Aeromagnetic data sheets were acquired for the purpose of this study. They were flown in Nigeria by Fugro airborne services in surveys for the Nigerian Geological Survey Agency in 2009, and is of higher quality than that of the 1970s. The survey was flown at 500m line spacing and 80m terrain clearance, hence the higher resolution, in digital form. The sheet Aeromagnetic sheets are for Afikpo, Ugep, Uwet, and Ikot-Ekpene. 7.2 Geosoft Oasis-Montaj and Surfer 10 softwares were used for processing of the acquired data.

The aeromagnetic data used were subjected to several filtering operations. The nature of filtering applied to the aeromagnetic data in this study in the Fourier domain (Fourier series) was chosen to eliminate certain wavelengths and to pass certain wavelengths. Several potential field software with different analytical modules were used in the interpretations of the aeromagnetic map. Polynomial fitting was applied to the data for regional-to-residual separation, to expose the residual features as random errors, and reduction-to-pole was applied to minimize polarity effects on the data. Then we did a Fourier Transformation of the digitized aeromagnetic data to compute the energy/power spectrum of the data which was then plotted against frequency on a logarithmic scale. The essence of this process is that the slopes so obtained of the segments, yielded estimates of average depths to magnetic sources of anomaly in the study area. Second vertical derivative filters were applied on the data to define the edges of the bodies and amplify the fault trends, and depth estimates in the study area were obtained by 3D Euler Deconvolution and Spectral analysis with three different procedures, and the results were correlated. The procedures are Peter's slope method, Tiburg rule, and Half-width rule.

Spectral analysis was also used to determine the Curie point depth, Curie temperature and Heat flow of the study area.

Landsat-ETM:

The raw data was first georeferenced with coordinates of the area. After which ILWIS 3.1 Academic software was used to process, enhance and analyze the data, and Arc-View 3.2 software, was used to enhance the lineaments in the study area. The lineament trend directions were then summarized with a rose diagram.

Generated color composites include; RGB 432, RGB 517, RGB 721, an unsupervised Classification Map, and a Normalized Difference Vegetation Index (NDVI).

Other generated maps include a Digital Elevation Model (DEM), Digitized Geological Map, Lineament Density Map, Lineament on Drainage Map, and Lineament on Edge Enhanced Band5 map.

Both data results were then *integrated* for interpreting the geologic, structural, and geothermal features within the study area.

Softwares used are 7.2 Geosoft Oasis-Montaj, Surfer 10.

For the aeromagnetic data, the *magmap* tool (Geosoft Oasis-Montaj, 7.2) offering a number of utilities was implemented to help calculate the magnetic-anomaly grid (total field intensity minus the Definitive International Geomagnetic Reference Field) for the appropriate time of year. After producing the grid the necessary filters were applied to it before displaying the image with the *Grid and Image* tool. A range of imaging routines were applied to visually enhance the effects of selected geologic sources using mathematical enhancement techniques (Milligan and Gunn, 1997). In order to facilitate interpretation, Analytic Signal Amplitude and Two-Dimensional Fast Fourier Transformation (2D-FFT) filters were applied to enhance the quality of the magnetic data. The 2D-FFT filters used included Reduction to Pole, First Vertical Derivative and Upward Continuation Derivative.

For the Landsat-ETM data, the data was subjected to various image enhancement and transformation routines. For the image transformation, band ratios were generated using calculator module in IDRISI32. The ratios generated (3/4, 4/2, 3/1, 5/4) were employed to reduce the effects of shadowing as well as enhance the detection of certain features/ materials. For the image enhancement, 3 band RGB colour composites were created using the composite module of

IDRISI32. This process was employed to enhance the spectral quality of the images. Generated composites include RGB 321, RGB 432, and RGB 541 as well as NDVI.

3.2 Aeromagnetic Data Acquisition

High Resolution Aeromagnetic (HRAM) data of the Calabar Flank, Nigeria were acquired between 2003 and 2009 with the aim of assisting and promoting petroleum and mineral exploration in the basin. The area was flown over by Fugro Airborne Services Limited, Johannesburg, with a flight line spacing of 500 m oriented in NW-SE and a tie line spacing of 2000 m (NGSA, 2010).

3.3 Landsat-ETM Data Acquisition

The seven-band Landsat-ETM image acquired on the 17th of December, 2000, belongs to a scene with Path number 188 and Row number 56 was obtained from the Earth Science Data Interface (ESDI) of the National Aeronautic and Space Agency (NASA). A Shuttle Radar Topographic Mission (SRTM) image of the same area was also obtained. Also, a Shell 1:250,000 geologic map of the Study area was re-digitized.

3.4 Landsat-ETM Data Analysis

The Landsat-ETM data obtained was subjected to various image enhancement and transformation routines. For the image transformation, band ratios were generated using calculator module in IDRISI32.

The ratios generated were studied in detail and information extracted along with those obtained from Digital Elevation Model (DEM) was attributed to colour patterns observed from the Colour composites. The Resulting Data obtained was employed in the classification of the images.

For the purpose of this study, the maximum likelihood classification of IDRISI32 was utilized to perform supervised classification and it involved the following steps:

- i. Training sites were established on composites and digitized with polygons.
- ii. Particular spectral signatures were assigned to each training site using the MAKESIG module in IDRISI32 (which analyzes the pixels within each training site before assigning spectral signatures).
- iii. Classification of the entire image was then embarked on after assigning particular probability values for each signature using the MAXLIKE module in IDRISI32.

Information obtained from the classified images, colour composites as well as the DEM of the Study area were combined in generating a new geologic map for the area.

3.5 High Resolution Aeromagnetic Data Analysis

Interpretation of the aeromagnetic survey data aims to map the surface and subsurface regional structures (e.g., faults, contacts, bodies and mineralization). Aeromagnetic data are mostly analyzed in these processes Aeromagnetic data, filtration (upward and/ or downward continuation, Reduction to pole, vertical derivatives, horizontal derivatives etc.), Regional - Residual Separation, and Depth estimation analysis

3.5.1 Filtering of the HRAM Map

Filtering is a way of separating signals of different wavelength to isolate and hence enhance anomalous features with a certain wavelength. A rule of thumb is that the wavelength of an anomaly divided by three or four is approximately equal to the depth at which the body producing the anomaly is buried. Thus filtering can be used to enhance anomalies produced by features in a given depth range. Bandpass filtering isolates wavelengths between user-defined upper and lower cut-off limits. In geophysical exploration, not every signal may of interest thus; there is always a need for filtration processes. Near surface or shallow anomalous sources usually produce relatively short wavelength disturbance.

Practically, in digitization of aeromagnetic map manually, certain short-wavelengths are eliminated to allow a pass of longer wavelength disturbances of lower wave numbers. This is known as a low-pass filter. The irregularities in aeromagnetic maps are removed by low pass filtering, which thus produces a smoother map than the original. Alternatively, the filter in the Fourier domain can be designed to eliminate longer wavelengths and pass shorter ones. This is called a high pass filter. Wavelength filtering is a major consideration in selection of anomalies. In studying a large-scale crustal structure, a low pass filter is employed as small local bodies are of less interest. Similarly, in the investigation of anomalies due to shallow crustal sources, a high pass filtering is employed.

The Data was passed through non-linear filters, high pass and low pass filters, etc, in order to study both the deeper and shallower sources of magnetic anomalies.

3.5.2 Magnetic Depth Estimation

Often one of the most useful pieces of information to be obtained from aeromagnetic data is the depth of the magnetic source (or rock body). Since the source is usually located in the so-called 'magnetic basement' (i.e. the igneous and metamorphic rocks lying below the -assumed non-magnetic - sediments), this depth is also an estimate of the thickness of the overlying sediments. This is an important piece of information in the early phases of petroleum exploration. Sufficient depth estimates from a large number of magnetic sources allow the depth of the basement to be contoured, giving a rough Isopach map of the sediments.

The methods of magnetic depth estimation were employed in this study, they include, Spectral Methods and the 3D Euler Deconvolution

The spectral method was also used to determine the curie depth point, geothermal gradient and heat flow of the study area.

3.5.2.1 Spectral Analysis

The spectral depth method is based on the principle that a magnetic field measured at the surface can therefore be considered the integral of magnetic signatures from all depths. The power spectrum of the surface field can be used to identify average depths of source ensembles (Spector

and Grant, 1970). This same technique can be used to attempt identification of the characteristic depth of the magnetic basement, on a moving data window basis, merely by selecting the steepest and therefore deepest straight-line segment of the power spectrum, assuming that this part of the spectrum is sourced consistently by basement surface magnetic contrasts. A depth solution is calculated for the power spectrum derived from each grid sub-set, and is located at the centre of the window. Overlapping the windows creates a regular, comprehensive set of depth estimates. This approach can be automated, with the limitation however that the least squares best-fit straight line segment is always calculated over the same points of the power spectrum, which if performed manually would not necessarily be the case.

For small windows of data the limited number of grid nodes often leads to power spectra becoming jagged at the start or end. This is the reason for omitting the first point in the automated determination of the deepest straight-line segment of the power spectra. To define a straight line on the basis of a set of points (in a least squares statistical manner) a minimum of 2 points is required, but more are preferable. Increasing the number of points used to define the straight line segment may conflict with obtaining the deepest characteristic source depths, as the slope of the power spectrum reduces for increasing wave number / decreasing wavelength.

Depth results are generated for the entire dataset using different wave number ranges and window sizes. A potential field grid may be considered to represent a series of components of different wavelength and direction. The logarithm of the power of the signal at each wavelength can be plotted against wavelength, regardless of direction, to produce a power spectrum. The power spectrum is often observed to be broken up into a series of straight line segments. Each line segment represents the cumulative response of a discrete ensemble of sources at a given depth. The depth is directly proportional to the slope of the line segment. Filtering such that the power spectrum is a single straight line can thus enhance the effects from sources at any chosen depth at the expense of effects from deeper or shallower sources.

Most approaches used in estimating depth to magnetic sources of anomaly involve Fourier transformation of the digitized aeromagnetic data to compute the energy (or amplitude) spectrum. This is plotted on the Logarithmic scale against frequency. The plot shows the straight

line segments which decrease in slope with increasing frequency. The slopes of the segments yield estimates of depths to magnetic sources.

Given a residual magnetic anomaly map of dimension $L \times L$ digitized at equal intervals, the residual intervals, and the residual total intensity anomaly values are expressed by Tanaka et al. (1999), in terms of double Fourier series expansion:

$$T(x, y) = \sum_{n=1}^N \sum_{m=1}^M P_m^n \cos\left(\frac{2\pi}{L}(nx + my)\right) + Q_m^n \sin\left[\left(\frac{2\pi}{L}\right)(nx + my)\right] \quad (2)$$

Where L dimension of the block, P_m^n and Q_m^n are Fourier amplitude and N, M are the number of grid points along the x and y directions respectively.

Equation (2) can be combined into a single partial wave thus:

$$P_m^n \cos\left[\left(\frac{2\pi}{L}\right)(nx + my)\right] + Q_m^n \sin\left[\left(\frac{2\pi}{L}\right)(nx + my)\right] = C_m^n \cos\left[\left(\frac{2\pi}{L}\right)(nx + my)\right] - \delta_m^n \quad (3)$$

Where,

$$(P_m^n)^2 + (Q_m^n)^2 = (C_m^n)^2 \quad (4)$$

And δ_m^n is the appropriate phase angle.

Each (C_m^n) is the amplitude of the partial wave. The frequency of this wave is given by: $F_m^n = \sqrt{n^2 + m^2}$ is called the frequency of the wave. Similarly, using the complex form, the two dimensional Fourier transform pair may be written (Bath, 1974)

$$G(U, V) = \int_{-\infty}^{\infty} \int_{-\infty}^{\infty} g(x, y) e^{-j(ux+vy)} dx dy \quad (5)$$

$$g(x, y) = \frac{1}{4\pi^2} \int_{-\infty}^{\infty} \int_{-\infty}^{\infty} G(U, V) e^{-j(ux+vy)} dx dy \quad (6)$$

Where u and v , are the angular frequencies in the x and y directions respectively, $G(u, v)$ when broken up into its real and imaginary parts is given by

$$G(u, v) = P(u, v) + jQ(u, v) \quad (7)$$

The energy density spectrum or simply the energy spectrum is

$$E(u, v) = |G(u, v)|^2 = P^2 + Q^2 \quad (8)$$

The Fourier transform of a section of a magnetic map digitized in a square grid therefore forms a rectangular matrix of coefficients which can be reduced to a set of average amplitude dependent only on the frequency (Hahn *et al*, 1976). These average amplitudes fully present a spectrum from which the depths to magnetic sources can be estimated. Residual total magnetic field intensity values are used to obtain the two dimensional Fourier transforms from which the spectrum is to be extracted. From the residual values $\Delta T(x, y)$ the two dimensional Fourier transform is conducted. Next the frequency intervals are subdivided into subintervals which lie within one unit of frequency range. The average spectrum of the entire partial wave falling within this frequency range is calculated and the resulting values together constitute the radial spectrum of the anomalous field. A plot of the logarithm of the energy values versus frequency consists of linear segments each of which group points due to anomalies caused by bodies occurring within a particular depth. If Z is the mean depth of a layer, the depth factor for this ensemble of anomalies is $\exp(-2ZK)$, where K is the magnetic moment per depth (Spector and Grant, 1970). Thus Logarithmic plot of the radial spectrum would give a straight line whose slope is $2Z$.

The use of this method involved some practical problems mostly of inherent in the application of the discrete Fourier transform (DFT). These include the problems of aliasing, truncating effect or Gibb's phenomenon and the problems associated with the even and odd symmetries of the real and imaginary parts of the Fourier transform. The aliasing effect arises from the ambiguity in the frequency represented by the sampled data. Frequencies greater than the Nyquist frequencies, tend to impersonate the lower frequencies and this is known as the aliasing effect. To avoid or reduce the effect of aliasing, the frequencies greater than the Nyquist frequency must be removed through the use of an alias filter, which provides high attenuation above the Nyquist frequency. Aliasing can also be removed or reduced through the use of an alias filter which provides high attenuation above the Nyquist frequency. Aliasing can also be removed or reduced through the

use of small sampling interval such that the Nyquist frequency is equal to or greater than the highest frequency component present in the function being analyzed.

When a limited portion of the aeromagnetic anomaly is subjected to Fourier synthesis, it is difficult to reconstruct the sharp edges of the anomaly with a limited number of frequencies and this truncation leads to the introduction of spurious oscillations around the region of discontinuity. This is known as Gibbs phenomenon. This truncation is equivalent to the convolution of the Fourier transform of the function with that of a regular window, which is a sine cardinal function. This convolution introduces ripples at the edges of the function, which manifests itself as spurious oscillations at the discontinuity. Increasing the length of the window makes the Fourier transform tends towards a delta function with a subsequent reduction of the ripples at the edges. The function effect can therefore be reduced through the use of short sampling intervals and by selecting a large portion of anomaly or a long profile centered on the feature of interest. An alternative and even more effective approach to reducing the problem of Gibb's phenomenon is by the application of a cosine taper to the observed data.

However, in this research, the analysis of the problems associated with aliasing and truncation or Gibb's phenomenon, have been taken care of by the computer software. An alias filter has been incorporated into the computer program to reduce the aliasing effect and a cosine taper has been applied to the data to reduce the effects of truncation.

3.5.2.2 3D Euler Deconvolution

The objective of the 3D Euler deconvolution process is to produce a map showing the locations and the corresponding depth estimations of geologic sources of magnetic or gravimetric anomalies in a two-dimensional grid (Reid, 1990).

The Standard 3D Euler method is based on Euler's homogeneity equation, which relates the potential Field (magnetic or gravity) and its gradient components to the location of the sources, by the degree of homogeneity N , which can be interpreted as a structural index (Thompson, 1982). The method makes use of a structural index in addition to producing depth estimates.

In combination, the structural index and the depth estimates have the potential to identify and calculate depth estimates for a variety of geologic structures such as faults, magnetic contacts, dykes, sills, etc. The algorithm uses a least squares method to solve Euler's equation simultaneously for each grid position within a sub-grid (window). A square window of predefined dimensions (number of grid cells) is moved over the grid along each row. At each grid point a system of equations is solved, from which the four unknowns (x , y as location in the grid, z as depth estimation and the background value) and their uncertainties (standard deviation) are obtained for a given structural index. A solution is only recorded if the depth uncertainty of the calculated depth estimate is less than a specified threshold and the location of the solution is within a limiting distance from the center of the data window (Whitehead and Musselman, 2008).

Thompson (1982) showed that for any homogenous, three-dimensional function $f(x; y; z)$ of degree n :

$$f(t_x; t_y; t_z) = t_n f(x; y; z) \quad (9)$$

It can be shown that, the following equation, which is known as Euler's homogeneity relation can be satisfied:

$$x \frac{\delta f}{\delta x} + y \frac{\delta f}{\delta y} + z \frac{\delta f}{\delta z} = n f \quad (10)$$

In geophysics, the function $f(x,y,z)$ can have the general functional form:

$$f(x, y, z) = \frac{G}{r^N} \quad (11)$$

Where $r^N = (X - X_0)^2 + (Y - Y_0)^2 + (Z - Z_0)^2$, N a natural number (1, 2, 3...) and G a constant (independent of x , y , z). Many simple point magnetic sources can be described by equation (14), with $(X_0; Y_0; Z_0)$ the position of the source whose field F is measured. The parameter N is dependent on the source geometry, a measure of the fall-off rate of the field and may be interpreted as the structural index (SI). Clearly equation (11) is homogeneous and thus N is equivalent to $-n$ in Euler's equation (10).

Considering potential field data, Euler's equation can be written as:

$$(x - x_0) \frac{\delta T}{\delta x} + (y - y_0) \frac{\delta T}{\delta y} + (z - z_0) \frac{\delta T}{\delta z} = N(B - T) \quad (12)$$

With B the regional value of the total magnetic field and (X₀; Y₀; Z₀) the position of the magnetic source, which produces the total field T measured at (x; y; z).

Thompson (1982) showed that simple magnetic and gravimetric models are consistent with Euler's homogeneity equation. Thus Euler Deconvolution provides an excellent tool for providing good depth estimations and locations of various sources in a given area, assuming that appropriate parameter selections are made.

Though it is a general advantage of the Euler Deconvolution method, that it is applicable to all geologic models and that it is insensitive to the remaining magnetic and geomagnetic inclination and declination, an initial assumption of the source type has to be made. Dependent upon the potential source type, a structural index is chosen. This structural index is also a measure of the distinctive fall-off rate of the geologic feature. For example, the best results for a contact are obtained by structural indices of 0, while for thin two-dimensional dyke structures a structural index of 1 yields the best estimates, as explained on Table 3.1. The number of infinite dimensions describes the extension of the geologic model in space.

Table 3.1: Structural Indices for Simple Magnetic Models Used For Depth Estimations by 3D Euler Deconvolution.

Geologic Model	Number of Infinite Dimensions	Magnetic Structural Index
Sphere	0	3
Pipe	1 (z)	2
Horizontal cylinder	1 (x-y)	2
Dyke	2 (z and x-y)	1
Sill	2 (x and y)	1
Contact	3 (x,y,z)	0

The significance of the location and depth estimates obtained by 3D Euler Deconvolution is given by the specificity of the chosen parameters like the grid cell size, window size, structural index, chosen depth uncertainty tolerance, etc. The selection of the grid cell size should be based on the grid spacing and the wavelength of the anomalies to be analyzed, as the software Geosoft Oasis Montaj allows a square window size of up to 20 grid cell units. If the wavelengths of the anomalies are significantly longer or shorter than the window size, the 3D Euler method does not yield appropriate results. On the other hand, the limiting distance from the centre of the algorithm window, in which solutions are still recorded, should be chosen with respect to the wavelength of potential anomalies. In general, 3D Euler Deconvolution yields results for each window position; therefore it is necessary to eliminate solutions with high uncertainties.

A reliable tool for the limitation of results is the specification of a threshold value for depth and horizontal uncertainties. Geosoft Oasis montaj reports the depth and location uncertainties as percentage of the depth below the recording sensor position. As matter of principle, low Structural Indexs values are associated with source bodies which give rise to low gradients, thus depth estimation solutions with low SI values have high uncertainties. The data quality determines the general level of uncertainty, so an examination of the recorded solutions will define the selection criteria.

The consideration of appropriate solutions should be guided by two aspects. On the one hand, the position (and depth) anomalies should be kept low to improve the accuracy of the computations, on the other hand a sufficient number of solutions must be retained in order to delineate geologic features sought and provide meaningful solutions.

The results of the Euler method are displayed in ordinary maps as point solutions combining the location (position of solution) and the depth (colour range). Given the choice of an appropriate structural index, 3D Euler Deconvolution will lead to a clustering of solutions, which can be interpreted. A vertical pipe structure will for example be shown as a cluster of solutions around a specific point, whereas an elongated dyke structure will be recognized as a linear trend of solutions.

Another approach to limit the solutions obtained by the Euler method is the Located Euler 3D method, which, unlike the Standard Euler method, tests and limits grid locations before

calculating depth estimations by Euler deconvolution. The Located Euler method calculates the analytic signal (3p) and finds peaks in the analytic signal grid. The normal depth estimation by Euler Deconvolution is then only applied to these peak locations.

3.5.3 Geothermal Gradient, Curie Point Depth, and Heat Flow

The Curie point depth is the theoretical surface with a temperature of approximately 580⁰C and can be considered an index of the bottom of a magnetic source, due to ferromagnetic minerals converting to paramagnetic minerals (Kasidi and Nur, 2013). Geomagnetic anomalies, which are retrieved from magnetic survey, can be utilized to study magnetic structures above the Curie point depth. Meanwhile, if temperature on the Earth's surface is also taken into account, the geothermal gradient can be constructed from the temperature difference between the Earth's surface and 580⁰C, divided by the Curie point depth.

As is known, crustal rocks lose their magnetization at the Curie point temperature. At this temperature, ferromagnetic rocks become paramagnetic, and their ability to generate detectable magnetic anomalies disappears. It is also defined as the point at which certain materials lose their permanent magnetic properties, to be replaced by induced magnetism. The Curie temperature is named after Pierre Curie, who showed that magnetism was lost at a critical temperature. The ordered magnetic moments ferromagnetic change and become disordered paramagnetic.

From the slope of the power spectrum, the top bound and the centroid of a magnetic layer are determined. The base depth of the magnetic source ((Okubo et al., 1985; Tanaka et al., 1999) is:

$$Z = 2Z_0 - Z_t \quad (13)$$

. Where Z_0 is the centroid of the magnetic layer and Z_t is the top bound

Heat flow estimates on the crust may therefore be made using the depth and thickness information.

The Curie point temperature at which rocks loss their ferromagnetic properties provides a link between thermal models and models based on the analysis of magnetic sources.

The magnetic susceptibility and strength of the material that make up the continental crust are controlled by the temperature. At temperature higher than the curie point, magnetic ordering is

loose and both induced and remanent magnetization disappear, while for temperatures greater than 580°C those material will begin to experience ductile deformation. The basic relation for conductive heat transport is Fourier's law. In one dimensional case under assumption that the direction of the temperature variation is vertical and the temperature gradient (dT/dz) is constant; Fourier's law takes the form ((Tanaka et al., 1999):

$$\mathbf{q} = - \mathbf{k} \, d\mathbf{T} / d\mathbf{z}. \quad (14)$$

where, qz is heat flow and k is thermal conductivity.

The Curie temperature Θ° can also be defined (Tanaka et al., 1999) as:

$$\Theta = (dT/dz)d \quad (15)$$

Where, d is the curie-point depth (as obtained from the spectral magnetic analysis).

The surface temperature is 0°C and dT/dz will remain constant provided there are no heat sources or heat sinks between the earth's surface and the curie-point depth. The Curie temperature depends on magnetic mineralogy.

For example although the curie temperature of magnetite (Fe^3O^4) is at approximately 580°C, an increase of titanium (Ti) contents of titano-magnetite will causes a reduction of the curie temperature. A Curie point temperature of 580°C and thermal conductivity of $2.5\text{Wm}^{-1}\text{C}^{-1}$ which is the average thermal conductivity for igneous rocks is used in the study as standard (Nwankwo *et al* 2009).

CHAPTER FOUR

RESULTS AND DISCUSSION

4.1 AEROMAGNETIC DATA: TOTAL MAGNETIC FIELD INTENSITY

The maps were digitized at 1.0 km interval to avoid the problem of frequency aliasing. After digitization each map was contoured using a set of computer software programs (A2XYZ, P2GRD, DETOUR, and CONTOUR). The digitized map was then contoured and the Total Magnetic Field Intensity Map of the Study area, contoured in gammas, was thus generated and is as shown in Fig. 4.1 and 4.3. The 3-D Surface map of TMI is also shown in Fig 4.2.

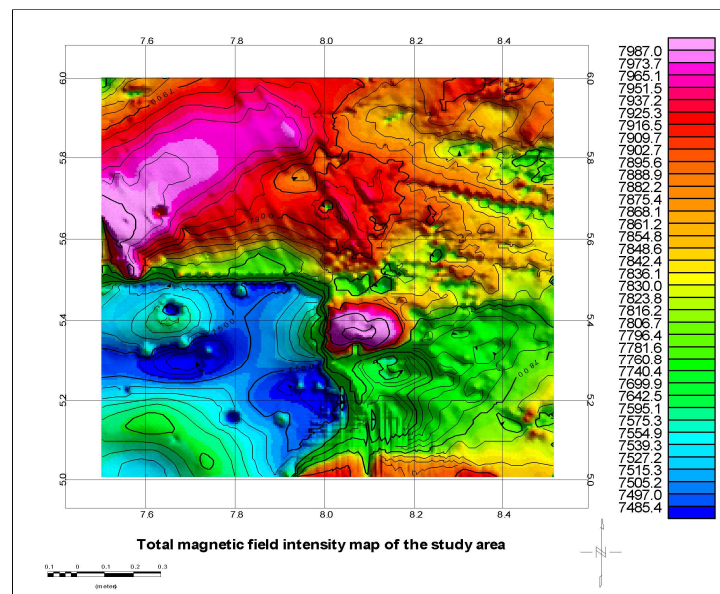


FIG. 4.1: TOTAL MAGNETIC FIELD INTENSITY MAP OF THE STUDY AREA

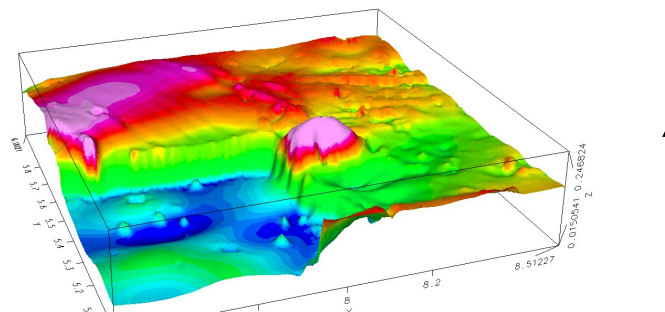


FIG. 4.2: 3D TOTAL MAGNETIC FIELD INTENSITY MAP OF THE STUDY AREA

distribution on the basis of parent materials as 0.21 ± 0.07 , 0.30 ± 0.26 , 0.33 ± 0.09 , 0.36 ± 0.11 and 0.40 ± 0.60 for soils from Imo clay-shale group, Bende-Ameki group (Osemwota et al, 2008).

Very high TMI values between 7987.0 – 7973.7gammas also occurs at the SE part of the TMI map, at a central position on the map. It is also colored light-pink, and geologically cuts slightly across the Bende-Ameki Group, and then Mamu Formation and Nkporo Shale/Afikpo Sandstone.

Conversely, very low TMI value ranges from 7539.3 gammas – 7485.4gammas was observed all over the SW part of the TMI map of the study area, and this coincides with the underlying Coastal Plain Sands.

The Total Magnetic Intensity of the study area was also contoured in gammas, as shown in Figures 4.4 and 4.5.

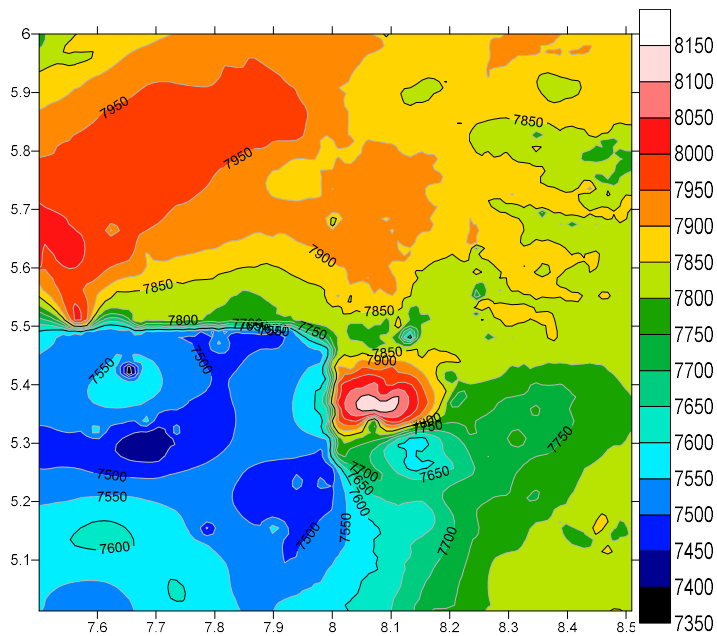


Fig. 4.4

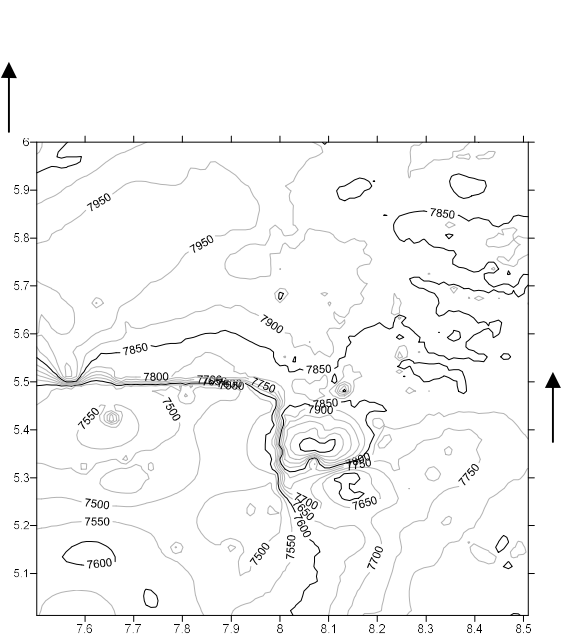


Fig. 4.5

FIG. 4.4: COLOUR SHADED PIXEL MAP OF THE TOTAL MAGNETIC FIELD INTENSITY OF THE STUDY AREA CONTOURED IN GAMMAS.

FIG. 4.5 : TOTAL MAGNETIC FIELD INTENSITY OF THE STUDY AREA CONTOURED IN GAMMAS.

Across the Undifferentiated Precambraian Basement Complex which occurs towards the Eastern direction of the study area, Total Magnetic Intensity values are in the middle with ranges between 7895.6 – 7642.5gammas, and are colored from brown to light yellow and greenish colors.

Across the Turonian Ezeaku Shale Group, high TMI values with ranges between 7937.2 - 7907.2gammas are noted towards its western direction (colored in light red), while intermediate TMI values between 7907.2 – 7854.8gammas are noted towards its eastern direction (colored in light brown).

Low Total Magnetic Intensity Values are noted towards the SE part of the TMI map and cuts across 4 geologic formations, belonging to the Precambraian Basement Complex, Turomian Ezeaku Shale Group, Nkporo Shale/Afikpo Sst, Imo Shale/Ebenebe Sst, and the Bende-Ameki Group.

High TMI values is generally observed towards the upper half of the Total Magnetic Intensity map of the study area with values between 7875.4 – 7951.5gammas.

4.1.2 Relief of the Study Area

The relief of the study area was summarized on two maps, namely; shaded relief map on Fig. 4.6, and 3-D Surface map on Fig. 4.7 of the Total Magnetic Field Intensity of the study area contoured in gammas.

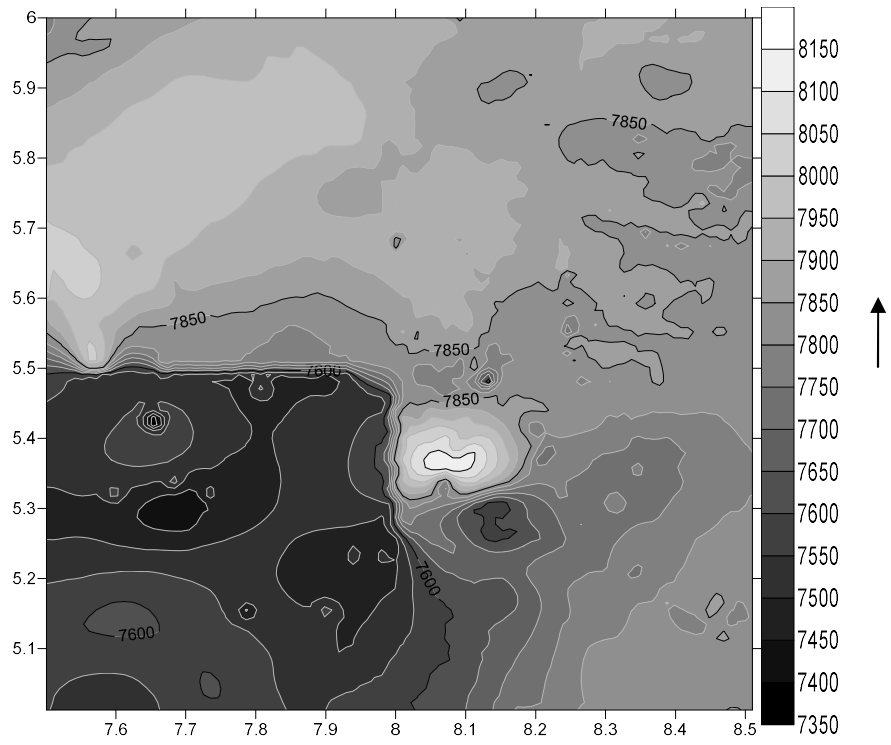


FIG. 4.6: SHADED RELIEF MAP OF THE TOTAL MAGNETIC FIELD INTENSITY OF THE STUDY AREA CONTOURED IN GAMMAS

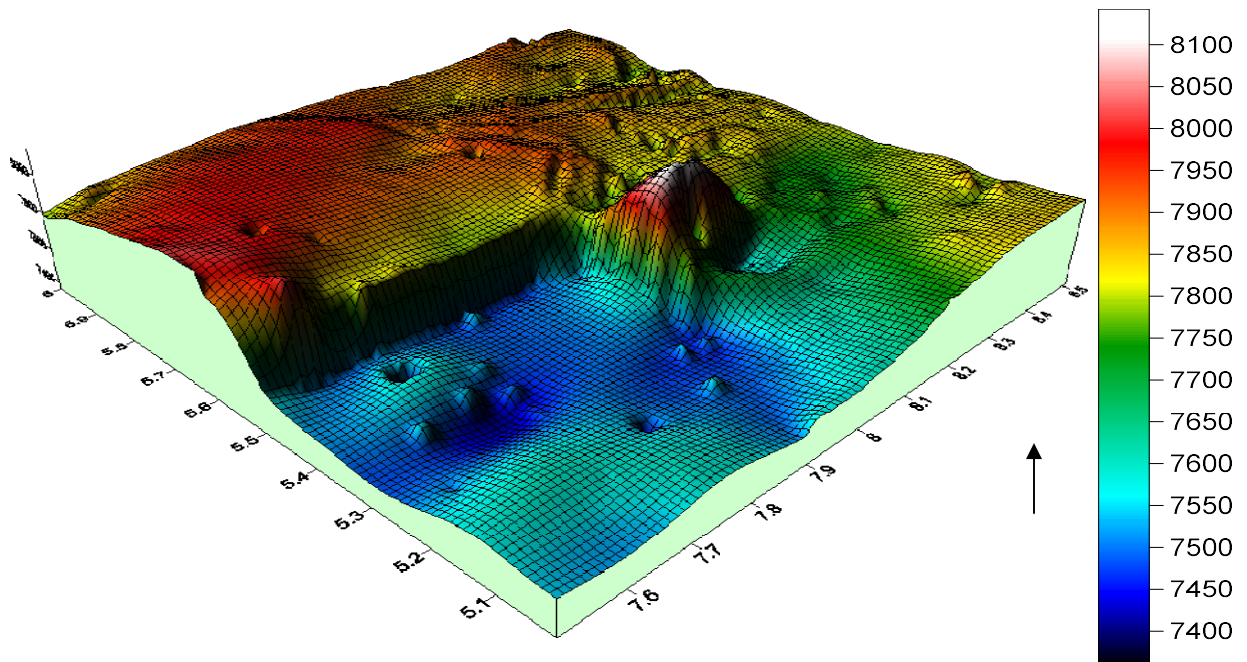


FIG. 4.7: 3-D SURFACE MAP OF THE STUDY AREA

Relief is basically the difference in elevation between any two points. Also, local relief is the difference between adjacent points (e.g., a hill and a valley), whereas total relief is the difference between the highest and lowest points on the map

From a qualitative interpretation of the derived relief maps, there is relatively very low elevation ranging from about 7450 – 7550 (colored in blue). Areas with this elevation include Uyo, Ikot Ekpene, Adiasim, Itu, Odoro Ekpe, and part of Arochukwu. This low elevation can be attributed to the presence of underlying Coastal Plain Sands.

Conversely, there is the presence of an outstanding high relief at an almost central position on the map, between Arochukwu and Ohafia, with value ranges of 8050 – 8100. This high ground is synonymous to two underlying formations, namely, Mamu formation and Nkporo Shale.

Other areas of high elevation on the relief maps occur NW of the map and cuts across 6 geological formations in areas like Afikpo, Owutu, Abriba, Ohafia, Bende, Uzuakoli. Relief values range here between 7850 – 8050. The underlying formations are of the Bende-Ameki Group, Imo Shale/Ebenebe Sandstone, Nsukka Formation, Ajali Sandstone, Mamu Formation, Nkporo Shale, and the Turonian Eze-Aku Shale Group.

Across the undifferentiated Precambrian Basement Complex, a middle-to-low relief was observed from the relief maps, with values ranging from 7650 – 7800. This area is to the East of the derived relief maps.

4.1.3 Upward Continuation

Map merging was accomplished subsequently by performing upwards continuation on the four High Resolution Aeromagnetic data sheets to a height of 200m, below the flight height, to obtain the same height level in all the sheets used in this study.

Basically, Upward and downward continuation will most commonly be used when merging together datasets from different sources, where the height of acquisition varies from one dataset to another. Aeromagnetic surveys frequently fall into this category inhomogeneity in topography.

However, Upward Continuation is considered a clean filter because it produces almost no side effects that may require the application of other filters or processes to correct. Because of this, it is often used to remove or minimize the effects of shallow sources and noise in grids. Also, upward continued data may be interpreted numerically and with modeling programs. This is not the case for many other filter processes. The result of applying this continuation is as shown in Fig. 4.8.

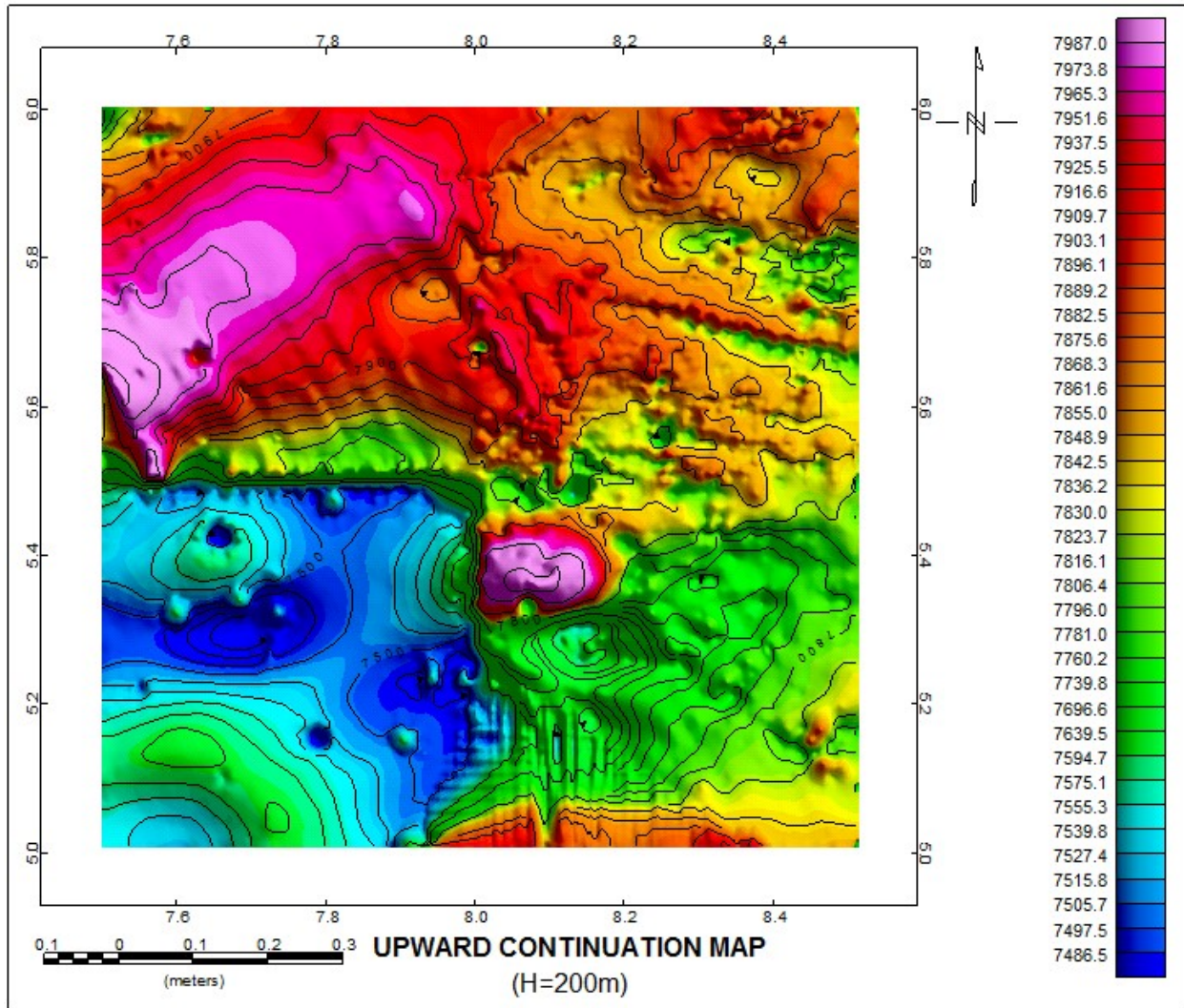
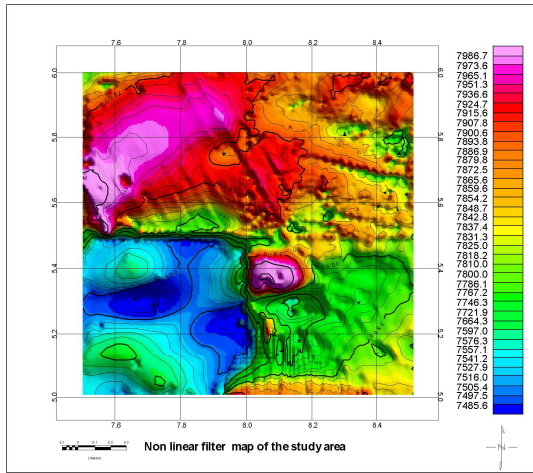


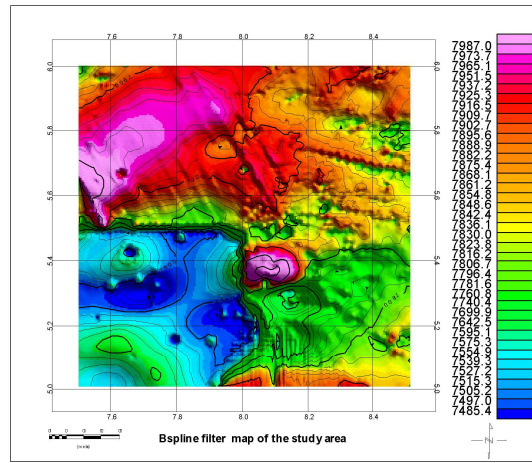
FIG. 4.8: UPWARD CONTINUATION MAP OF THE STUDY AREA.

4.1.4 Applied Filters

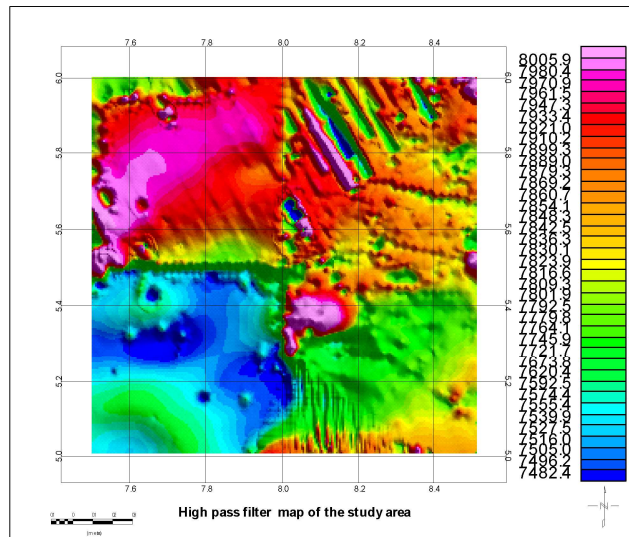
A number of filters were applied to the aeromagnetic data to cancel out certain wavelengths and pass certain other wavelengths. In essence, this serves to subdue the effects of certain underlying features, which may be regarded as noise, and enhance the effect of the desired underlying features. These class of filters applied to the data include Non-Linear, B-Spline, and High Pass filters, as shown in Figures 4.9, 4.10, and 4.11.:



4.9



4.10



4.11

FIG. 4.9: NON-LINEAR FILTER MAP OF THE STUDY AREA.
 FIG. 4.10: B-SPLINE FILTER MAP OF THE STUDY AREA
 FIG. 4.11: HIGH PASS FILTER MAP OF THE STUDY AREA

4.1.4.1 Non-Linear Filter

A non-linear filter was applied to the data to remove high amplitude and short wavelength noise, and was then followed by a linear low-pass filter to smooth any low-amplitude noise that remained.

Basically, NLFILT is ideal for removing very short wavelength, but high amplitude features from data. It is often thought of as a noise spike-rejection filter, but it can also be effective for removing short wavelength geological features, such as signal from surficial features. The decision algorithm is based on the width of features in the data and the amplitude of those features relative to a local background. In order to be considered noise, a feature must be narrower than a specified width and of greater amplitude than a specified amplitude tolerance. The width must be specified in number of data points. For example, single spikes in the data will have a width of 3 points. The non-linear filter amplitude tolerance, if specified, uses the actual data units, for example, 5 gammas. If no tolerance value is specified, the default value is set to equal a percentage of the range of data in the grid or XYZ file.

The result of removing short wavelength and high amplitude noise from the data showed the Total Magnetic Intensity of the study area varying from 7986.7 gammas– 7485.6gammas, as opposed to the range of the initial TMI value of 7980.0 gammas – 7485.4gammas.

4.1.4.2 B-Spline Filter and High-Pass Filter

A B-Spline filter allows a control of the smoothness of the spline and the tension applied to the ends of the spline.

On the other hand, a high pass filter was applied to the data to allow high wavenumbers (high frequencies) to pass to an output channel, thereby creating a High-Pass filter map of the study area.

Basically, a high-pass filter sharpens the input data by the application of a convolution filter. Features in the data that are longer than the long wavelength cutoff will be removed. The convolution filter is designed using the method of Fraser, 1966. The default length will be as

long as the cutoff wavelength, which produces a filter that exhibits a minimum of side effects, such as Gibb's phenomena.

4.1.5 Reduction to Pole

RTP was applied across the study area as a correction factor to remove the non-vertical magnetic component (the earth's magnetic field) and leave only the vertical component (causative body) in its correct spatial position. The RTP filtering process removes the effect of the earth's magnetic field by way of a gross shift of the observed magnetic readings. It also helps to better define boundaries between different basement lithologies with different magnetic susceptibilities. Fig. 4.12 shows the total magnetic intensity reduced to pole across the study area. Magnetic response is measured in gammas and the range of values is from 7453.6 gammas to a high of 8009.6 gammas.

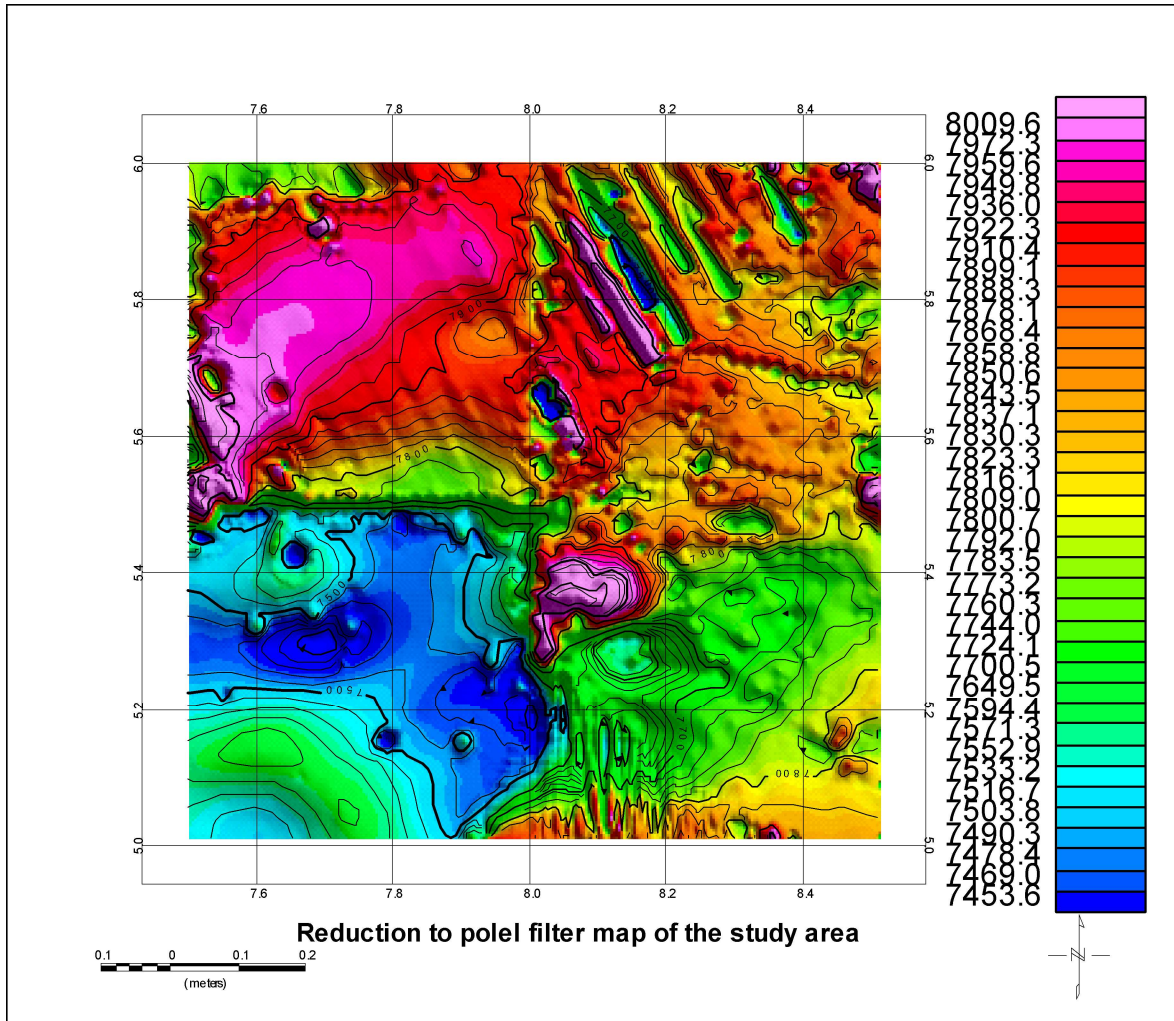


FIG. 4.12: REDUCTION TO POLE FILTER MAP OF THE STUDY AREA.

The purpose of the Reduction-to-Pole (RTP) operation is to provide an additional magnetic data set which, (assuming the frequently correct situation of sub vertical interfaces) depicts the magnetic field in a simplified form transformed to its equivalent response at the geomagnetic pole. The operation requires knowledge of the values of inclination and declination of the Earth's magnetic field appropriate to the survey. This is obtained by inputting the location and period during which the data were acquired. The height above sea level is also required.

4.1.6 Horizontal Gradient Map

For magnetic data the Total Gradient is the absolute value of a complex quantity known as the Analytic Signal and maxima also are indicators of body edges, independent of the Earth's magnetic field and direction of magnetization in bodies.

With the RTP correction, a magnetic body is spatially associated with its attendant magnetic response. As the magnetic response across this body changes, the maximum change or gradient of the magnetic slope occurs at or near the body edge. The horizontal gradient map depicts these changes in slope and in presentation; the net result is that horizontal gradient maxima and minima appear as ridges and valleys respectively. Therefore, a horizontal gradient map is useful in defining the contacts between basement lithologies and these contacts may represent individual basement blocks, faults and fault boundaries and other linear features.

The horizontal gradient map is as shown in Fig. 4.13.

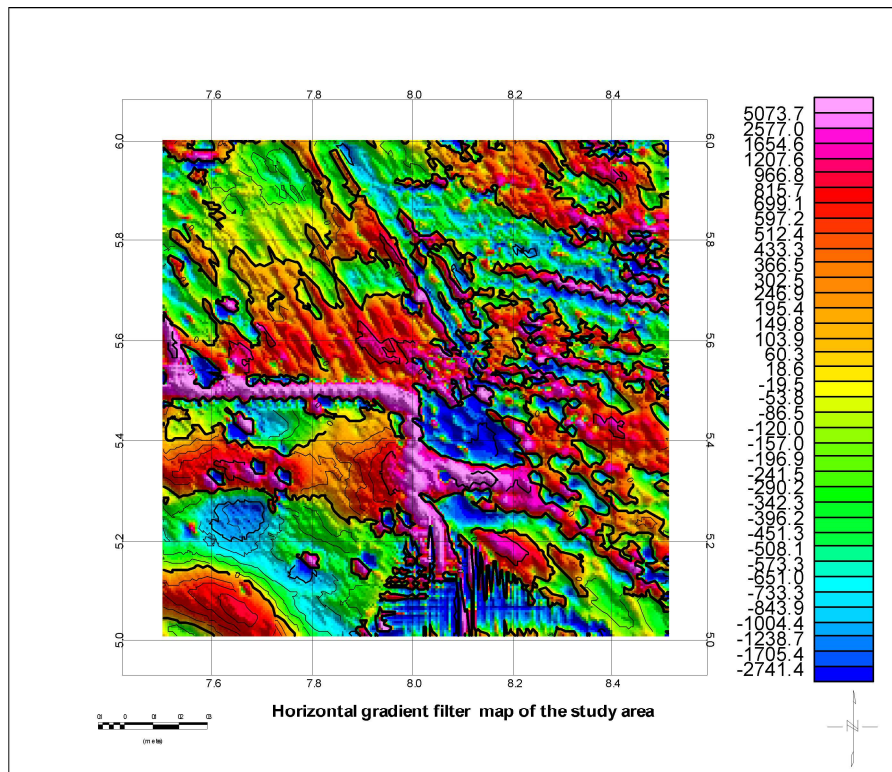


FIG. 4.13: HORIZONTAL GRADIENT MAP OF THE STUDY AREA.

The horizontal gradient field of the study area was thus derived. From qualitative interpretation, horizontal gradient maxima and minima in the form of hills and valleys are widespread all through the map.

The values of the horizontal gradient field of the study area ranges from +5073.7 gammas to -2741.4 gammas. There are ridges of high horizontal gradient maxima at the middle western part of the map cutting across six geological formations inbetween Bemde, Odoro-Ekpe, and Arpchkwu. This feature also runs down the central southern part of the said map. The same ridge of high horizontal gradient maxima also occurs towards the northern part of the undifferentiated basement complex, and its other occurrences are widespread. These areas are colored in purple and have values from 2577.0 gammas – 5073.7 gammas.

A NW-SE trending succession of hills and valleys occurs in the NW part of the map, with values ranging from -508.1 gammas – 966.8 gammas. These areas are depicted in colors of green, brown and red.

Low values of horizontal gradient depicted in blue, are widespread through the map, but are more pronounced towards the southern part of the said map (from -651.0 gammas to -2741.4 gammas).

Conclusively here, the thick black lines bounding the ridges and valleys can be said to be the indicators of body edges, independent of the Earth's magnetic field and direction of magnetisation in bodies.

4.1.7 Regional to Residual Anomaly Separation

A magnetic anomaly grid can be thought of as being composed of several components. Large scale structural elements which cause very long wavelength anomalies and referred to as the 'regional'. Superimposed on these are smaller localised perturbations, the 'residual', caused by smaller scale structures or bodies. The distinction between the regional and residual is somewhat arbitrary but the regional component can be thought of as the response of bodies large and/or deep compared with respect to the study area and, therefore, not readily interpretable within the

bounds of the study area. As stated above, an initial selection of the cut-off wavelength may be made on the basis of spectral analysis. Additional trials shall, in any case, be made to determine the most appropriate value to use on any dataset.

The regional gradients of the aeromagnetic data were removed by fitting a plane surface to the data by using multi-regression least squares analysis. The expression obtained for the regional field $T(R)$ is given as:

$$T(R) = 76122.158 + 0.371x + 0.248y \quad (16)$$

Where x and y are units of spacing. The regional field values are subtracted from the observed data to obtain the residual anomaly values. The technique is carried out on the aeromagnetic data of the study area to produce the first to fourth residual and regional trend surfaces.

The derived results from the first degree regional/residual field to the fourth degree regional/residual field, are as shown from Figures 4.17 to Figures 4.25.

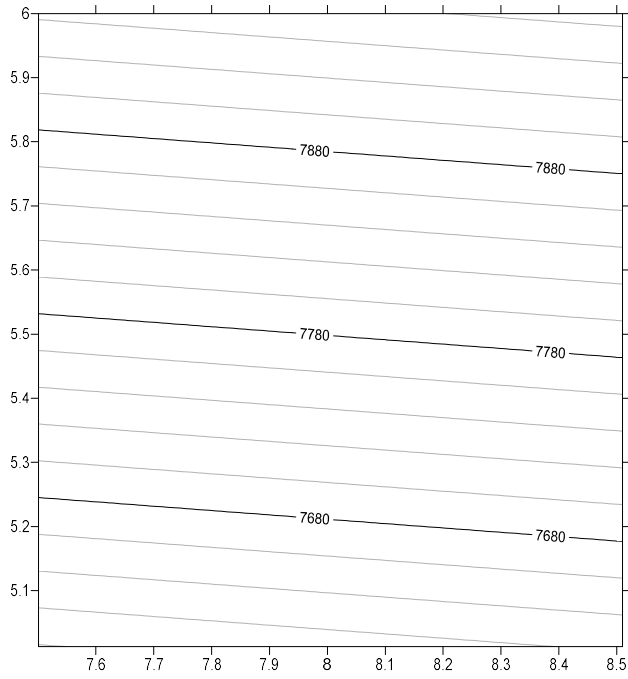


FIG. 4.14: FIRST DEGREE REGIONAL FIELD.

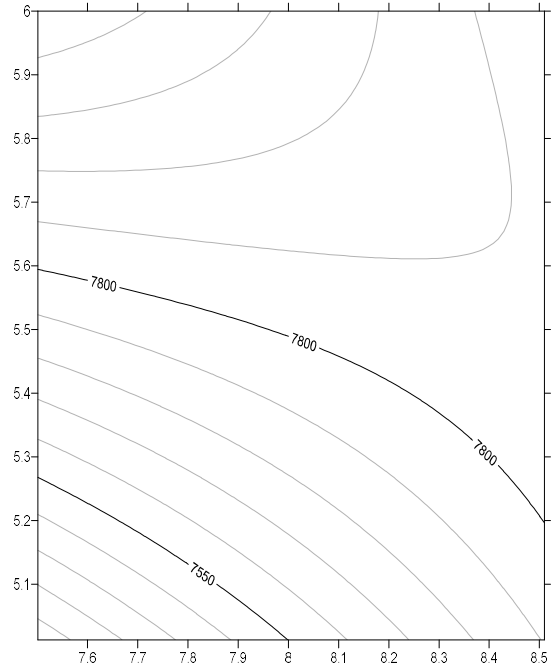


FIG. 4.15: SECOND DEGREE REGIONAL FIELD

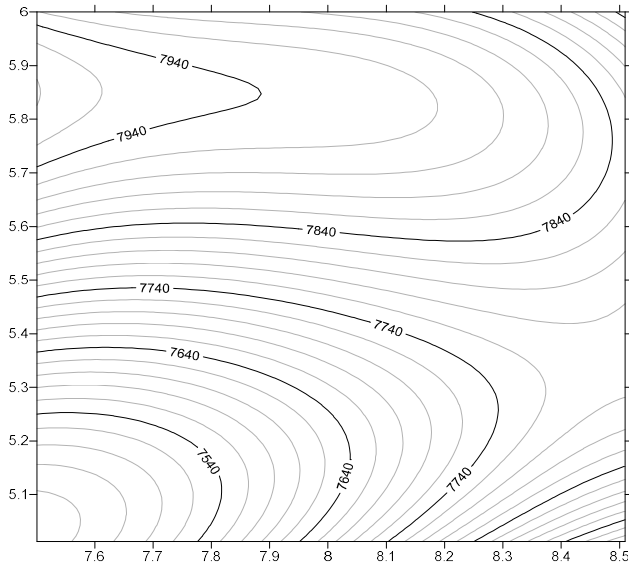


FIG. 4.16: THIRD DEGREE REGIONAL FIELD

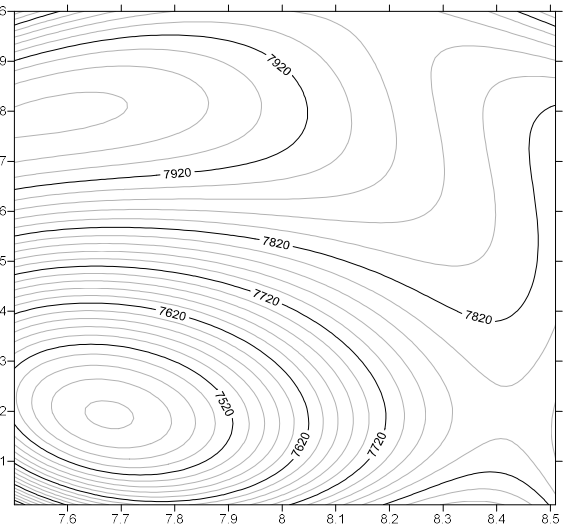


FIG. 4.17: FOURTH DEGREE REGIONAL FIELD

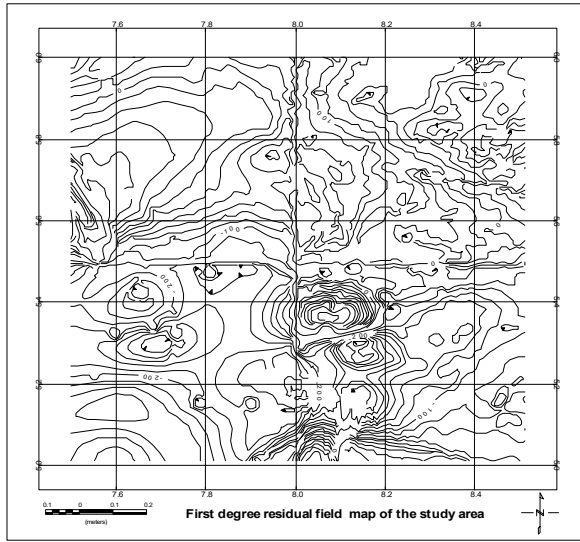


FIG. 4.18: FIRST DEGREE RESIDUAL FIELD

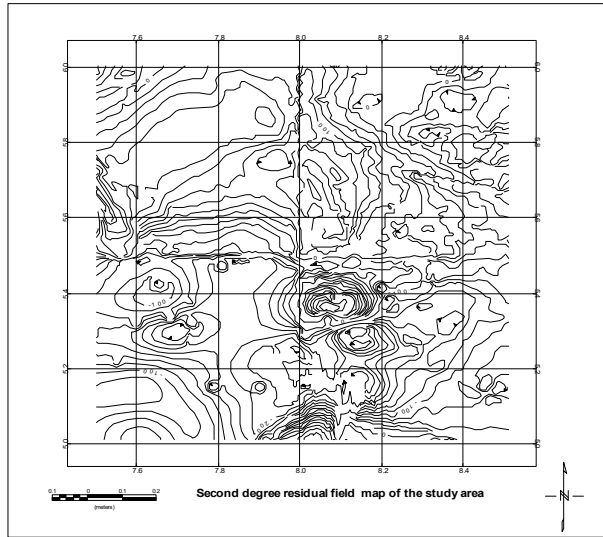


FIG. 4.19: SECOND DEGREE RESIDUAL FIELD

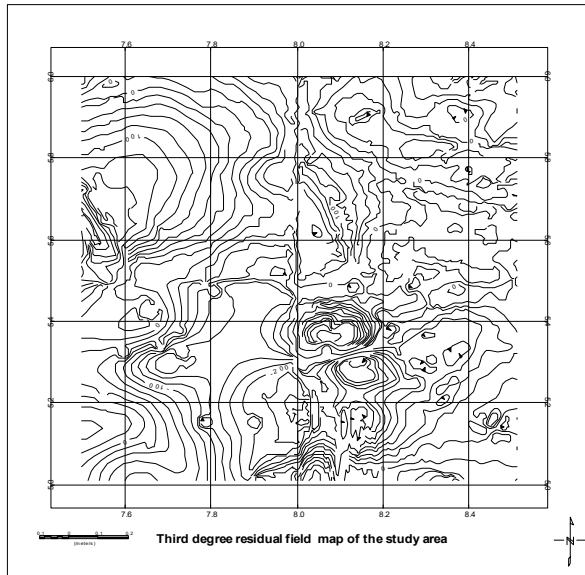


FIG. 4.20: THIRD DEGREE RESIDUAL FIELD

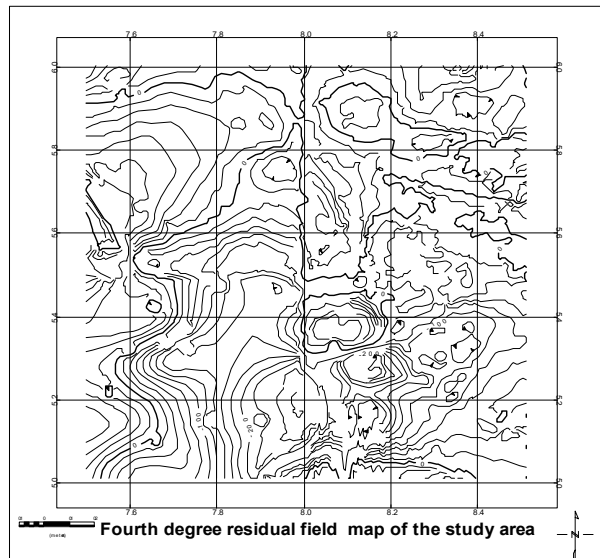


FIG. 4.21 FOURTH DEGREE RESIDUAL FIELD

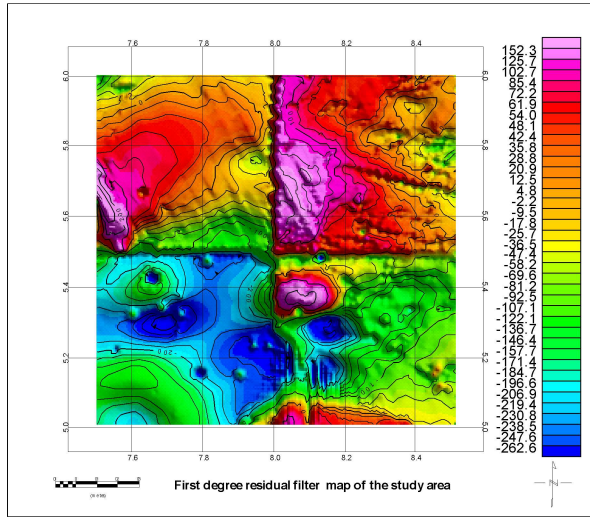


FIG. 4.22: FIRST DEGREE RESIDUAL FILTER MAP.

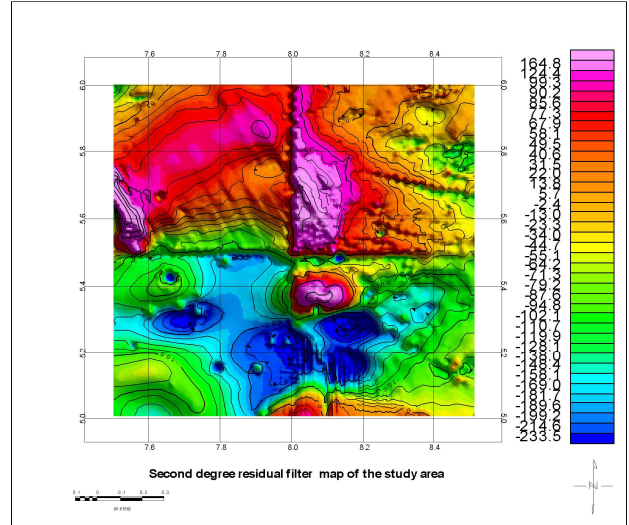


FIG. 4.23: SECOND DEGREE RESIDUAL FILTER MAP

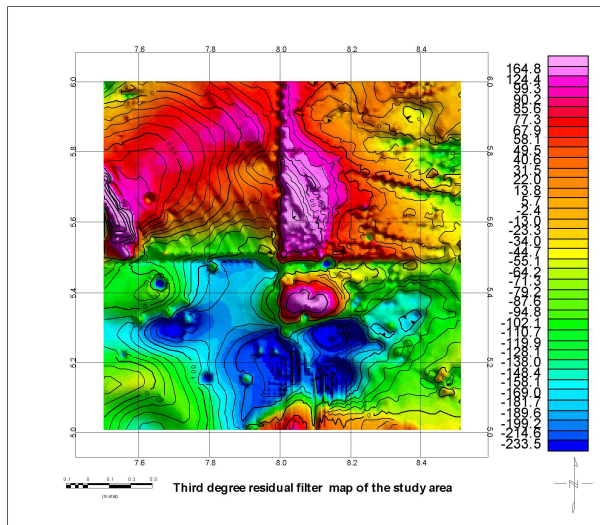


FIG. 4.24: THIRD DEGREE RESIDUAL FILTER MAP

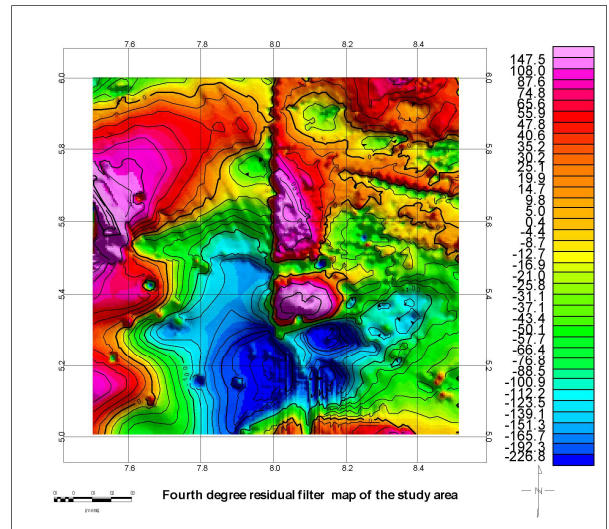


FIG. 4.25: FOURTH DEGREE RESIDUAL FILTER MAP

For this study, anomaly separation was done by application of surface fitting using polynomial regression method from first to fourth order. The Residual fields so obtained is basically the differences between the total field map and the regionals. As higher orders were calculated, the fit between the total field map and the regional field became closer and the residuals became smaller.

From first to third degree on the residual filter map of the study area, very low residual magnetic intensity occur towards the southern part of the map, depicted in blue and green colors. More specifically however, very low residual magnetic intensity between -262.6 gammas to -196.6 gammas are noted around Ikot-Ekpene, Adiasim, Itu, and Odoro-Ekpe areas of Uyo and Abia States. These areas coincide with the underlying Coastal Plain sands, Bende-Ameki Group, and Imo Shale/Ebenebe Sandstone, and therefore classified as areas with magnetic low.

Another phase of magnetic lows depicted in green colors on the said maps occurs also towards the southern part of the Residual filter maps but are more pronounced to its eastern half, with occasional occurrences of lower magnetic low craters. Values within these areas range from -171.4 gammas to -47-4 gammas, and coincide with the underlying geological formations of the Coastal Plain Sands, Imo Shale, Nkporo Shale/ Afikpo Sst., and the Undifferentiated Precambrian Basement Complex.

These areas of low residual magnetic intensities can be qualitatively interpreted as zones of low magnetization, which implies to the non-existence of underlying shallow to near surface magnetized bodies.

Conversely, the northern half of the 1st to 3rd degree residual filter maps shows increasing residual magnetic intensities Uzuakoli, Owutu, Afikpo, Bende, Ariba, Ugep, and Ekor, all in Abia and Cross River States. These areas are underlain by the nine geological formations bordering the northern half of the Geological Map of the Study area.

The major magnetic highs in the study area are noted around Arochukwu, Afikpo, Ariba, Ohafia, and coincides with the underlying Mamu Formation, Nkporo Shake/Afikpo Sst, Bende-Ameki Group (towards the western part of the map), and Alluvium (towards the southern end of

the map). These areas are depicted with purple coloration and have residual magnetic intensity values between +102.7gammas to +152.3gammas.

These areas of high residual magnetic intensities can therefore be qualitatively interpreted as zones of high magnetization, which implies to the existence of underlying shallow to near surface magnetized bodies.

4.1.8 Derivatives

The derivative of a function mathematically, represents an infinitesimal change in the function with respect to one of its variables. They could be taken with respect to time and thus denoted with Newton's overdo notation. The process of finding a derivative is called differentiation, and the horizontal and vertical derivatives have been obtained for the purpose of this work.

4.1.8.1 Horizontal Derivatives

The 1st and 2nd horizontal derivatives of the Residual Maps of the Total Magnetic Intensity of the study area was obtained, and this is basically calculated as the Pythagorean sum of the gradients in the orthogonal directions. Choosing the directions to be along one of the grids, the calculation becomes:

$$\sqrt{(G_x)^2 + (G_y)^2} = H_z.$$

The resultant horizontal derivative maps are as shown in Figures 4.26 and 4.27.

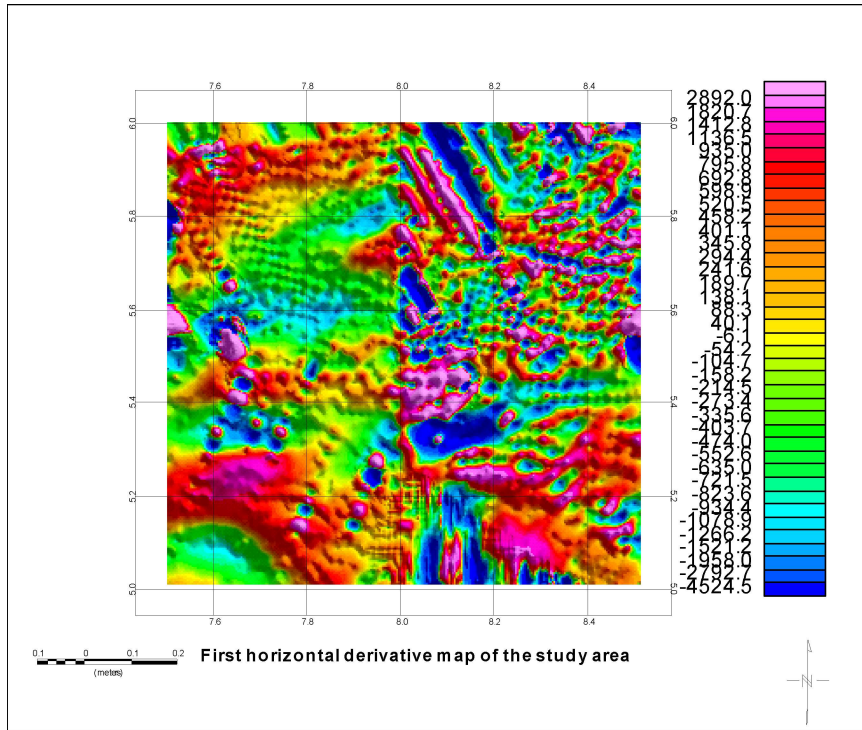


FIG. 4.26: FIRST HORIZONTAL DERIVATIVE MAP OF THE STUDY AREA.

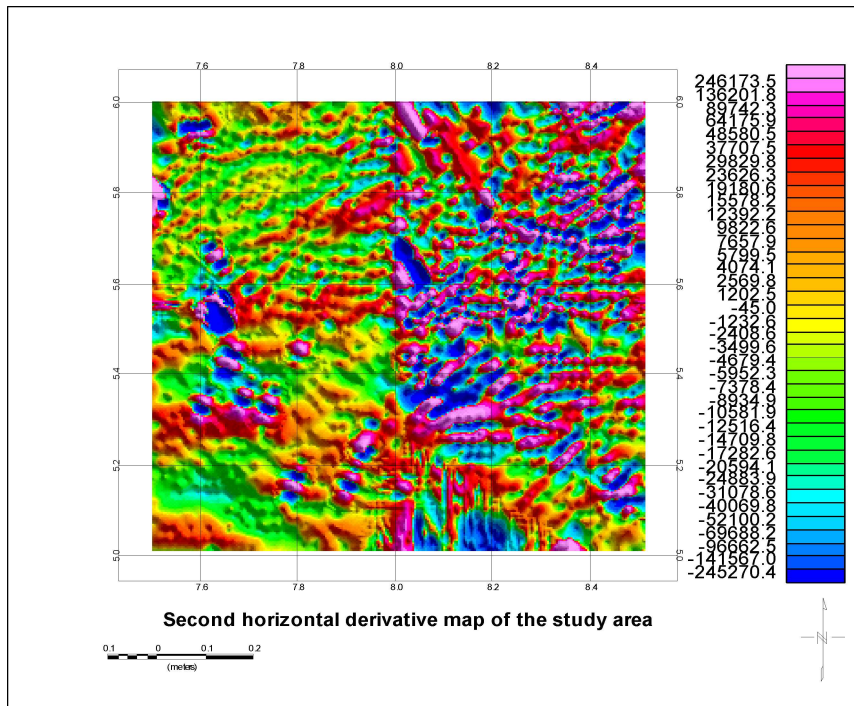


FIG. 4.27: SECOND HORIZONTAL DERIVATIVE MAP OF THE STUDY AREA.

4.1.8.2 Vertical Derivatives

Vertical derivatives are enhancement techniques which amplify shorter wavelength features relatively to those with longer wavelengths. Usually, the First Vertical Derivative (FVD) and second vertical Derivative (SVD) transforms are the only transforms of this type that are routinely generated because, the higher the order the greater is the relative amplification of higher frequencies and greater too is the risk of accentuating noise to an unacceptable degree. For the purpose of this work, the FVD and SVD were calculated, where the first vertical derivative can be used as an alternative to a residual display, and the SVD's ZERO CONTOUR represents the point of inflexion on the original anomaly curve which approximates the locations of edges of the causative bodies, provided that the bodies are shallow and have vertical sides. Recall that second vertical derivative (SVD) transform is a mathematical transform based on Laplace's equation. It has the effect of accentuating the shorter wavelength (shallower source) components at the expense of longer wavelength (generally deeper) features (Elkins, 1951).

The derived FVD and SVD maps are as shown in Figures 4.28 and 4.29.

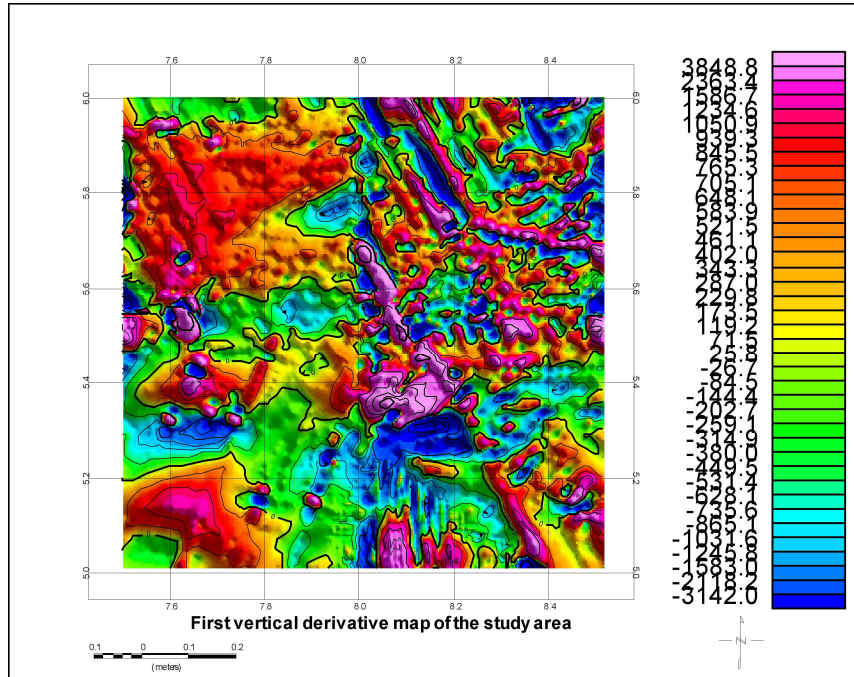


FIG. 4.28: FIRST VERTICAL DERIVATIVE MAP OF THE STUDY AREA.

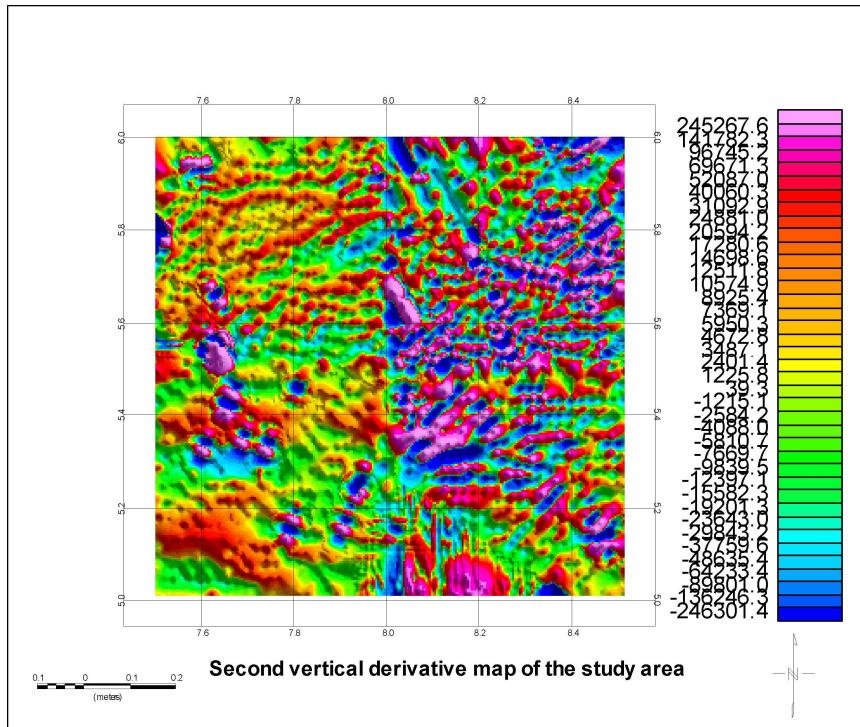


FIG. 4.29: SECOND VERTICAL DERIVATIVE MAP OF THE STUDY AREA.

4.1.9 Depth Estimation by Spectral Analysis

To estimate basement depth here, the digitized aeromagnetic data was transformed in Fourier domain to compute the energy (or amplitude) spectrum. This was then plotted on a logarithmic scale against frequency. It is the slopes of the segments so obtained that yield estimates of average depths to magnetic sources of anomalies.

Three methods for depth estimation were adopted for this study. They include;

- Peter's slope method
- Tiburg rule
- Half-width rule

The FORTRAN program used here is called SPECTRDEP, and to determine the depths of the anomalies to their magnetic sources, the study area was divided into 16 overlapping sections. A two layer (D1 and D2) depth model was adopted.

Additionally, the individual Total Field Aeromagnetic data of the four areas which make up the study area (Afikpo, Ugep, Ikot-Ekpene, Uwet) were contoured at 20nT intervals and the corresponding maps were derived. Linear magnetic anomalies of the four areas along chosen profiles were also interpreted.

The results are as shown in from Figures 4.30 to Figure 4.41, and Tables 4.1 to Table 4.4.

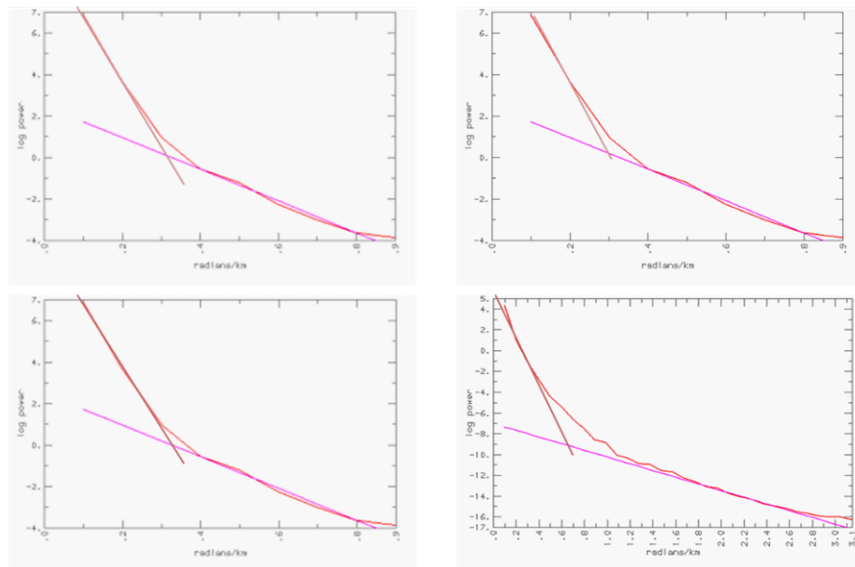


FIG. 4.30: PLOT OF LOG POWER AGAINST FREQUENCY (IKOT-EKPENE)

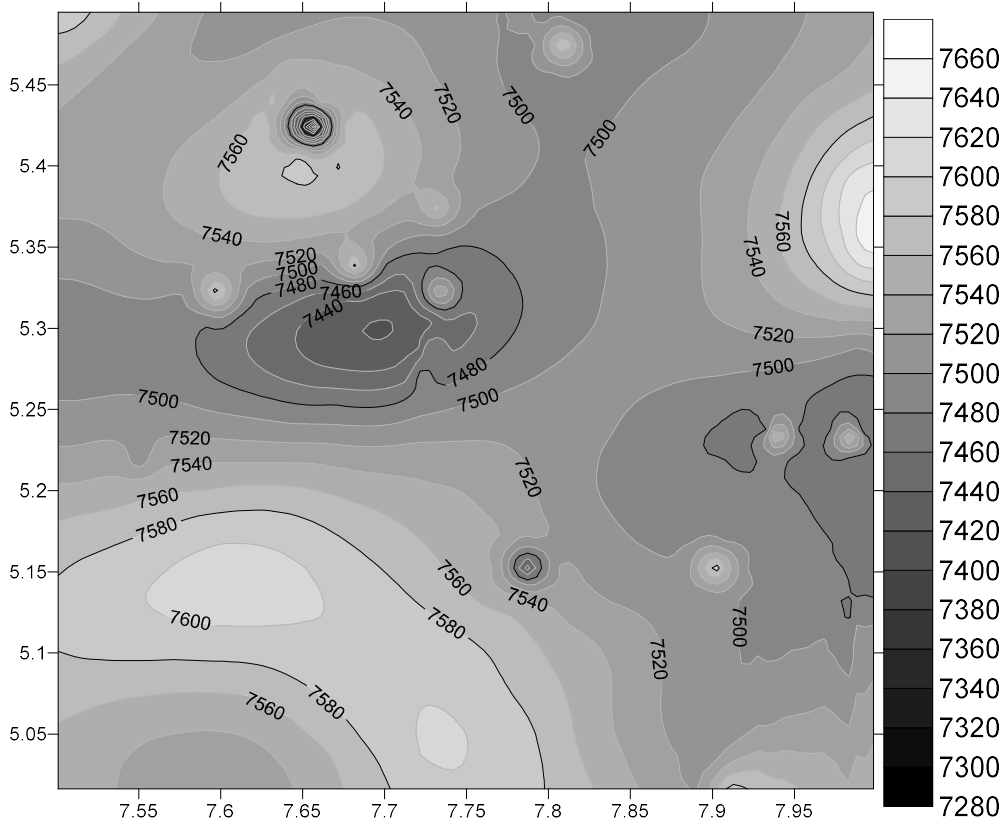


FIG. 4.31: TOTAL MAGNETIC INTENSITY FIELD MAP OF THE AEROMAGNETIC DATA OF THE IKOT-EKPENE

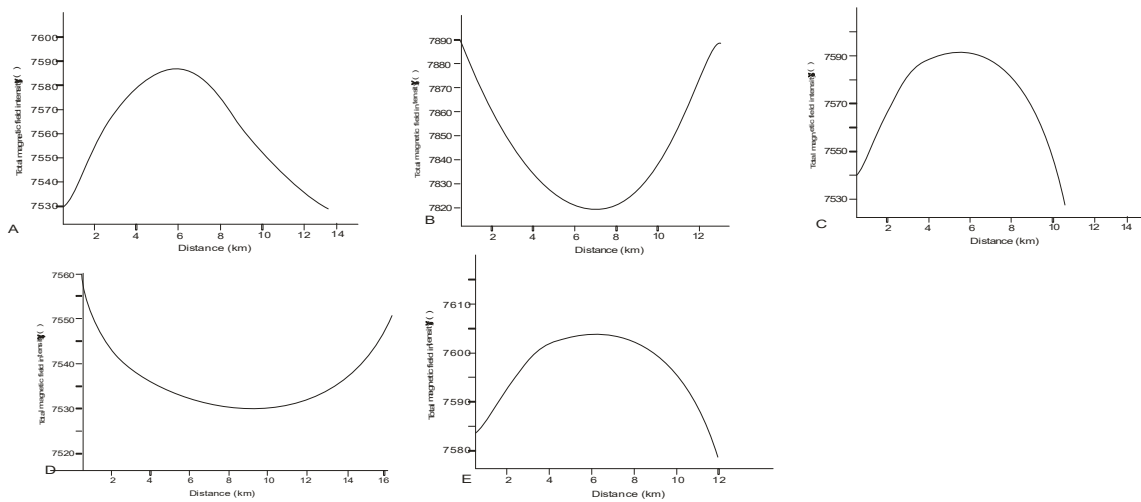


FIG. 4.32: INTERPRETATION OF SOME LINEAR MAGNETIC ANOMALIES FROM IKOT-EKPENE

TABLE 4.1: CALCULATED DEPTH TO THE MAGNETIC SOURCE AEROMAGNETIC
MAP OF IKOTEKPENE

TOWN	COORDINATE		DEPTH ESTIMATION IN KM			WIDTH (KM)	AMPLITUDE IN GAMMA	MAGNETIZAT ION (A/M)	1% RADIAN CE	TYPE OF ANOMALY
	LAT	LONG	PETER'S SLOPE	TIBURG	HALF WIDTH					
AFIKPO										
A	5.2545	8.4449	1.723	4.136	3.048	8.0	7850	0.23	-1.00	LOW
B	5.3601	8.4115	0.973	1.849	1.3348	10.5	7980	0.81	2.30	HIGH
C	5.4801	8.0712	0.235	0.518	0.348	12.0	7895	0.91	1.52	HIGH
D	5.3583	8.3528	1.848	4.136	3.048	8.0	7973	4.00	1.21	HIGH
E	5.2743	8.1579	3.09	6.548	4.948	10.5	7955	2.00	1.41	HIGH

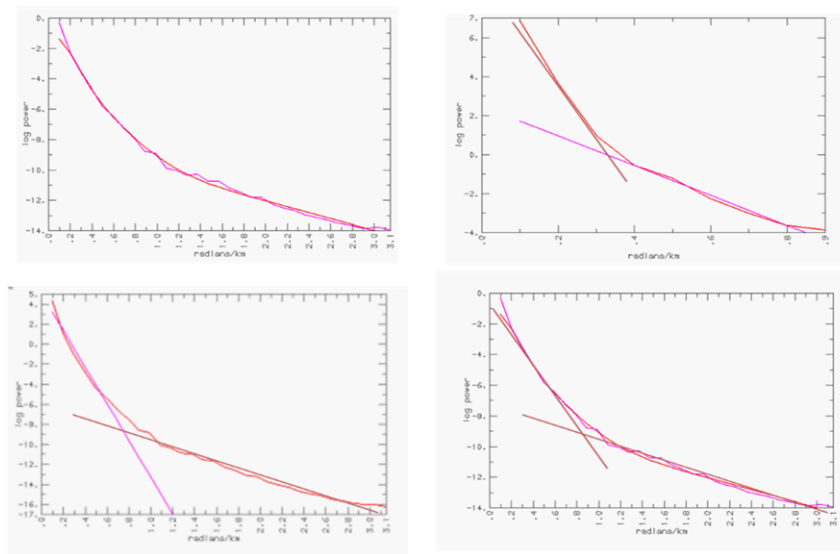


FIG. 4.33: PLOT OF LOG POWER AGAINST FREQUENCY (UWET)

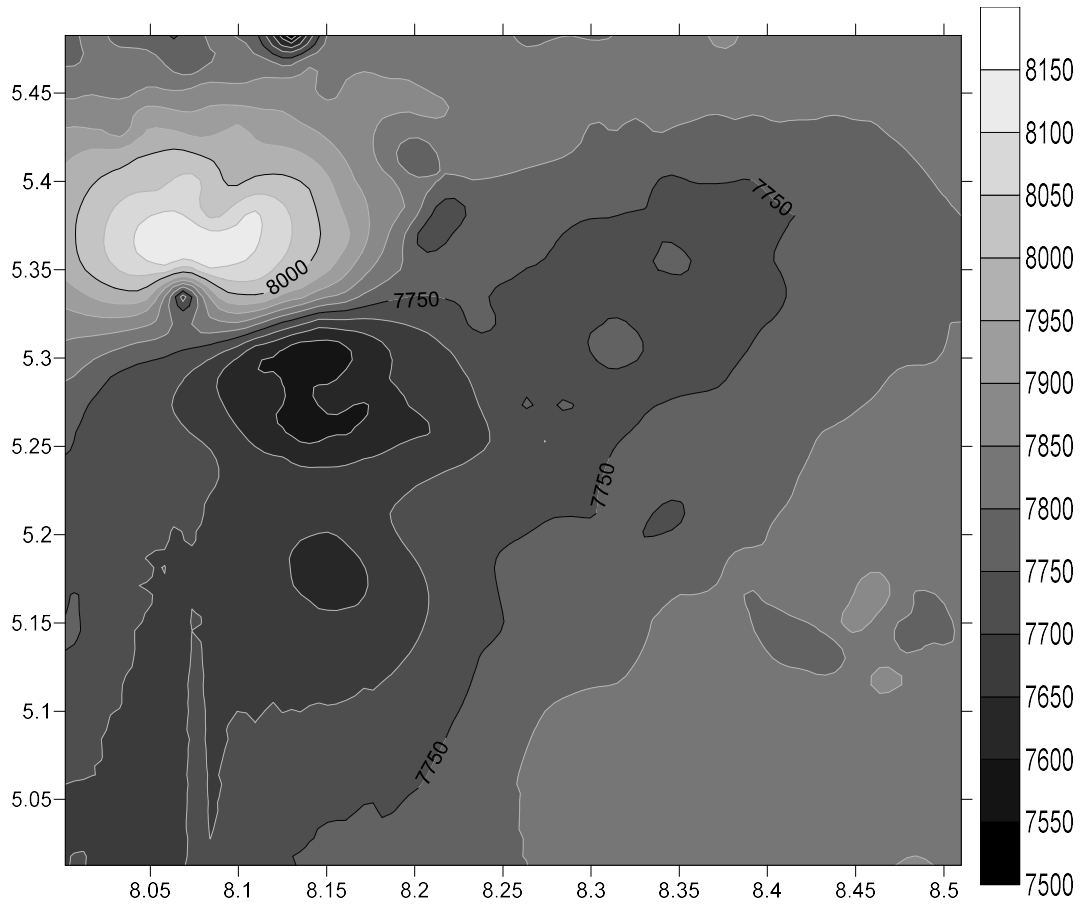


FIG. 4.34: TOTAL MAGNETIC INTENSITY FIELD MAP OF THE AEROMAGNETIC DATA OF THE UWET

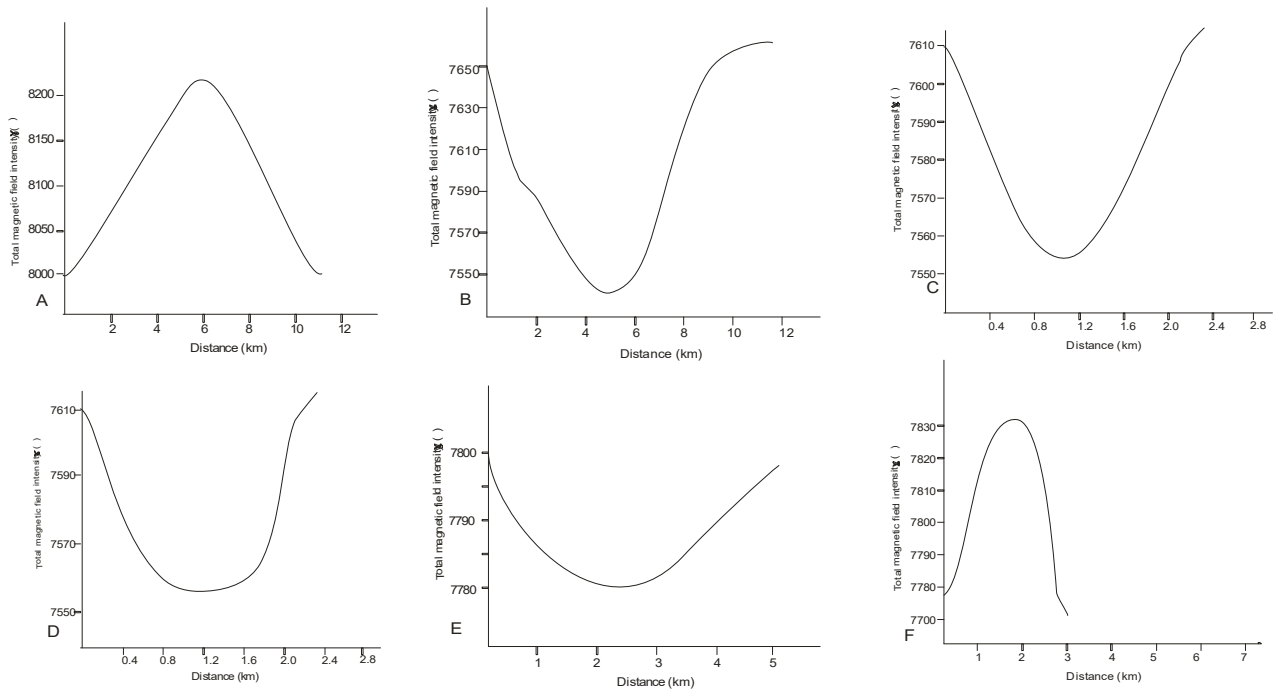


FIG. 4.35: INTERPRETATION OF SOME LINEAR MAGNETIC ANOMALIES FROM UWET

TABLE 4.2: CALCULATED DEPTH TO THE MAGNETIC SOURCE AEROMAGNETIC MAP OF UWET

TOWN	COORDINATE		DEPTH ESTIMATION IN KM			WIDTH (KM)	AMPLITUDE IN GAMMA	MAGNETIZATION (A/M)	1% RADIAN	ANOMALY TYPE
	LAT	LONG	PETER'S SLOPE	TIBURG	HALF WIDTH					
A	5.3610	8.0658	0.298	0.367	0.548	5.5	8126	4.05	1.49	HIGH
B	5.3005	8.1380	2.848	4.672	3.448	7.6	7749	1.75	1.44	LOW
C	5.2662	8.1407	0.5355	0.9327	0.667	7.8	7555	1.68	1.39	LOW
D	5.4909	8.1218	0.248	0.701	0.598	7.9	7550	0.91	1.40	LOW
E	5.1308	8.4205	1.09	1.848	1.348	5.0	7786	0.20	1.42	LOW
F	5.2238	8.3339	0.5355	0.987	0.698	3.5	7830	1.24	1.38	HIGH

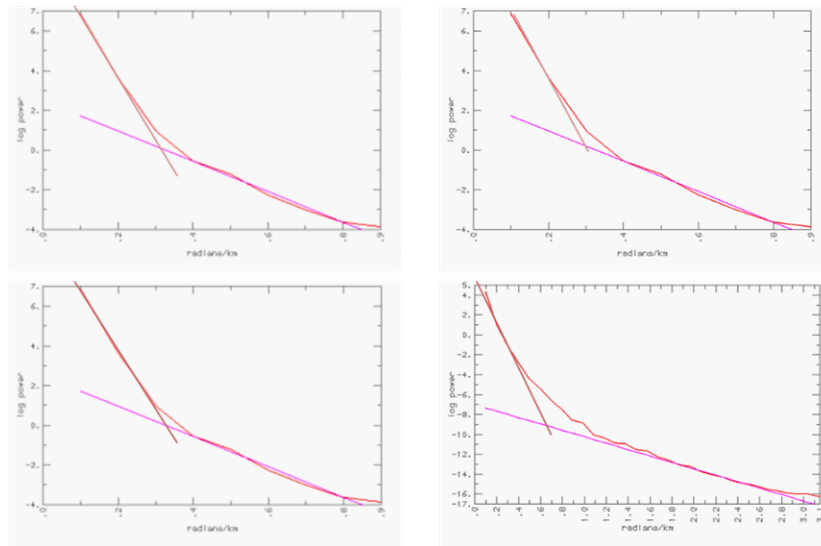


FIG. 4.36: PLOT OF LOG POWER AGAINST FREQUENCY (UGEP)

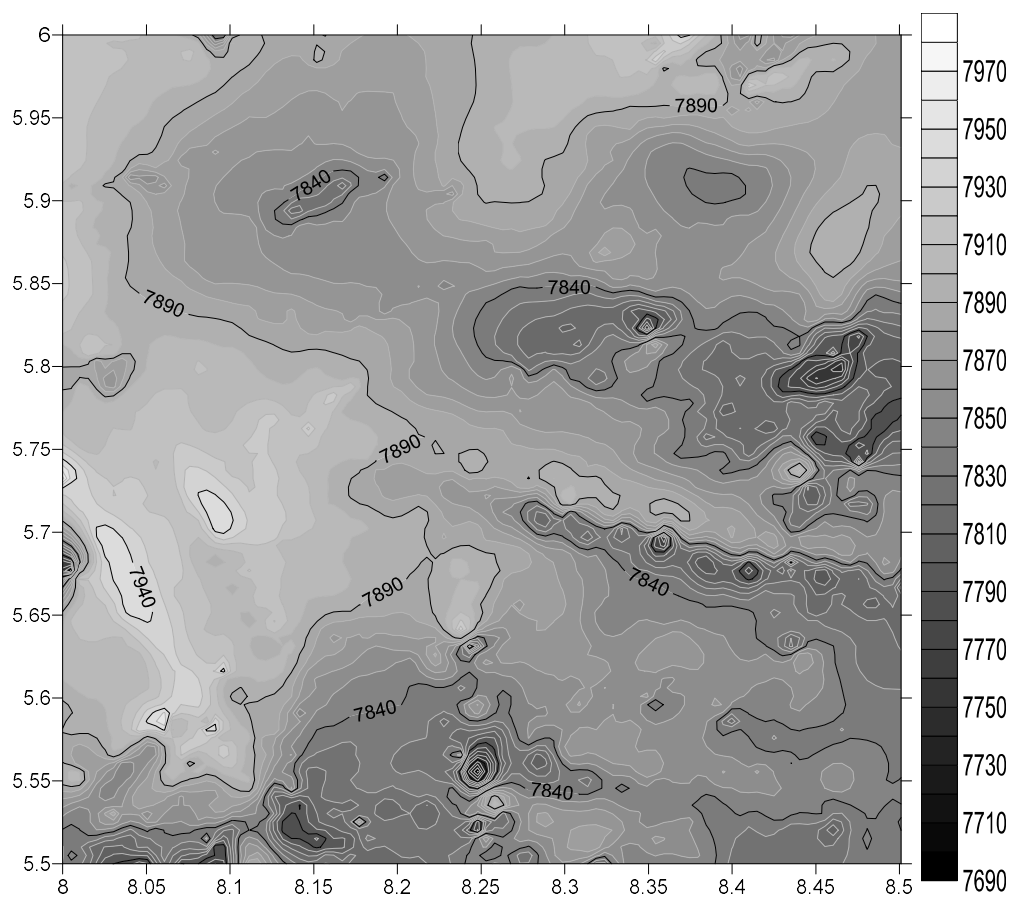


FIG. 4.37: TOTAL MAGNETIC INTENSITY FIELD MAP OF THE AEROMAGNETIC DATA OF THE UGEP

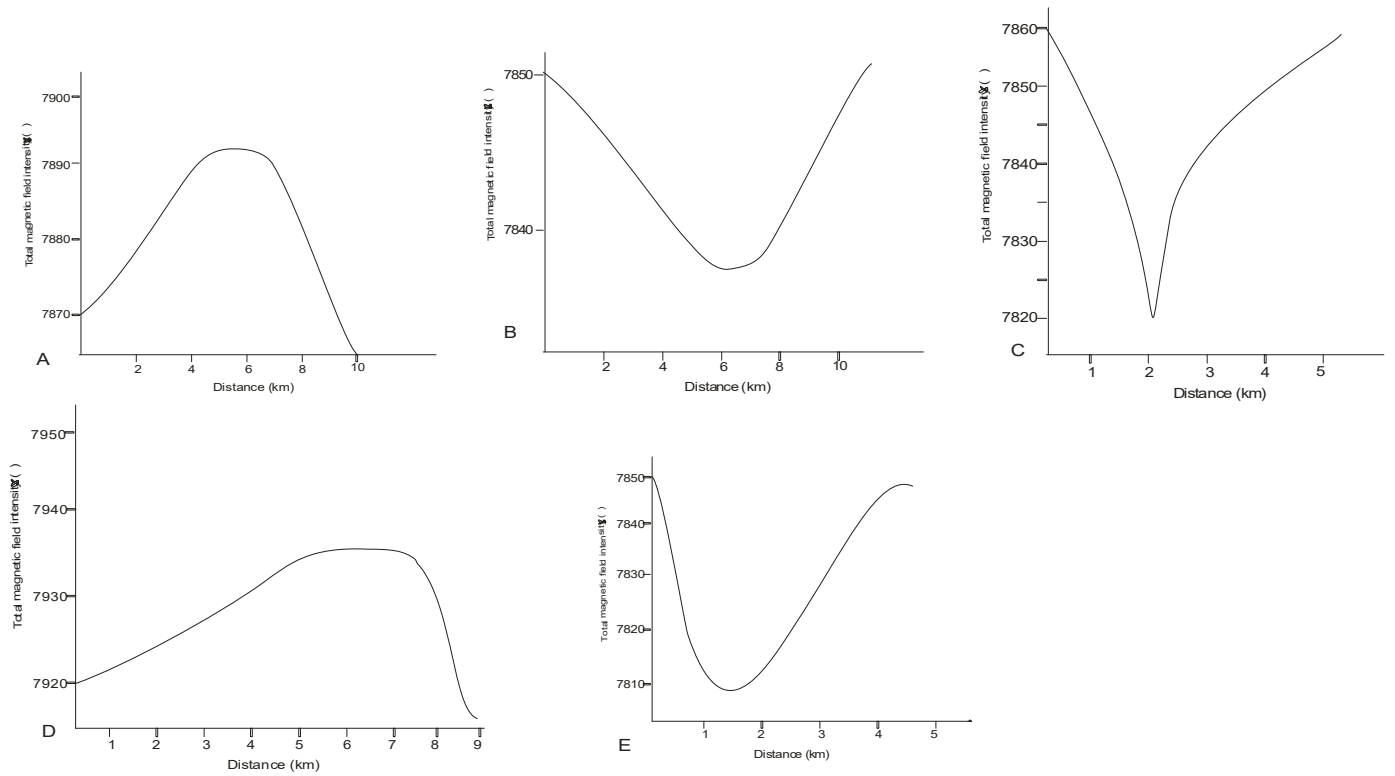


FIG. 4.38: INTERPRETATION OF SOME LINEAR MAGNETIC ANOMALIES FROM UGEP

TABLE 4.3: CALCULATED DEPTH TO THE MAGNETIC SOURCE AEROMAGNETIC MAP OF UGEP

TOWN	COORDINATE		DEPTH ESTIMATION IN KM			WIDTH (KM)	AMPLITUDE (GAMMA)	MAGNETIZATION (A/M)	1% RADIANCE	TYPE OF ANOMALY
	LAT	LONG	PETER'S SLOPE	TIBURG	HALF WIDTH					
A	5.6718	8.4629	0.0355	4.136	3.148	7.8	7909	1.53	1.24	HIGH
B	5.7088	8.3989	1.285	4.136	3.048	7.5	7838	0.48	1.09	LOW
C	5.7043	8.0161	1.035	0.585	0.398	5.5	7828	0.14	-1.50	LOW
D	5.4714	8.0442	0.6292	3.2985	2.448	12.0	7945	1.64	1.43	HIGH
E	5.3631	8.2842	1.535	1.791	1.348	6.0	7805	0.91	-1.57	LOW

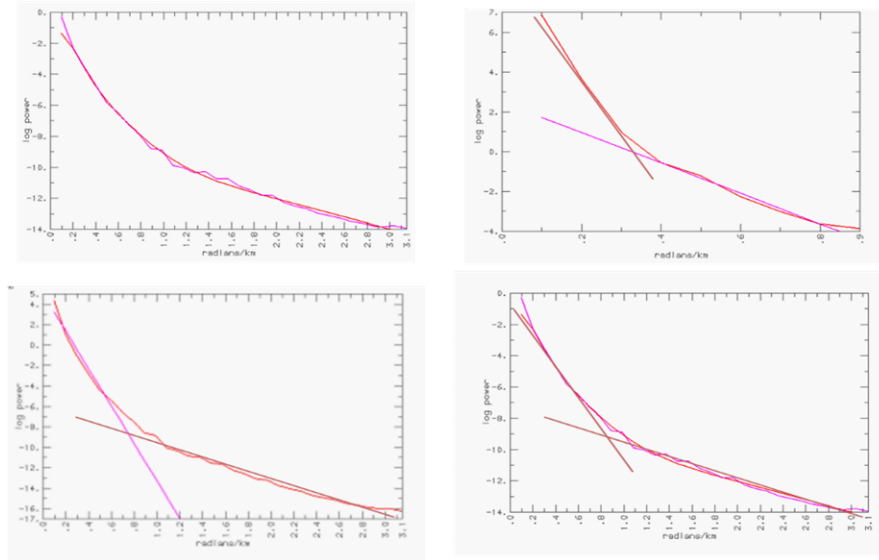


FIG. 4.39: PLOT OF LOG POWER AGAINST FREQUENCY (AFIKPO)

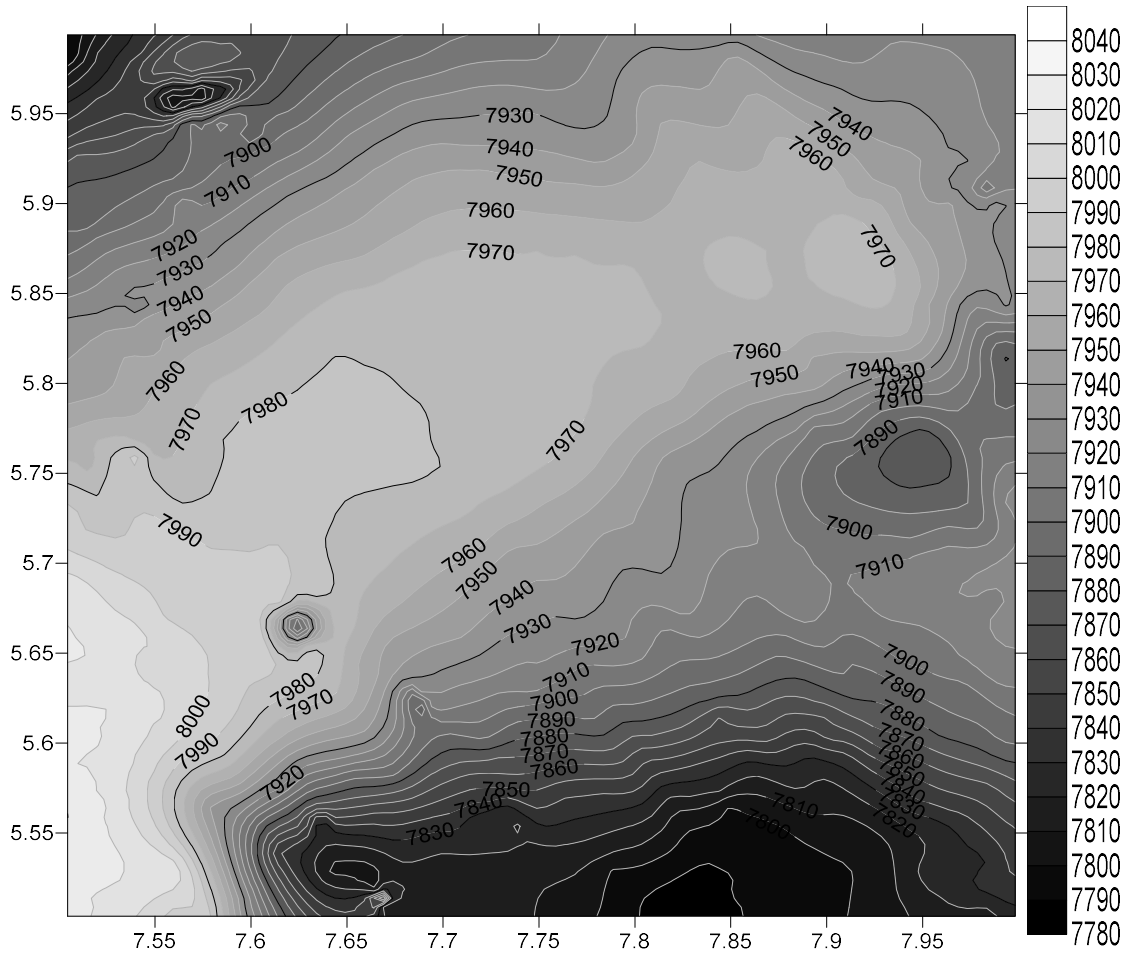


FIG. 4.40: TOTAL MAGNETIC INTENSITY FIELD MAP OF THE AEROMAGNETIC DATA OF THE AFIKPO

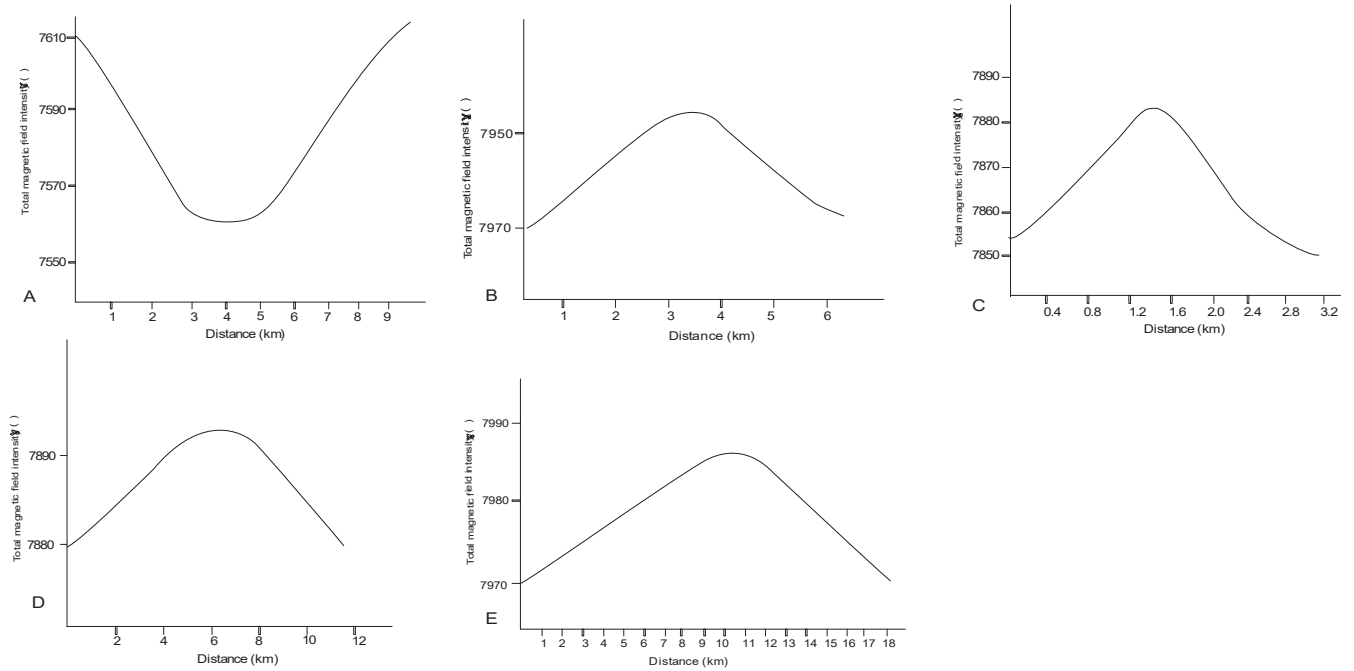


FIG. 4.41: INTERPRETATION OF SOME LINEAR MAGNETIC ANOMALIES FROM AFIKPO SHEET

TABLE 4.4: CALCULATED DEPTH TO THE MAGNETIC SOURCE AEROMAGNETIC MAP OF AFIKPO

TOWN	COORDINATE		DEPTH ESTIMATION IN KM			WIDTH (KM)	AMPLITUDE IN GAMMA	MAGNETIZAT ION (A/M)	1% RADIAN CE	TYPE OF ANOMALY
	LAT	LONG	PETER'S SLOPE	TIBURG	HALF WIDTH					
A	5.2545	8.4449	1.723	4.136	3.048	8.0	7850	0.23	-1.00	LOW
B	5.3601	8.4115	0.973	1.849	1.3348	10.5	7980	0.81	2.30	HIGH
C	5.4801	8.0712	0.235	0.518	0.348	12.0	7895	0.91	1.52	HIGH
D	5.3583	8.3528	1.848	4.136	3.048	8.0	7973	4.00	1.21	HIGH
E	5.2743	8.1579	3.09	6.548	4.948	10.5	7955	2.00	1.41	HIGH

The estimated depths to magnetic basement are shown as D1 and D2 in table 4.5, where D1 represents the depth to the shallower sources, and D2 as average depths to the basement complex (sedimentary thickness) in the blocks considered.

The first layer depth (D1), varies from 0.0345 km – 2.7798 km, with an average depth of 1.365425 km. The second layer depth (D2), varies from 0.7012 km – 6.7893 km, with an average depth of 3.403056 km. It is also summarized from each of the Spectral plots, that D1 values so obtained are the depth values to shallower sources of anomalies in the study area, while D2 values so obtained are the depth values to the Basement Complex, and therefore depicts the sedimentary thickness in the blocks considered, as shown below:

TABLE 4.5: BASEMENT DEPTH ESTIMATES OF THE STUDY AREA CALCULATED FROM SPECTRAL INVERSION

TOWN	X1	X2	Y1	Y2	ESTIMATED DEPTHS(KM)	
					D1	D2
AFIKPO	7.5	7.75	5.5	5.75	1.6763	3.2636
	7.5	7.75	5.75	6	0.8973	1.9859
	7.75	8	5.5	5.75	0.3535	0.9852
	7.75	8	5.75	6	1.648	3.2336
UGEP	8	8.25	5.5	5.75	0.0345	3.4326
	8	8.25	5.75	6	0.9885	3.3436
	8.25	8.5	5.5	5.75	1.0425	0.7785
	8.25	8.5	5.75	6	0.7629	2.3785
UWET	8	8.25	5	5.25	1.6598	3.7867
	8	8.25	5.25	5.5	2.7798	4.8967
	8.25	8.5	5	5.25	0.6535	2.9327
	8.25	8.5	5.25	5.5	0.3548	0.7012
IKOT EKPENE	7.5	7.75	5	5.25	2.4463	5.2340
	7.5	7.75	5.25	5.5	2.2113	5.7638
	7.75	8	5	5.25	1.7695	4.9430
	7.75	8	5.25	5.5	2.5683	6.7893

Contour maps of the depths to shallower sources of anomalies (D1), and depths to Basement (D2) , and their appearances on 3D wireframe was also derived and are as shown in Figures 4.42 to Figures 4.45.

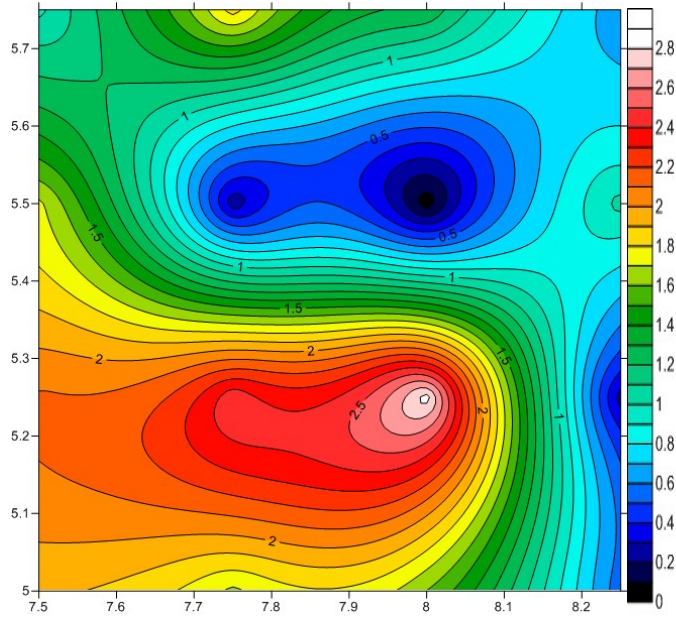


FIG. 4.42: DEPTH MAP, D1

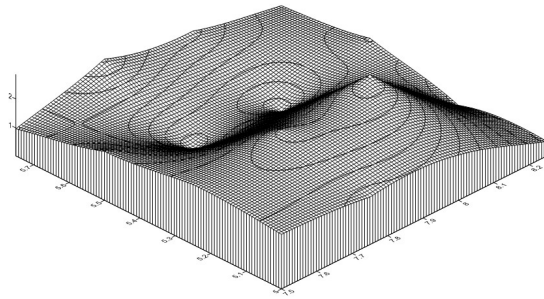


FIG. 4.43: 3D WIREFRAME DEPTH MAP, D1

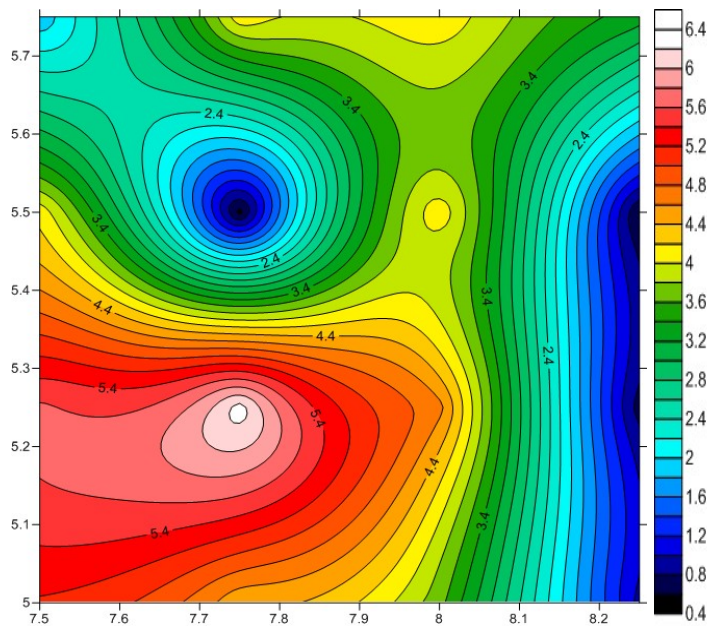


FIG. 4.44: DEPTH MAP, D2

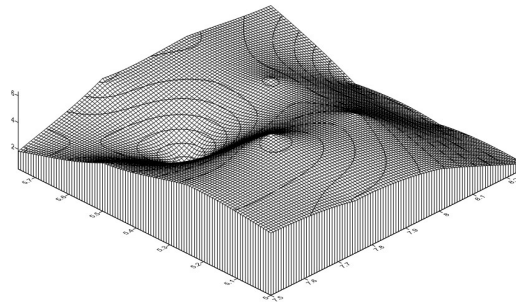


FIG. 4.45: 3D WIREFRAME DEPTH MAP, D2

Some linear magnetic anomalies across the entire study area, with respect to each Aeromagnetic data sheet was also interpreted here, along chosen profiles. They are interpreted as magnetic highs and magnetic lows, and the causes of these anomalies were defined by a 3D Euler Deconvolution of the digitized aeromagnetic data.

For Ikot-Ekpene, profiles A→ E were taken at Profile [A], as 29Km West of Arochukwu, Profiles [B], [C] and [D] as 13Km North; 12Km South-West and 23Km South-West of Ikot Ekpene respectively. The interpretation of magnetic anomalies here shows three (3) magnetic highs in profiles A, C, & E, and two (2) magnetic lows in profiles B & D.

For Uwet, profiles A→ F were taken at Profile [A] as 22Km North-West of Uwet, Profile [B] as 10Km North-West Uwet; Profile[C] as 10Km South of Uwet, [D] as 25Km South-East of Uwet, Profile [E] as 9Km East of Odukpani; and Profile [F] as 9Km East of Uwet. . The interpretation of magnetic anomalies here shows two (2) magnetic highs in profiles A& F, and four (4) magnetic lows in profiles B, C, D & E (profiles)

For Ugep, profiles A→ E were taken at Profile [A], as 7Km South-East of Ochon town; Profile [B], as 4.3Km North-East of Okumure; Profile [C] as 5Km North-East of Ekuri ; Profile [D], as 12Km South-West of Idomi And Profile [E], as 36Km South-East of Ugep. The interpretation of magnetic anomalies here shows two (2) magnetic highs in profiles A & D, and three (3) magnetic lows in profiles B, C, & E.

For Ugep, profiles A→ E were taken at Profile [A], as 6.2Km South of Ehoma Lake; Profile [B] as 4Km North-East of Afikpo; Profile[C], as 2Km North-West of Ishiagu .Profile[D] as 11Km North-West of Ehome lake. The interpretation of magnetic anomalies here shows four (4) magnetic highs in profiles B, C, D & E, and one (1) magnetic low in profile A.

4.1.10 Depth Estimation and Source Location by 3-D Euler Deconvolution

Here, depth estimates for a variety of geologic structures such as faults, magnetic contacts, dykes, sills, etc., will be identified through the combination of structural index and depth estimates. The method locates sources of anomaly by the degree of homogeneity which can be interpreted as a Structural Index (Thompson, 1982), by relating the potential field with its gradient components. In order words, initial assumption of the source type has to be made (structural index).

For this work, structural indices of 0 to 3 were used, while solutions were gotten for the standard Euler deconvolution using the different structural indices. Thus the euler deconvolution suggests a depth of the source horizon of 0m to a little above 300m.

The obtained results are as shown from Figures 4.46 to 4.53.

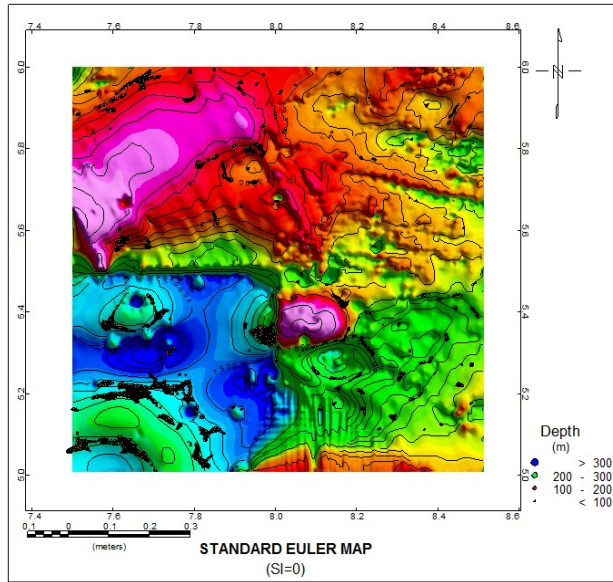


FIG. 4.46: STANDARD EULER MAP (SI=0)

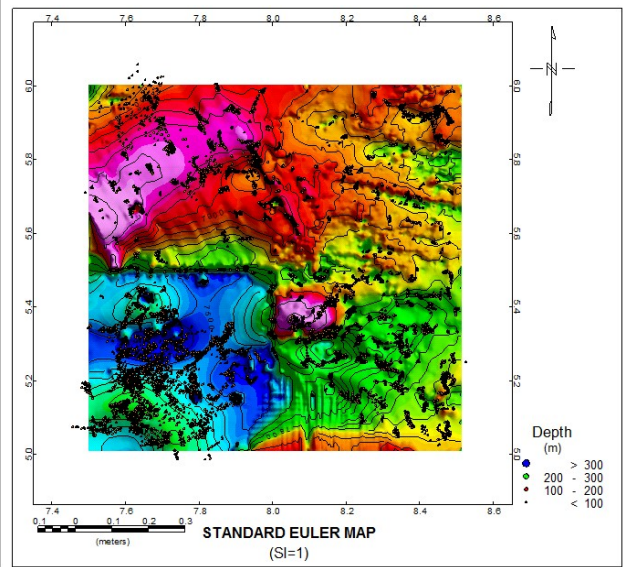


FIG. 4.47: STANDARD EULER MAP (SI=1)

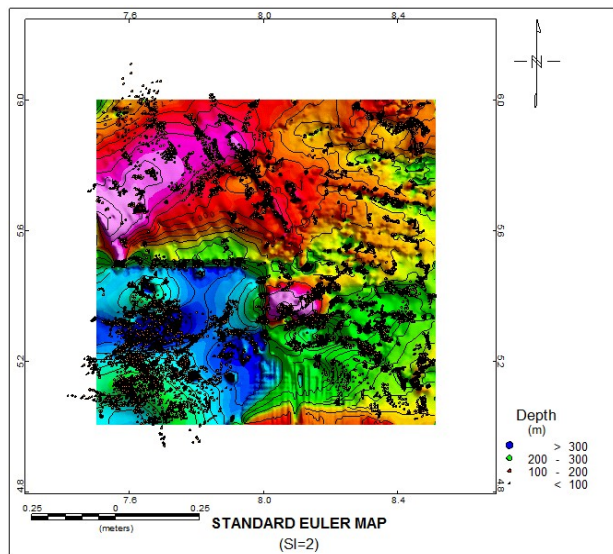


FIG. 4.48: STANDARD EULER MAP (SI=2)

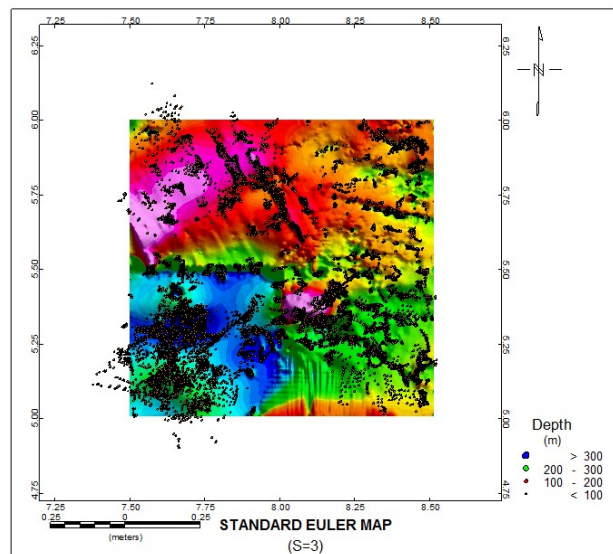


FIG. 4.49: STANDARD EULER MAP (SI=3)

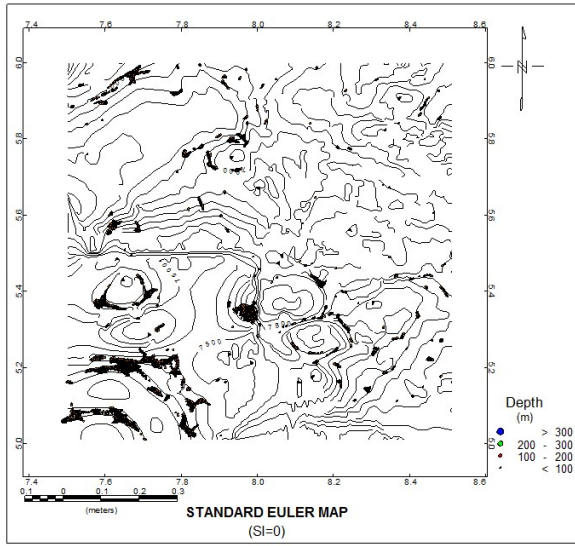


FIG. 4.50: STANDARD EULER MAP (SI=0)

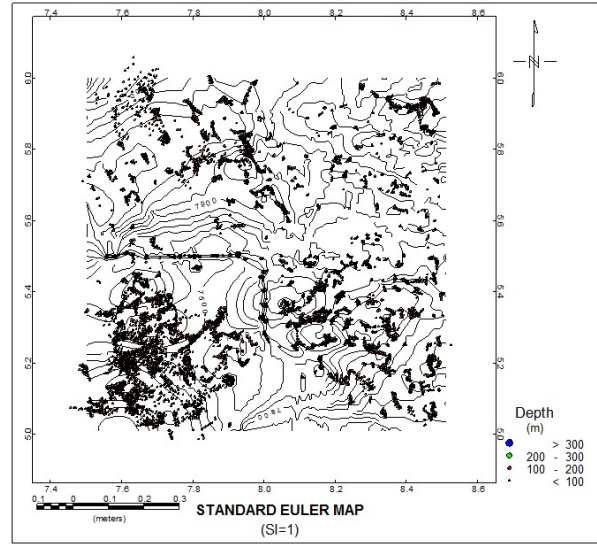


FIG. 4.51: STANDARD EULER MAP (SI=1)

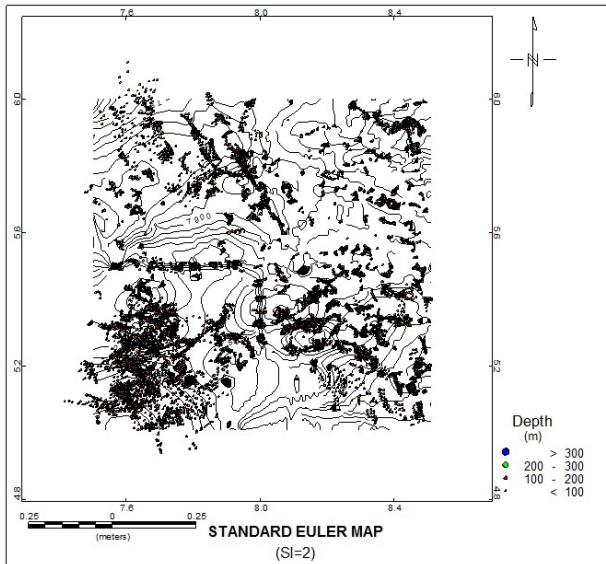


FIG. 4.52: STANDARD EULER MAP (SI=2)

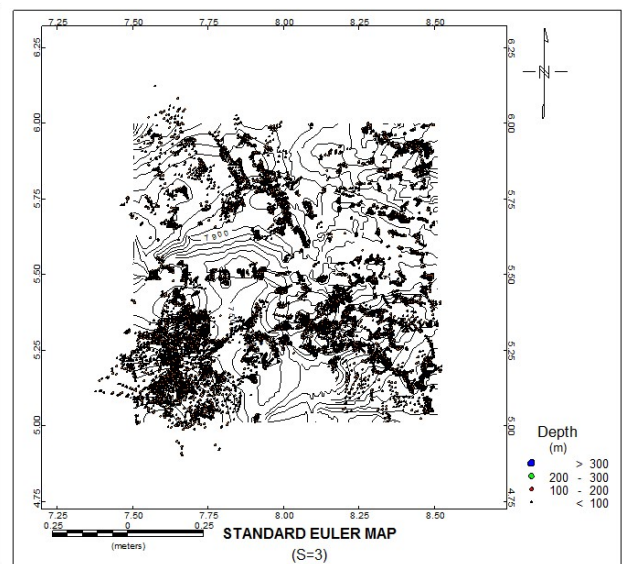


FIG. 4.53: STANDARD EULER MAP (SI=3)

A map of depth estimates as obtained by modelling at structural index of 0, with number of Infinite Dimensions as 3 (x,y,z), and synonymous with geologic setting of contact structures as sources.

A qualitative interpretation of the result with respect to clustered solutions as against few scattered solutions was done.

The highest occurrence of Geologic Contacts here is seen towards the SW part of the map around Adiasim, and west of Odoro Ikpe, at depths above 300m. This area is underlain by Coastal Plain Sands. Another occurrence of these Geologic Contacts is Around Arochukwu, bothering the major magnetic high in the area, with depth ranges between 200 – 300m, and underlain by the Imo Shale/Ebenebe Sandstone. Scattered solutions of these contacts occur towards the NW and towards SE of the derived Standard Euler Map.

For result of depth estimates as obtained by modelling at structural index of 1, with number of Infinite Dimensions as 2 (x and y), 2 (z and x-y), and synonymous with geologic setting of Sill and Dyke structures as sources, the Standard Euler map is also.

The highest occurrence of Sill and Dykes here occur at depth ranges between 200 – 300m and above 300m. They are seen towards the SW part of the map around Adiasim, Ikot Ekpene, Itu, and Odoro Ekpe. The area is underlain by Coastal Plain Sands, and part of Imo Shale/Ebenebe Sandstone. Another occurrence of these Sill and Dyke is at depth ranges between 200 – 300m, towards the SE part of the map, cutting across four Geological formations belonging to Imo Shale/Ebenebe Sst, Nkporo Shale/Afikpo Sst., ASU River Group and the Precambrian Basement Complex. Dykes and Sills also occur towards the NE end and NW end of the derived Standard Euler Map, and also around Afikpo and Owutu. Result of depth estimates this area is below 200m. Scattered solutions however occur all over the derived Standard Euler Map.

For result of depth estimates as obtained by modelling at structural index of 2, with number of Infinite Dimensions as 1 (x-y), 1 (z), and synonymous with geologic setting of Pipe and Horizontal Cylinder structures as sources, the Standard Euler map is also shown.

The highest occurrence of Structures in form of Pipe and Horizontal Cylinders here occur at depth ranges between 200 – 300m and above 300m. They are seen towards the SW part of the map around Adiasim, Ikot Ekpene, Itu, and Odoro Ekpe. The area is underlain by Coastal Plain Sands, and part of Imo Shale/Ebenebe Sandstone. Another occurrence of these Sill and Dyke is at depth ranges between 200 – 300m, towards the SE part of the map, cutting across four Geological formations belonging to Imo Shale/Ebenebe Sst, Nkporo Shale/Afikpo Sst., ASU River Group and the Precambrian Basement Complex. Dykes and Sills also occur towards the NE end and NW end of the derived Standard Euler Map, and also around Afikpo and Owutu. Result of depth estimates this area is below 200m. Scattered solutions however occur all over the derived Standard Euler Map.

For result of depth estimates as obtained by modelling at structural index of 3, with number of Infinite Dimensions as 0, and synonymous with geologic setting of Spheres as sources, the Standard Euler map was also shown.

4.1.11 Curie Point Depth, Heat Flow, and Geothermal Gradient Field from Spectral Analysis.

The Curie temperature is named after Pierre Curie, who showed that magnetism was lost at a critical temperature, where ordered magnetic moments, ferromagnetic, change and become disordered magnetic moments, paramagnetic.

Applying Spectral analysis here from the slope of the power spectrum, the top bound and the centroid of a magnetic layer are determined. Where the base depth of the magnetic source is:

$$Z = 2Z_0 - Z_t \quad (17)$$

Where Z_0 is the centroid of the magnetic layer, and Z_t is the top bound

Hence, Curie temperature is defined as the point at which certain materials lose their permanent magnetic properties, to be replaced by induced magnetism. At this temperature, ferromagnetic rocks become paramagnetic, and their ability to generate detectable magnetic anomalies disappears.

Heat flow estimates on the area were therefore made using the depth and thickness information.

TABLE 4.6: ESTIMATED CURIE DEPTH POINT, TEMPERATURE AND HEAT FLOW

TOWNS	CORDINATES				ESTIMATED DEPTHS(KM)			CURIE DEPTH POINT	dt/dz CURIE TEMP.	HEAT FLOW, q.
	X ₁	X ₂	Y ₁	Y ₂	D ₁	Z _t (D ₂)	Z ₀	Z _b (2Z ₀ -Z _t)	Θ/Z _b , at Θ=580	kdt/dz, at K=2.5Wm ⁻¹ k ⁻¹
AFIKPO	7.5	7.75	5.5	5.75	1.676	3.264	15.157	27.05	21.44177449	53.60443623
	7.5	7.75	5.75	6	0.897	1.986	13.857	25.728	22.54353234	56.35883085
	7.75	8	5.5	5.75	0.354	0.985	11.695	22.405	25.88707878	64.71769694
	7.75	8	5.75	6	1.648	3.234	15.321	27.408	21.16170461	52.90426153
UGEP	8	8.25	5.5	5.75	0.035	3.433	15.497	27.561	21.04422916	52.61057291
	8	8.25	5.75	6	0.989	3.344	15.51	27.676	20.95678566	52.39196416
	8.25	8.5	5.5	5.75	1.043	0.779	11.336	21.893	26.49248618	66.23121546
	8.25	8.5	5.75	6	0.763	2.379	14.522	26.665	21.75135946	54.37839865
UWET	8	8.25	5	5.25	1.66	3.787	15.921	28.055	20.67367671	51.68419177
	8	8.25	5.25	5.5	2.78	4.897	16.325	27.753	20.89864159	52.24660397
	8.25	8.5	5	5.25	0.654	2.933	14.757	26.581	21.82009706	54.55024265
	8.25	8.5	5.25	5.5	0.355	0.701	11.525	22.349	25.95194416	64.8798604
IKOT EKPENE	7.5	7.75	5	5.25	2.446	5.234	17.259	29.284	19.80603743	49.51509357
	7.5	7.75	5.25	5.5	2.211	5.764	17.926	30.088	19.27678809	48.19197022
	7.75	8	5	5.25	1.77	4.943	16.511	28.079	20.65600627	51.64001567
	7.75	8	5.25	5.5	2.568	6.789	18.815	30.841	18.80613469	47.01533673

TABLE 4.7: CALCULATED AVERAGE CURIE POINT DEPTH (KM) AND THEIR CORRESPONDING HEAT FLOW (mWm^{-2}) FROM SPECTRAL ANALYSIS

Spectral Block A $Z_0 = 15.157$ $Z_t = 3.264$ $Z_b = 27.05$ $q = 53.60$	Spectral Block B $Z_0 = 15.857$ $Z_t = 1.98$ $Z_b = 25.728$ $q = 56.358$	Spectral Block E $Z_0 = 15.497$ $Z_t = 3.43$ $Z_b = 27.561$ $q = 52.61$	Spectral Block F $Z_0 = 15.51$ $Z_t = 3.34$ $Z_b = 27.676$ $q = 52.39$
Spectral Block C $Z_0 = 12.995$ $Z_t = 0.98$ $Z_b = 22.405$ $q = 64.717$	Spectral Block D $Z_0 = 15.321$ $Z_t = 3.23$ $Z_b = 37.408$ $q = 52.90$	Spectral Block G $Z_0 = 13.136$ $Z_t = 0.77$ $Z_b = 21.893$ $q = 66.231$	Spectral Block H $Z_0 = 14.522$ $Z_t = 2.379$ $Z_b = 26.665$ $q = 54.378$
Spectral Block I $Z_0 = 15.921$ $Z_t = 3.78$ $Z_b = 28.055$ $q = 51.684$	Spectral Block J $Z_0 = 16.325$ $Z_t = 4.89$ $Z_b = 27.753$ $q = 52.246$	Spectral Block M $Z_0 = 17.259$ $Z_t = 5.23$ $Z_b = 29.284$ $q = 49.515$	Spectral Block N $Z_0 = 17.926$ $Z_t = 5.76$ $Z_b = 30.088$ $q = 48.19$
Spectral Block K $Z_0 = 14.757$ $Z_t = 2.93$ $Z_b = 26.581$ $q = 24.55$	Spectral Block L $Z_0 = 13.425$ $Z_t = 0.70$ $Z_b = 22.349$ $q = 64.879$	Spectral Block O $Z_0 = 16.511$ $Z_t = 4.94$ $Z_b = 28.079$ $q = 51.64$	Spectral Block P $Z_0 = 18.815$ $Z_t = 6.78$ $Z_b = 30.841$ $q = 47.015$

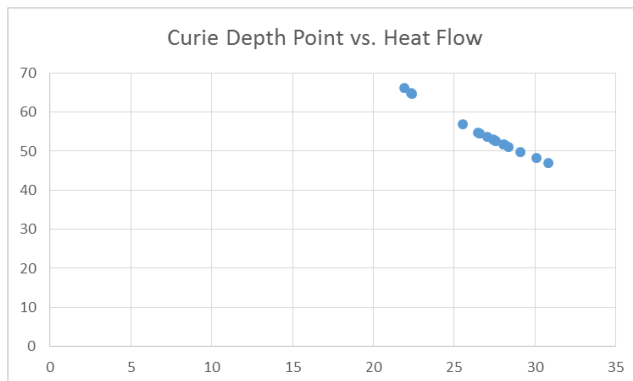


FIGURE 4.54: PLOT OF CURIE POINT DEPTH VERSUS HEAT FLOW

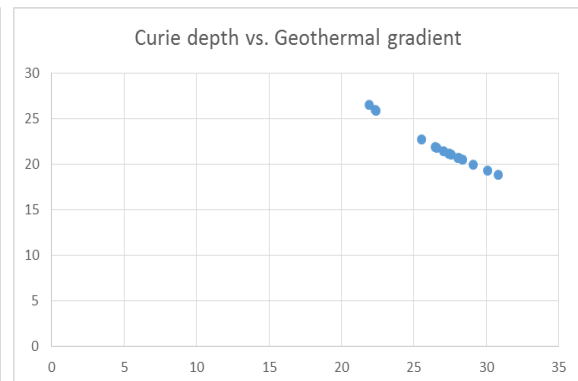


FIGURE 4.55: PLOT OF CURIE POINT DEPTH VERSUS GEOTHERMAL GRADIENT

Spectrum analysis have been applied to the HRAM data of the study area and Curie depths were determined. Then, heat flow values were determined with regards to the region by using the depths and taking into consideration of heat conductivity ($2.5Wm^{-1}k^{-1}$).

NOTE:

Curie point depth is greatly dependent upon geological conditions. Curie point depths are shallower than 10 km for volcanic and geothermal fields, between 15-25 km for island arcs and ridges, and deeper than 20 km in plateaus and trenches (Tanaka et al., 1999). Generally, the units that comprise high heat flow values correspond to volcanic and metamorphic regions since these two units have high heat conductivities. Additionally, tectonically active regions affect the Curie depth and heat flow.

Because the average heat flow in thermally “normal” continental regions is around 60 mW/m². Values in excess of about 80 -100mW/m² indicate anomalous geothermal conditions (Jessop et al., 1976). Accordingly, three prospects at Afikpo, Ugep and Uwet, with heat flow values of 64.71mW/m², 66.23 mW/m² and 64.87 mW/m² respectively, are recommended for further geothermal exploration. Geothermal gradients in these areas may provide good source(s) of geothermal energy, with their Curie temperatures greater than 24⁰C being reached at depths of less than 2 km.

From the derived table, the depth to the Centroid (Z_o) ranges from 11.336 km to 18.815 km. On the other hand, the depth to the top boundary (Z_t) of magnetic sources ranges from 0.03 km to 2.78 km (below sea level) Table.

The equivalent Curie Depth Point ranges from 21.89 km to 30.84 km. Heat flow values for the study area ranges from 47.01mW/m² to 66.23mW/m².

The results so obtained from a plotting a graph of Heat Flow as against Curie Depth Point, supports the conclusion that Curie depth is shallow where the heat flow is high.

4.2 Data Presentation, Results and Interpretation: Landsat-ETM Data.

4.2.1 Digital Elevation Model (DEM)

The elevation range within the coordinates of the study area, and as obtained from the Digital Elevation Model (DEM), is between -3m and 864 m.

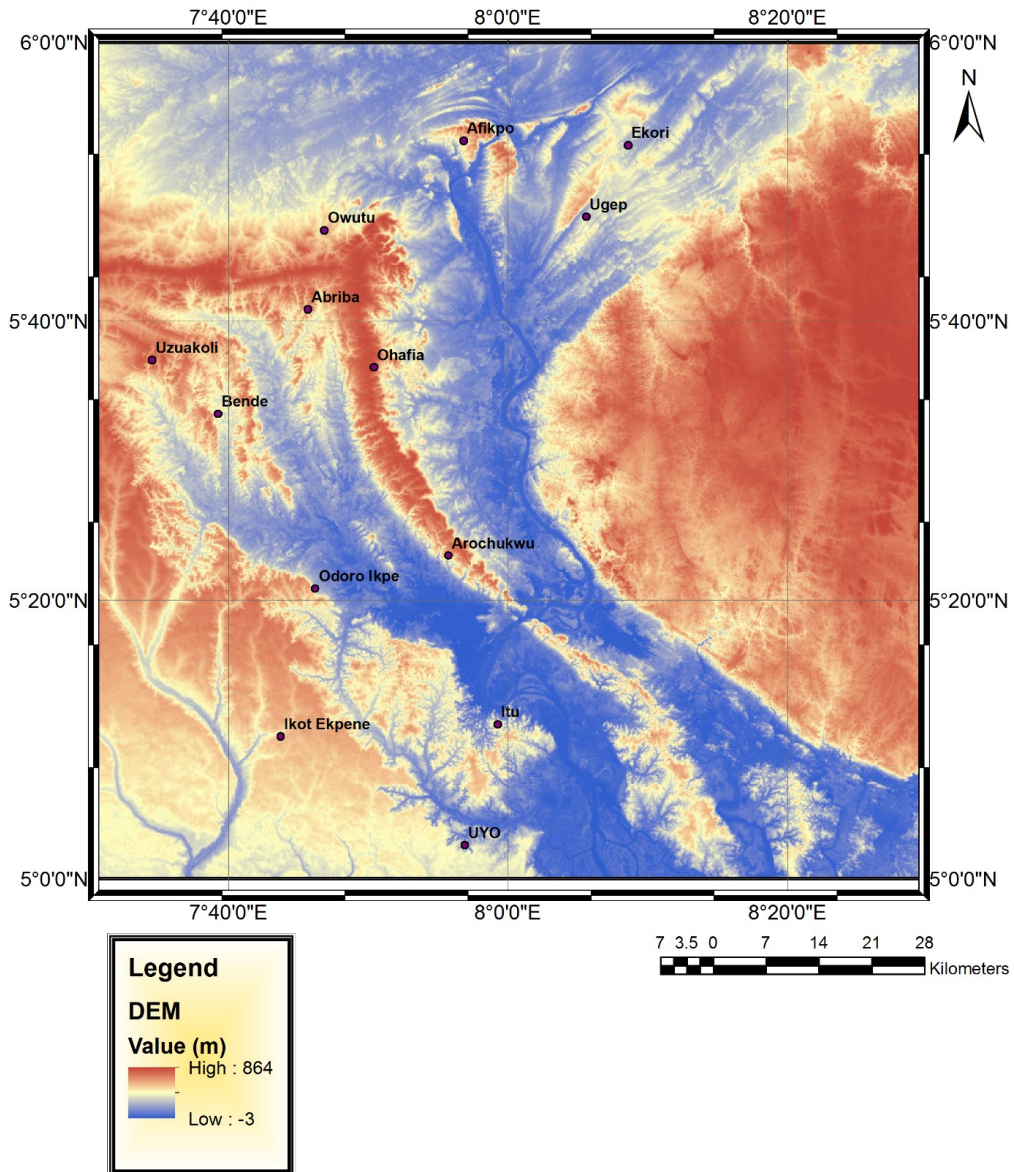


FIG. 4.56: DIGITAL ELEVATION MODEL OF THE STUDY AREA

For an interpretation legend, areas tending to the dark-red coloration are highlands, while areas tending to a blue coloration are lowlands.

Thus, we attribute our first highland to the Undifferentiated Precambrian Basement Complex, which predominantly dominates the easterly part of the DEM. This area occurs at an elevation of about 864m.

Another highland of an almost equal elevation is to the North-West of the map, a continuous ridge-like occurrence, attributed to the Maastrichtian_Danian Upper Coal Measure of the Nsukka Formation. Locations around these areas are Ohafia, Arochukwu, Uzuakoli, and of course, areas within the Undifferentiated Basement Complex. There is also another high elevation towards the Northerly direction, at Afikpo.

Tending from High elevation towards lower elevation, i.e., from dark red towards light-yellow, there is a decreasing elevation, possibly between 500m -700m, at Ugep, and Ekori, NE of the map, both attributed to the Turonian Ezeaku Shale Group. The same elevation range occurs SW of the DEM at Itu, and Odoro Ikpe, attributed to the Bende-Ameki Group, and Bende, attributed to the Imo Shale/Ebenebe Sandstone.

At mid elevations between -3m and 864m, there are the yellow colored areas on the DEM. One of such areas is towards the east of the map and flanks the Basement Complex and is attributed to the Albian ASU River Group. It also occurs towards the SW part of the DEM at Adiasim and in patches all over the Study area.

The lowest elevations within the study are as obtained from the Digital Elevation Model, occurs at about -3m and are attributed to the river and stream flows within the study area. One of such low elevations run NS of the DEM in line with the major river-flow in the area. The second part is towards the lower SE of the DEM. Another part is towards the North and NW of the DEM, and the last, occurs towards the Westerly direction and at the lower SW of the DEM. These low elevations so obtained can be interpreted to be in-line with the dendritic drainage pattern of the study area.

4.2.2 Lineament Density, Lineament on Drainage, and Lineament on Edge Enhanced Band5.

A lineament is a linear feature in a landscape which is an expression of an underlying geological structure such as a fault.

4.2.2.1 Lineament Density

In terms of density, the range of lineaments within the coordinates of the study area is between 0 – 60000 m/100km².

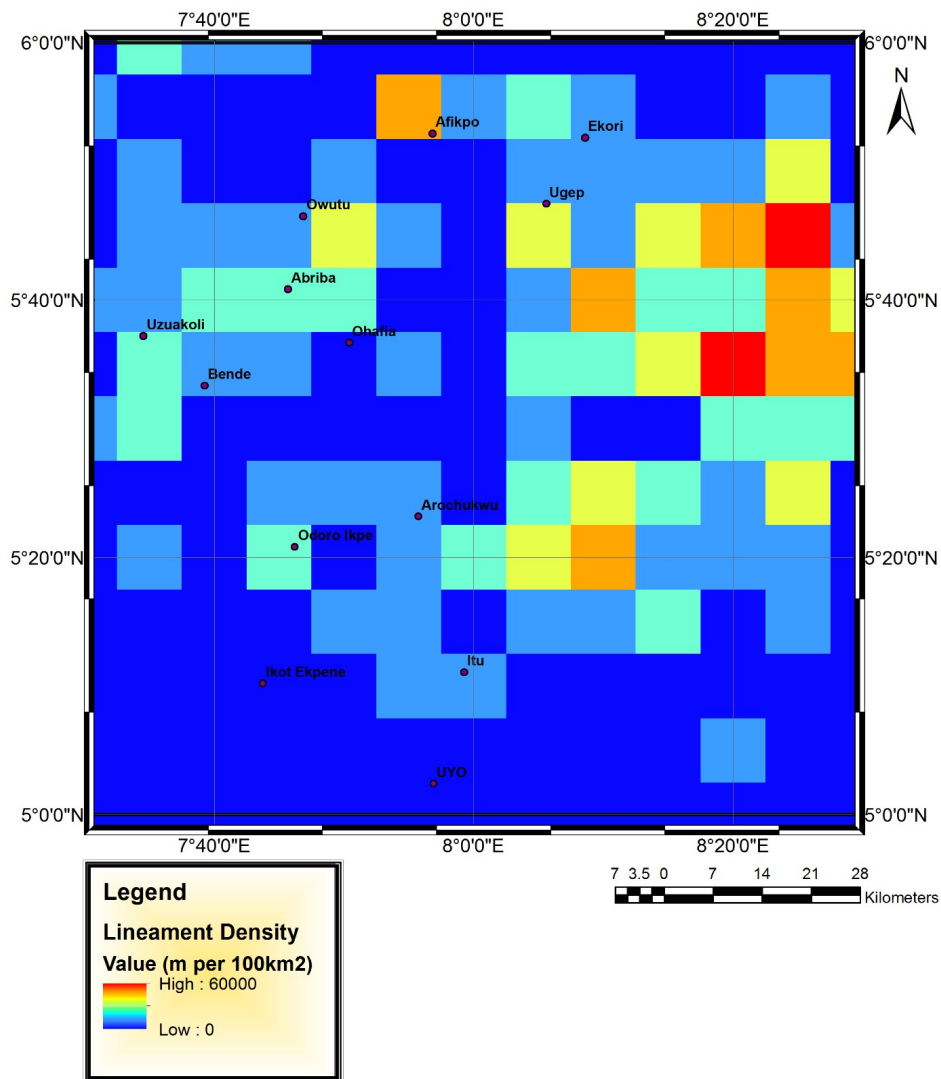


FIG. 4.57: LINEAMENT DENSITY MAP OF THE STUDY AREA

The areas with highest lineament density are two square grids within the undifferentiated Precambrian Basement Complex of about 60000 m/100km². The second areas with high lineament density are also enclosed within the Basement Complex at 6 square grids, and is also observed North of the Lineament Density map, at Afikpo.

There are also areas with Lineament Density values between 30000 – 60000 m/100km² (with yellow colors), clustered mostly towards the East of the map and associated with the Undifferentiated Precambrian Basement Complex. Same lineament density occurs at Owuta (Nsukka Formation).

At mid value of Lineament Density of about 30000 m/100km² for the study area, there are the lemon colored areas on the map clustered also within the Basement Complex. It is also observed west of the map at Abriba, Uzuakoli, Odoro Ikpe and North of the map between Afikpo and Ekori.

The areas with lowest lineament density within the study are in almost all parts of the map, but more pronounced in the Southern part of the map comprising mostly of Alluvium and Coastal Plain Sands.

4.2.2.2 Lineament on Drainage

In terms of deriving a relationship between the drainage pattern of the study area and the Lineament, the map on Fig. 4.58 was derived.

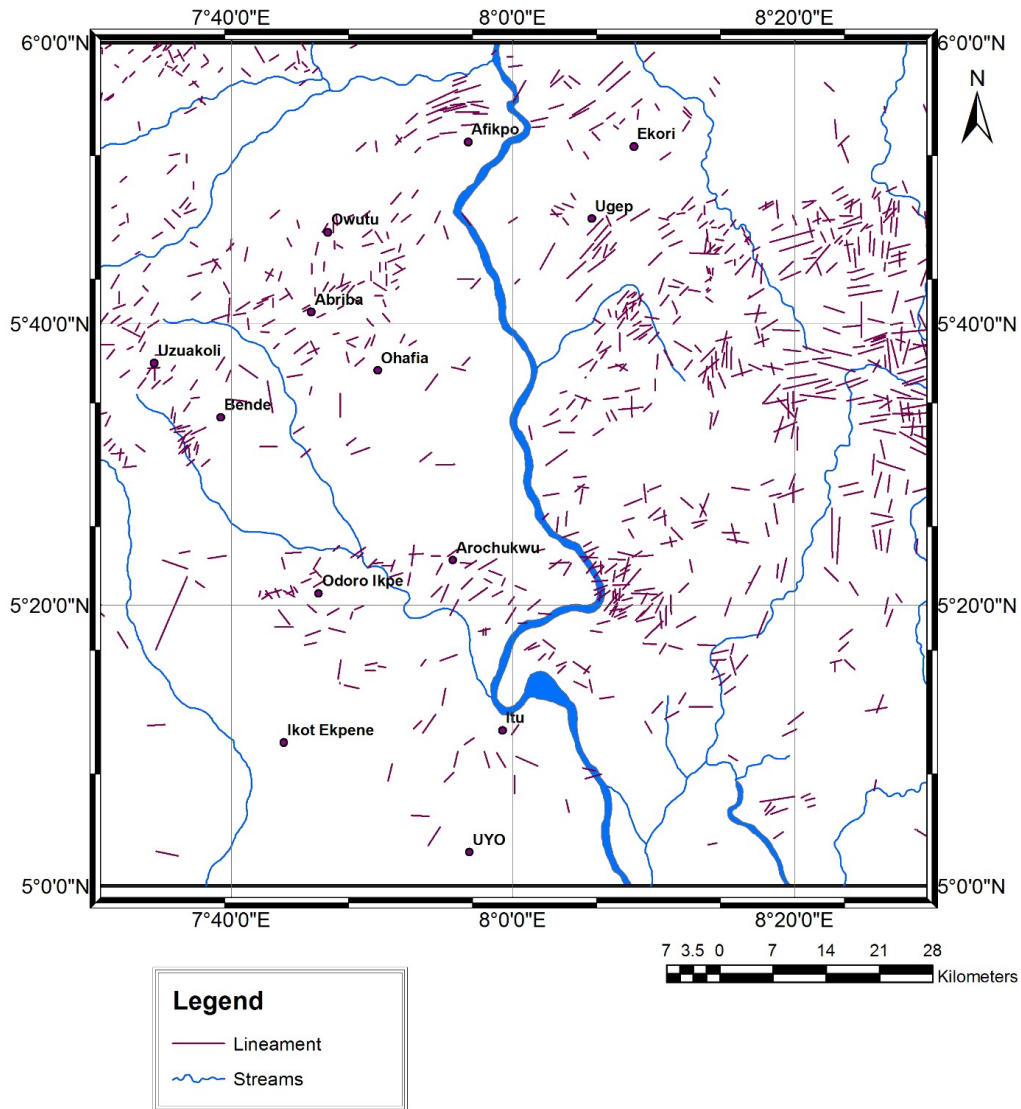


FIG. 4.58: LINEAMENT ON DRAINAGE MAP OF THE STUDY AREA

NOTE: The trend directions of the lineament patterns will be treated later with a Rose Diagram, hence qualitative interpretation given here will be based on the cluster patterns of the derived lineaments.

For drainage, the study area exhibits a dendritic pattern, and is drained mainly by the Cross River with many tributaries such as Aboine, Enyong, Udene and Iyiokwu Rivers which in turn empties into the Atlantic Ocean. The Rivers are perennial and usually overflow their banks at the peak of the rainy season.

The major lineament cluster within the study area is in the easterly direction of the map and is attributed to the Undifferentiated Precambrian Basement Complex. It also occurs within the Ezeaku Shale Group at Ugep, Ekori, and towards the Southern part of this Formation.

There are not much lineament representation towards the NNE, and towards the SSW of the map.

There are also lineament clusters towards the NW of the map, at Afikpo, Owutu, Abriba, Ohafia, Bende, and Uzuakoli.

Lineament clusters are also observed at most places along the River-paths. An example of this is that East of Arochukwu, on the channel of the Cross River, a major cluster is observed. Hence it can be tentatively interpreted that the lineament patterns of the study area played a leading role in the creation process of the drainage pattern of the study area.

4.2.3 Normalized Difference Vegetation Index (NDVI) Map

A vegetation index is an indicator that describes the greenness — the relative density and health of vegetation — for each picture element, or pixel, in a satellite image. The output of NDVI (figure) is a measure of vegetation richness of an area. Vegetation indices are based on the observation that different surfaces reflect different types of light differently.

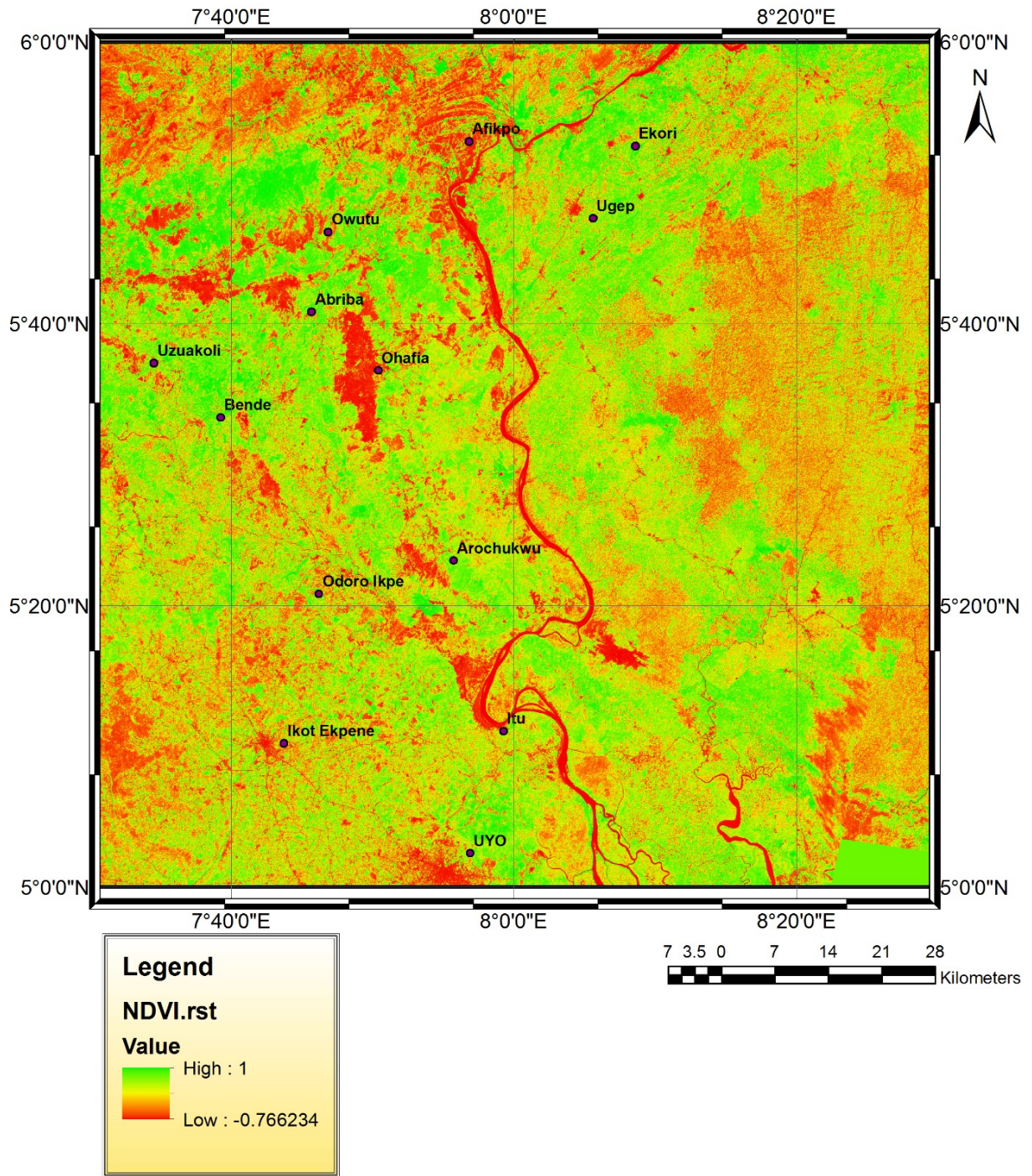


FIG. 4.59: NDVI MAP OF THE STUDY AREA

Although there are several vegetation indices, one of the most widely used is the Normalized Difference Vegetation Index (NDVI). NDVI values range from +1.0 to -1.0. Areas of barren

rock, sand, or snow usually show very low NDVI values (for example, 0.1 or less). Sparse vegetation such as shrubs and grasslands or senescing crops may result in moderate NDVI values (approximately 0.2 to 0.5). High NDVI values (approximately 0.6 to 0.9) correspond to dense vegetation such as that found in temperate and tropical forests or crops at their peak growth stage.

Photosynthetically active vegetation, in particular, absorbs most of the red light that hits it while reflecting much of the near infrared light. Vegetation that is dead or stressed reflects more red light and less near infrared light. Likewise, non-vegetated surfaces have a much more even reflectance across the light spectrum.

By taking the ratio of red and near infrared bands from a remotely-sensed image, an index of vegetation “greenness” can be defined. The Normalized Difference Vegetation Index (NDVI) is probably the most common of these ratio indices for vegetation. NDVI is calculated on a per-pixel basis as the normalized difference between the red and near infrared bands from an image:

$$\text{NDVI} = (\text{NIR}-\text{RED})/(\text{NIR}+\text{RED}) \quad (4c)$$

Where NIR is the near infrared band value for a cell, RED is the red band value for the cell and NDVI can be calculated for any image that has a red and a near infrared band.

Thus the NDVI map of the study area was generated.

Because water reflects very little NIR light, there is a pronounced low NDVI value of about -0.766234 along the full length of the Cross River course on the map. Same values of NDVI occur at Afikpo, Ohafia, Itu, and in patches of red across the map.

Following the low NDVI values are areas shaded in orange and green colors, with NDVI values in-between 0 and 1. These areas can be attributed to soils with little vegetation and sparse vegetation, respectively.

Areas with high vegetation within the study area are those shaded in green color and corresponds to thick vegetation. This is so because these areas are associated with highly photosynthetically-active vegetation, signified the larger difference between the red and near infrared radiation

recorded by the sensor. The NDVI value here, is 1, and occur in several parts of the map. It is however, more pronounced in towards the east of the NDVI map.

4.2.4 Color Composites

The composites were generated for the purpose of enhancing spectral signatures of the images for the study area thus enhancing the observation of the different patterns thus aiding in the interpretation of features and their limits.

The composite colours are shown in the figures bellow:

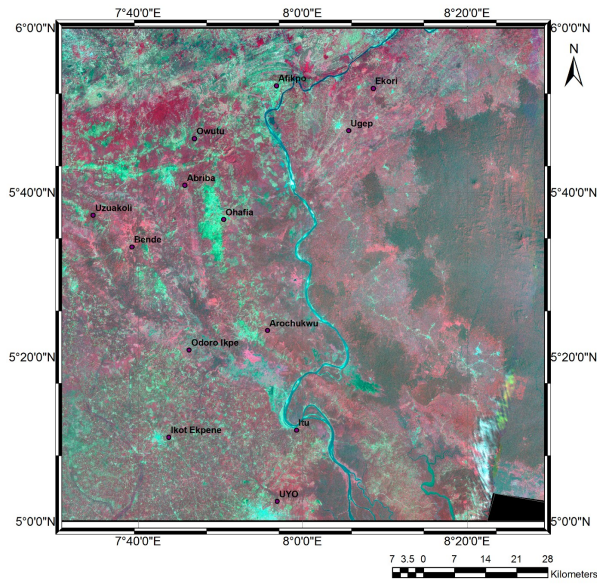


FIG 4.60: RGB 432 COLOR COMPOSITE MAP

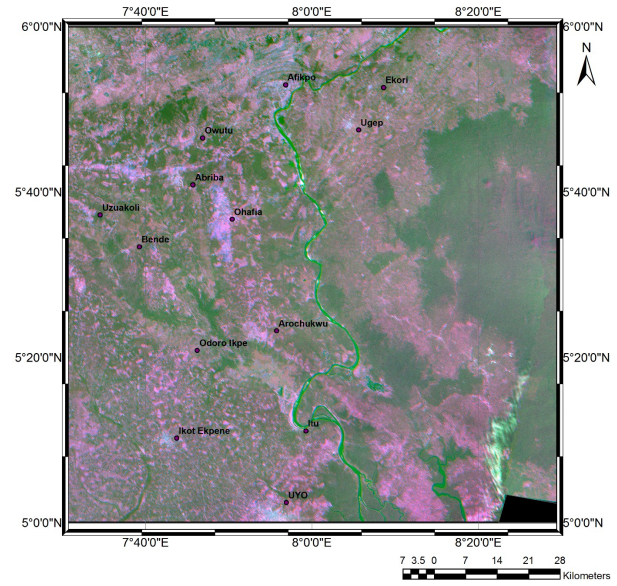


FIG. 4.61: RGB 517 COLOR COMPOSITE MAP

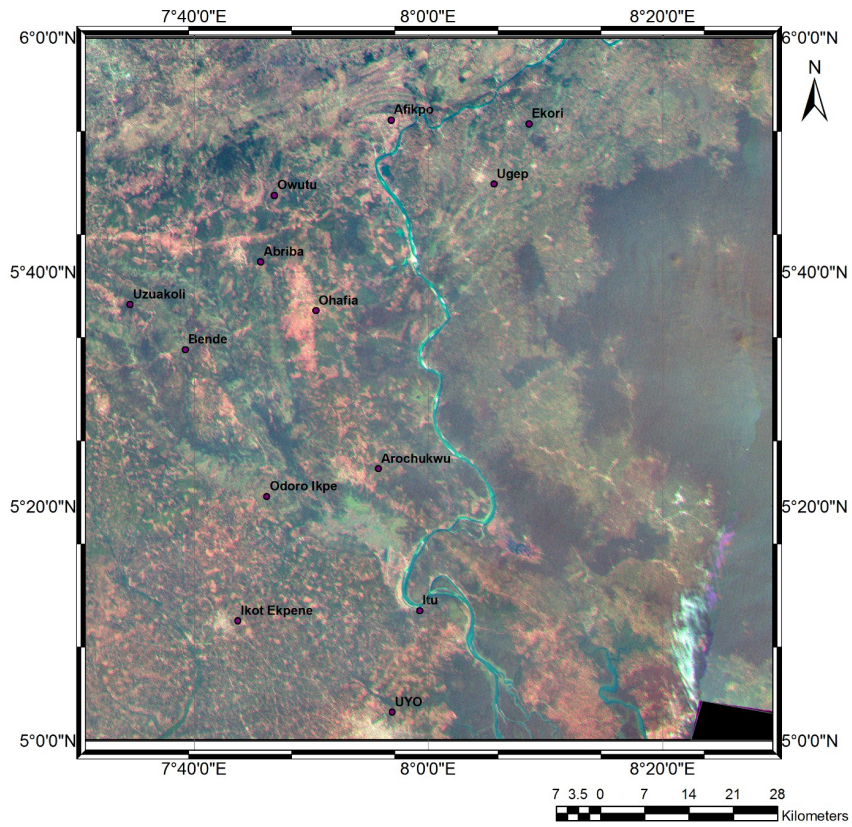


FIG. 4.62: RGB 721 COLOR COMPOSITE MAP

The appearance of features in the generated colour composite maps is shown in the table below.

Table 4.8: Appearance of Features on Composite Images

	TRUE COLOUR	FALSE COLOUR
	Red: Band 3 Green: Band 2 Blue: Band 1	Red: Band 4 Green: Band 3 Blue: Band 2
Trees and Bushes	Olive Green	Red
Crops	Medium to light Green	Pink to red
Wetland vegetation	Dark green to black	Dark red
Urban areas	White to light blue	Blue to gray
Water	Shades of blue and Green	Shades of blue
Bare soil	White to light gray	Blue to gray

4.2.5

Rose Diagram

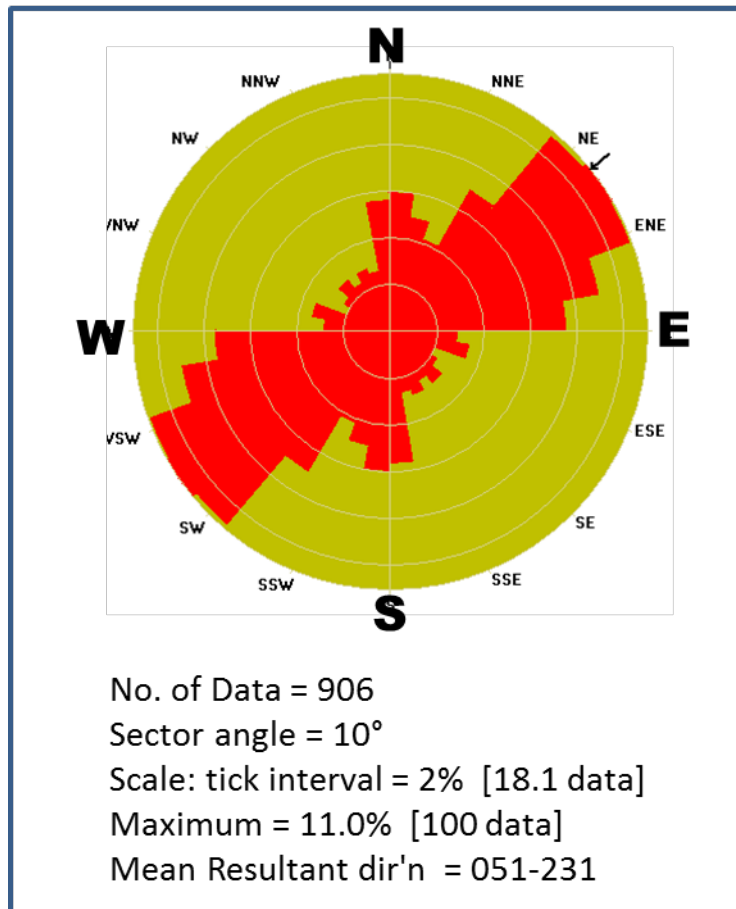


FIG. 4.63: ROSE DIAGRAM

The rose diagram revealed three major trends: NE-SW, ENE-WSW and N-S. However, several other trends are observed which have low frequency on the diagram. The dominant NE-SW trend reflects the younger tectonic events. Similarly, subsurface linear structures identified in study area from polynomial surfaces (first - fourth degree regional and residual maps) revealed tectonic features with principal trend directions. The predominant NE-SW, ENE-WSW fault trends would so have played an essential role in the control of the geodynamic evolution of the region, as opposed to the right angled major rift faults of the Benue Trough, but however, consists of NW-SE trending basement horsts (the Oban massif and the Ituk-high) separated by a graben, the Ikang trough. The mean resultant direction taken for the derived Rose diagram is 051-231.

CHAPTER FIVE

CONCLUSION AND RECOMMENDATIONS

Conclusively, the evolution of Calabar Flank is a result of the separation of African and South American plates. The total sediment thickness is about 3.403 km, with a feathered edge of outcrops north of Calabar along the margin of the Oban basement. The presence of high total magnetizations compared to other rock types is attributed to Igneous and crystalline metamorphic rocks in the study area, whereas the lower magnetizations are attributed to sedimentary rocks and poorly consolidated sediments. In the east, it extends up to the Cameroon volcanic ridge.

Depth to basement, faults in the basement surface and relief of the basement was estimated due to its direct relevance to the depositional and structural history of a basin. The Data was passed through non-linear filters, high pass and low pass filters, etc, in order to study both the deeper and shallower sources of magnetic anomalies. Values of Total Magnetic Intensity as obtained from digitizing the Aeromagnetic data, ranges from 7485.4 gammas – 7987.0 gammas.

The methods of magnetic depth estimation employed in this study are Spectral Methods and 3D Euler Deconvolution. The spectral method was also used to determine the curie depth point, Curie temperature and heat flow of the study area, while the Euler deconvolution pointed out the causes of magnetic anomalies and their depths, thereby creating 4 maps showing the locations and the corresponding depth estimations of geologic sources of magnetic anomalies on two-dimensional grids. The structural elements observed in the study area as modelled from Euler deconvolution are contact structures, dykes, sills, and other geologic structures in form of spheres, pipes and horizontal cylinders.

The interpretation of magnetic anomalies at Ikot-Ekpene shows three (3) magnetic highs in profiles A, C, & E, and two (2) magnetic lows in profiles B & D. It shows two (2) magnetic highs in profiles A & F, and four (4) magnetic lows in profiles B, C, D & E at Uwet. At Ugep, magnetic anomalies interpretation shows two (2) magnetic highs in profiles A & D, and three (3) magnetic lows in profiles B, C, & E. Finally, the interpretation shows four (4) magnetic highs in profiles B, C, D & E, and one (1) magnetic low in profile A.

Economically, the basin has low petroleum potential because the average sedimentary thickness of 3.403 km is very thin for entrapment of crude oil. Another reason put up is that high magnetic anomalies may be associated with igneous and/or metamorphic rocks which have high susceptibility than sedimentary rocks. This implies that the temperature accompanying tectonic activity in the area must have cooked the source rock, if any beyond the oil window phase of maturation.

Geothermal reservoirs are sometimes formed when rising hot water and steam is trapped in permeable and porous rocks under a layer of impermeable rock, which could be a powerful source of energy. Therefore, heat flow estimates on the study area were made using the depth and thickness information, taking heat conductivity ($2.5\text{Wm}^{-1}\text{k}^{-1}$) into consideration. Three prospects at Afikpo, Ugep and Uwet, with heat flow values of 64.71mW/m^2 , 66.23mW/m^2 and 64.87mW/m^2 respectively, are recommended for further geothermal exploration. Geothermal gradients in these areas may provide good source(s) of geothermal energy, with their Curie temperatures greater than 24°C being reached at depths of less than 2 km. The results so obtained from a plotting a graph of Heat Flow as against Curie Depth Point, supports the conclusion that Curie depth is shallow where the heat flow is high.

Economically, mineralization in the Basement Complex, includes tin and gold (mined in colonial days from Akwa Ibami and Akamkpa), ilmenite, columbite-tantalite, kaolin, graphite, manganese and marble; while in the sedimentary basins are high quality limestones, salts, barytes, leadzinc, and uranium prospects.

REFERENCES

- Adeigbe, O.C., & Jimoh, Y.A. (2013). Geochemical Fingerprints: Implication for provenance, tectonic and depositional settings of the Lower Benue Trough sequence, southeastern Nigeria. *Journal of Environment and Earth Science*, 3 (10), 115-140.
- Adeleye, D.R., & Fayose, E.A. (1978). Stratigraphy of the type section of Awi Formation, Odukpani area, southeastern Nigeria. *Journal of Mining and Geology*, 15, 33-37.
- Ajibade, A.C., Woakes, M., & Rahaman, M.A. (1989). Proterozoic crustal development in the Pan-African regime of Nigeria. In: *Geology of Nigeria (2nd revised edition)*, Edited by Kogbe, C.A. Rockview Nigeria Ltd, Jos, Nigeria. 57-69
- Al Moush, H., Hammoun, N., Al Farajat, M., Salameh, E., Diabat, A., Hassonah, M., & Al Adamat, R. (2013). Integrating of aeromagnetic data and landsat imagery for structural analysis purposes: a case study in the southern part of Jordan. *Journal of geographic information system*, 5(2), 15-22.
- Ananaba, S.E., (1991). Dam sites and crustal megalineaments in Nigeria. *ITC Journal Vol. 1*, pp. 26-29.
- Ananaba, S.E., and Ajakaiye, D.E., (1987). Evidence of tectonic control of mineralization of Nigeria from lineament density analysis: A Landsat study; *Int. Journal. Rem. Sensing*; vol.1, no.10; pp. 1445-1453
- Benkhelil, J. (1987). Cretaceous Deformation Magmatism and metamorphism in the Lower Benue Trough, Nigeria. *Geol. Journ. Vol. 22*, pp. 467-493.
- Benkhelil, J., (1988). Structure et evolution geodynamique du Basin intracontinental de la Benoue (Nigeria) *Bull. Centres Rech., Explor. Prod. Elf Aquitaine* 1207, 29-128.
- Blakely, R.J., (1995). *Potential theory in gravity and magnetic applications*: Cambridge Univ. Press.
- Burke, K., Dessauvagie, T.F.J., & Whiteman, A.J. (1972). Geological history of the Benue Valley and adjacent areas., In : *African Geology* (Edited by Dessauvagie, T.F.J., and Whiteman, A.J). Ibadan University Press; Ibadan, Nigeria. 187-205
- Colwell, R. 1997. EstimateS: Statistical estimation of species richness and shared species from samples. Version 7.5. User's guide and application published online. [URL: <http://viceroy.eeb.uconn.edu/estimates>]

- Dessauvague and A.J. Whiteman (Eds.), African Geology, University of Ibadan, Nigeria, pp. 251-266.
- Ehinola, O.A., Sonibare, O.O., Javie, D.M. and Oluwale, E.A (2008). Geochemical Appraisal of Organic Matter in the Mid-Cretaceous Sediments of the Calabar Flank, Southeastern Nigeria. *European Journal of Scientific research*, 23, 4, pp 567 – 577.
- Ekpo, B.O., Essien, N., Fubara, E.P., Ibok., U.J., Ukpabio, E.J., & Wehner, H. (2013). Petroleum geochemistry and Cretaceous outcrops from the Calabar Flank , Southeastern Nigeria. *Marine and Petroleum Geology*, 48, 171- 185.
- Ekweozor, C.M., Udo, O.T., 1988. The oleananes: origin, maturation and limits of occurrence in southern Nigeria sedimentary basins. In: Mattavelli, L., Novelli, L. (Eds.), *Advances in Organic Geochemistry 1987. Org. Geochem. vol. 13 (1e3)*, 131e140.
- Ekwere, S.J., 1993. Geochemistry of subsurface limestone samples from Etankpini, Calabar Flank, Southeastern Nigeria. *Trop. J. Appl. Sci.* 3, 9e17.
- Essien, J.P, M. Ubom and S.P. Antai, 2005. Productivity and distribution of epipellic microalgae along salinity gradients in mangrove swamp of the Qua Iboe Estuary (Nigeria). *Environ. Monitoring Assess.*, 121: 65-75.
- Gunn, P.J., 1997. Application of aeromagnetic surveys to sedimentary basin studies; *AGSO Journal of Australian Geology and Geophysics*, 17(2): 133-144.
- Kangoko, R., Ojo, S.B. and Umego, M.N., (1997). Estimation of Basement depths in the Middle Cross River basin by Spectral analysis of the Aeromagnetic field. *Nig. Journ. Of Phys.* Vol. 9, pp.30-36.
- Kasidi S. and Nur A., 2013. Estimation of Curie depth flow and geothermal gradient inferred from aeromagnetic data over Jalingo and environs north-eastern Nigeria. *International journal of Science and Emerging Technologies*, Vol. 6 No. 6
- Kowalik, W.S., & Glenn, W.E. (1987). Image processing of aeromagnetic data and integrating with landsat images for improved structural interpretation; *Geophysics*, 52, 875-884.
- Mello, M.R., Gaglianone, P.C., Brassel, S.C., Maxwell, J.R., 1988a. Geochemical and biological marker assessment of depositional environments using Brazilian offshore oils. *Marine Pet. Geol.* 5, 205e223.

- Mello, M.R., Koutsoukos, E.A.M., Hart, M.B., Brassel, S.C., Maxwell, J.R., 1989. Late Cretaceous anoxic events in the Brazilian continental margin. *Org. Geochem.* 14 (5), 529e542.
- Mello, M.R., Mohriak, W.U., Koutsoukos, E.A.M., Figueira, J.C.A., 1991. Brazilian and West African oils. Generation, migration, accumulation and correlation. In: *Proceedings of the 13th World Petroleum Congress*. John Wiley & Sons, New York, pp. 153e164.
- Milligan, P.R. and Gunn P.J. (1997) Enhancement and Presentation of Airborne Geophysical. AGSO, *Journal of Australian Geology and Geophysics*, 17, 64-74.
- Murat, R.C., (1972). Stratigraphy and Palaeography of the Cretaceous and Lower Tertiary in Southern Nigeria. In: T.F.J.
- Nwachukwu, S.O. (1972). The tectonic evolution of the Southern portion of the Benue Trough, *Nigeria Geol. Mag.* 109, 411-419.
- Nwajide, C.S. (1990). Cretaceous Sedimentation and Paleogeography of the Central Benue Trough. In: Ofoegbu, C.O; (Ed.), *The Benue. Trough structure and Evolution International Monograph Series*, Braunschweig, pp. 19-38.
- Nwankwo CN, Ekine AS, Nwosu LI (2009). Estimation of the heat flow variation in the Chad Basin Nigeria. *J. Appl. Sci. Environ. Manage.* 13(1): 73-80.
- Nyong, E. E. (1995). Geological Excursion Guide book to Calabar Flank and Oban Massif. In the 31st Annual conference of the Nigerian Mining and Geosciences Society, Calabar, March 12 -16.
- Nyong, E. E., and Ramanathan, R. (1985). A record of oxygen-deficient paleoenvironments in the Cretaceous of the Calabar Flank, SE Nigeria. *Journal of African Earth Sciences* 3(4):455-460.
- Obi, C.G. (2000). Depositional Model for the Campanian-Maastrichtian Succession, Anambra Basin, Southeastern Nigeria. Ph.D Thesis, University of Nigeria, Nsukka, Nigeria.
- Odegard, M.E., and Berg, J.W., (1965). Gravity interpretation using the Fourier integral, *Geophysics*, 5. No. 3, pp. 424-38.
- Odumodu, C.F., 2012. Temperatures and Geothermal gradient fields in the Calabar Flank and parts of the Niger Delta, Nigeria. *Petroleum Technology Development Journal*. Vol. 2, No. 2

- Odumodu, C.F.R., 2009b. Subsurface temperatures, Geothermal gradients and Hydrocarbon Studies in the Calabar Flank. *Global Journal of Geological Sciences*. 7 (1), pp 55 – 65.
- Ofoegbu, C. O., (1988). An Aeromagnetic Study of Part of the Upper Benue Trough, Nigeria. *Jour. Afr. Earth Sci.*, 7, 77- 90.
- Ofoegbu, C. O., and Onuoha, K. M.,(1991). Analysis of magnetic data over the Abakaliki Anticlinorium of the Lower Benue Trough, Nigeria. *Marine and Petr.Geol.* vol. 8.
- Okereke, C.N., and Ananaba, S.E., (2006). Deep crustal Lineament inferred from aeromagnetic anomalies over the Niger Delta, Nigeria. *J. of Mining and Geol.* Vol. 42, pp.127-131.
- Olade, M.A. (1975). Evolution of Nigeria's Benue Trough (aulacogen): A tectonic smodel. *Geol. Mag.* 112, 576-583.
- Olade, M.A.D., 1975. Trace-element and isotopic data and their bearing on the genesis of Precambrian spilites from Athapuscow aulacogen, Great Slave Lake, Canada. *Geol. Mag.* 112, 283–93.
- Onyedim, G.C., Awoyemi, M.O., Ariyibi,E.A., and Arubayi.J.B, (2006).Aeromagnetic imaging of the basement morphology in part of the Middle Benue Trough, Nigeria, *Journal of Mining and Geology*,vol.42 (2), pp.157-163.
- Opara A.I. (2014). Structural Interpretation of the Afikpo Sub-basin: evidences from airborne magnetic and Landsat ETM data. *Elixir Earth Sci.* 71 (24546-24552).
- Opara A.I., 2014. Structural and tectonic features of Ugep and Environs, Calabar Flank, Southeastern Nigeria: Evidences from aeromagnetic and Landsat-ETM data. *MITTEILUNGEN KLOSTERNEUBURG* 64(2014) 7.
- Osemwota I.O., J.A.I. Omueti and A.I. Ogboghodo, 2008. Distribution of magnesium forms in surface soils of Central Southern Nigeria. *South African Journal of Plant and Soil.* 01 PG1526.
- Petters, S.W. (1982).Central West African Cretaceous Tertiary benthic foraminifera and Stratigraphy. *Palaeotographica(A)*, 179, 1-104.
- Petters, S.W., (1982). Central West African Cretaceous–Tertiary Benthic Foraminifera and Stratigraphy. *Paleontographica B.* 179 pp.1-104.
- Ragani, R.T., & Ebinger, C.J. (2008). Aeromagnetic and landsat – TM structural Interpretation for identifying regional groundwater exploration targets, southcentral Zimbabwe Craton. *Journal of Applied Geophysics*, 65, 73-83.

- Ramasamy, S.M. (2010). Significance of surface lineaments for gas and oil exploration in parts of Sabatayan Basin, Yemen. *Journal of Geography and Geology*, 2(1), 119-128.
- Reid, A.B. (1990). Magnetic interpretation in three dimensions using Euler deconvolution. *Geophysics*. Vol. 55, No. I (January 1990); P. 8&91.
- Reijers, T.J.A., and Petters, S.W., 1987. Depositional Environments and Diagenesis of Albian Carbonates on the Calabar Flank, S.E. Nigeria. *Journal of Petroleum Geology*. 10 (3), pp 283 – 294.
- Reyment, R.A., (1965). *Aspects of Geology of Nigeria*, Ibadan University Press, Ibadan Nigeria. p.106
- Sharma, R.P., Chopra, V.L. (1976). Effect of the Wingless (wg1) mutation on wing and haltere development in *Drosophila melanogaster*. *Dev. Biol.* 48(): 461--465.
- Spector, A. and Grant, F.S., (1970). Statistical models for interpreting aeromagnetic data. *Geophysics*, Vol.35, pp. 293-302.
- Stoneley, R., (1966). The Niger Delta region in the light of the theory of continental drift. *Geological Magazine* 103, 385-397.
- Tanaka, A., Okubo, Y., and Matsubayashi, O.,1999. Curie point depth based on spectrum analysis of the magnetic anomaly data in East and Southeast Asia, *Tectonophysics* 306, pp. 461-470.
- Thompson, P., 1982. Perceived rate of movement depends on contrast *Vision Research*, 22 (1982), pp. 377–380
- Weber, K.J., and Daukoru, E., (1975). Petroleum geology of the Niger Delta. In: *Proceedings, 9th World Petroleum Congress*. Applied Science Publishers, London 9, 209–221.
- Whitehead, N. and Musselman, C. (2008). *Montaj Gravity/Magnetic Interpretation: Processing, Analysis and Visualization System for 3D Inversion of Potential Field Data for Oasis montaj v6.3*, Geosoft Incorporated, 85 Richmond St. W., Toronto, Ontario, M5H 2C9, Canada.
- Whiteman, A., (1982). *Nigeria : Its Petroleum Geology, Resources and Potential*. Graham and Trotham, London.



Integrated landsat-etm* and aeromagnetic study for enhanced structural and geothermal interpretation: case study of part of Calabar flank, Nigeria.. By Chukwuka, C. I. is licensed under a [Creative Commons Attribution-NonCommercial-NoDerivatives 4.0 International License](https://creativecommons.org/licenses/by-nc-nd/4.0/)